Mon. Not. R. Astron. Soc. **312**, 585–628 (2000)

NGC 6153: a super-metal-rich planetary nebula?

X.-W. Liu,[1] P. J. Storey,[1] M. J. Barlow,[1] I. J. Danziger,[2] M. Cohen[3] and M. Bryce[4]
[1]*Department of Physics and Astronomy, University College London, Gower Street, London WC1E 6BT*
[2]*Osservatorio Astronomico di Trieste, Via G. B. Tiepolo 11, I-34131 Trieste, Italy*
[3]*Radio Astronomy Laboratory, 601 Campbell Hall, University of California, Berkeley, CA 94720, USA*
[4]*Dept. of Physics and Astronomy, University of Manchester, Oxford Road, Manchester M13 9PL*

Accepted 1999 October 7. Received 1999 October 4; in original form 1999 July 12

ABSTRACT

We have obtained deep optical spectra of the planetary nebula NGC 6153, both along its minor axis and by uniformly scanning a long slit across the whole nebula. The scanned spectra, when combined with the nebular total Hβ flux, yield integrated fluxes for all the lines ($\sim$400) in our spectra, which are rich in strong recombination lines from C, N, O and Ne ions. A weak O VI λ3811 emission line from the central star has been detected, suggesting that the nucleus of NGC 6153 has a hydrogen-deficient surface. The optical data, together with the *ISO* LWS 43–197 μm spectrum and the archival *IUE* and *IRAS* LRS spectra, are used to study the thermal and density structure and to derive the heavy-element abundances from lines produced by different excitation mechanisms. In all cases, the C^{2+}/H^+, N^{2+}/H^+, O^{2+}/H^+ and Ne^{2+}/H^+ abundances derived from multiple optical recombination lines (ORLs) are consistently higher, by about a factor of 10, than the corresponding values deduced from optical, UV or infrared (IR) collisionally excited lines (CELs), regardless of the excitation energies or critical densities of the latter. The agreement between the temperature-sensitive optical forbidden lines and the temperature-insensitive IR fine-structure lines rules out temperature fluctuations as the cause of the large difference between the ORL and CEL abundances.

We present the results of a new calculation of recombination coefficients for [O II] which lead to good agreement between the observed and predicted [O II] $\lambda\lambda$7320, 7330 forbidden line intensities if these lines are solely excited by recombination at the Balmer jump temperature. Recombination excitation is also found to be important in exciting the [N II] λ5754 line, which, if unaccounted for, would lead to an overestimated [N II] temperature from the observed (λ6548+λ6584)/λ5754 ratio. Analysis of a number of C II lines arising from levels as high as 7g in the recombination ladder reveals excellent agreement between their reddening-corrected relative intensities and those predicted by recombination theory. Spatial analysis of the long-slit spectra taken along the nebular minor axis yields a varying [O III] temperature, whereas the hydrogen Balmer jump temperature of 6000 K is approximately constant across the nebula, and is 2000–3000 K lower than the [O III] temperature. The observed high-n Balmer line decrement indicates that the hydrogen lines arise from material having an electron density of 2000^{+2000}_{-1000} cm^{-3}, consistent with the optical and IR forbidden-line density diagnostics, which yield average line-of-sight electron densities along the minor axis varying between 2000 and 4000 cm^{-3}.

While the He/H ratio mapped by He I and He II recombination lines is constant within 5 per cent across the nebula, the C^{2+}/H^+ and O^{2+}/H^+ recombination-line abundances decrease by a factor of 2–3 over a radius of 15 arcsec from the centre, pointing to the presence of abundance gradients. We consider a variety of hypotheses to account for the observed behaviour of the various thermal, density and abundance diagnostics. Empirical nebular models containing two components with differing densities and temperatures are able to account for many of the observed patterns, but only if one of the components is significantly hydrogen-deficient. One such model, which gives a good fit to the observed line intensities and patterns, has 500-K H-depleted material, presumed to be evaporating

from dense neutral inclusions, embedded in 9500-K material with 'normal' abundances. An alternative model, which appears more physically plausible on a number of grounds, has high-density (2×10^6 cm^{-3}), fully ionized, H-deficient knots embedded in the 'normal' component, although this model fails to account adequately for the observed low (6000 K) hydrogen Balmer jump temperature. However, the observed fact that the ORLs and CELs yield heavy-element abundance ratios that are identical within the uncertainties finds no obvious explanation in the context of H-deficient knot models.

Key words: ISM: abundances – planetary nebulae: individual: NGC 6153.

1 INTRODUCTION

The emission-line analysis of photoionized nebulae is one of the major tools used to obtain knowledge of abundances in our Galaxy, and is often the sole tool for extragalactic systems. The technique has been used to study planetary nebulae (PNe; envelopes ejected by low- and intermediate-mass stars in their late evolutionary stage), H II regions surrounding young hot stars, and envelopes ejected by Of, LBV and Wolf–Rayet stars. Abundance analyses of these objects have revealed much about the formation and evolution of stars and of the Galaxy. Analyses of giant H II regions in distant galaxies yield elemental abundances for those systems, particularly those of He, N, O and Ne, which are otherwise unobtainable. The primordial He abundance derived for the least chemically evolved extragalactic H II regions and dwarf galaxies constrains big bang nucleosynthesis and the density of baryonic matter. Emission-line analysis techniques are also used to study other nebular-type objects, including novae, supernova remnants and active galactic nuclei.

Until recently, heavy-element abundances of ionized nebulae have been based on bright optical and UV collisionally excited lines (CELs), which dominate nebular spectra (e.g. Osterbrock 1989). Abundances thus derived have an exponential (Boltzmann factor) sensitivity to the adopted electron temperature T_e. For CELs with a low critical density, N_{crit}, the results are also sensitive to the adopted electron density N_e for the emitting regions (Rubin 1989). Alternatively, metal abundances can be derived by measuring optical recombination lines (ORLs) from heavy-element ions. Although they are much weaker and more difficult to measure than CELs, the emissivities of radiative ORLs from hydrogen, helium and heavy-element ions have only a weak, similar, power-law dependence on T_e, and are essentially independent of N_e under typical nebular conditions. Thus ionic abundances derived from the intensities of heavy-element ORLs relative to a hydrogen recombination line, such as Hβ, are almost independent of the temperature and density structure of the nebulae under study, and consequently should be more reliable.

A long-standing problem in nebular abundance studies has been that heavy-element abundances derived from ORLs are often (though not always) higher than those derived from UV and optical CELs. In the early 1980s, *IUE* observations of PNe showed that the C^{2+}/H^+ abundances derived from the collisionally excited C III] $\lambda\lambda$1907, 1909 intercombination lines are generally lower than those derived from the C II λ4267 optical recombination line, by factors of 3–10 in some cases (e.g. Kaler 1986; Barker 1991, and references therein). Various explanations have been advanced, yet no consensus has been reached.

The advent of large-format CCDs, with high quantum efficiency and large dynamic range, has enabled many weak lines, previously impossible or difficult to detect, to be measured with high accuracy. The new measurements, together with the high-quality effective recombination coefficients now available for many heavy-element ions (Péquignot, Petitjean & Boisson 1991; Storey 1994; Liu et al. 1995a, hereafter LSBC) have opened up the possibility of obtaining accurate abundances using ORLs from heavy-element ions. Using line intensities published in the literature, Peimbert, Storey & Torres-Peimbert (1993) derived O^{++}/H^+ abundances from O II recombination lines for the H II regions M 42 and M 17 and the PN NGC 6572 and found them to be a factor of 2 higher than those derived from the [O III] forbidden lines. In a detailed analysis of recombination lines from C, N and O ions in the PN NGC 7009, LSBC detected and measured more than 100 O II lines. The excellent agreement between O^{2+}/H^+ abundances derived from a large number of O II transitions with different electron configurations strongly supports the recombination interpretation of these lines and the reliability and accuracy of current recombination theory for non-hydrogenic ions. The recombination line C, N and O abundances, relative to H, derived for NGC 7009 were all about a factor of 5 higher than those deduced from the CELs. Similar analysis for a number of additional PNe (Liu et al. 1999) yielded O/H abundances which are consistently higher than those from CELs, reaching a factor of $\gtrsim$20 in the extreme case of the Galactic bulge PN M 1-42.

The large discrepancies between the ORL and CEL abundances observed in many PNe point to the possibility that there are fundamental flaws in our current understanding of the nebular thermal and ionization structure. Without a better understanding of the cause of the discrepancy, nebular abundances cannot be taken as intrinsically secure. Since the ratios of abundances derived from these two types of emission line vary from object to object and cover a wide range of 1–20, the cause is likely to be found in the nebular physical conditions, rather than in the basic atomic physics. Peimbert (1967) first discussed the possibility that the traditional method of abundance determinations, based on the standard technique of CEL analysis, might underestimate nebular heavy-element abundances. Given the strong T_e-dependence of the ionic abundances derived from CELs, he showed that in the presence of temperature fluctuations, standard temperature diagnostics, such as the [O III] nebular ($\lambda\lambda$4959, 5007) to auroral (λ4363) line ratio, will overestimate the electron temperature, and, as a consequence, ionic abundances of heavy elements derived from CELs will be underestimated. The first observational evidence suggesting that PNe and H II regions may have significant temperature fluctuations was provided by Peimbert (1971). He measured the electron temperatures using the ratio of the nebular continuum Balmer discontinuity to Hβ, for three PNe and several regions of the Orion nebula and found them to be systematically lower than those derived from the [O III] forbidden-line ratio. He interpreted the results as due to the presence of large temperature fluctuations in the nebulae. On the other hand,

Barker (1978) measured Balmer jump temperatures for 19 PNe, and found them to be in general agreement with those derived from the [O III] forbidden lines. More recently, Liu & Danziger (1993b) measured Balmer jump temperatures for 14 PNe and found that the new measurements, together with those published by Peimbert (1971) and Barker (1978), showed that, on average, the Balmer jump temperatures tend to be lower than the [O III] temperatures. Dinerstein, Lester & Werner (1985) measured [O III] 52- and 88-μm far-IR fine-structure line fluxes for six PNe using the Kuiper Airborne Observatory (KAO), and found that for four of them the electron temperatures calculated from the λ5007/52 μm ratio were significantly lower than those given by the λ5007/λ4363 ratio and concluded that the nebulae were not isothermal. However, reanalysis of the KAO measurements by Dinerstein et al. (1995) showed that for NGC 6543 the electron temperatures derived from these two diagnostics agree within the errors, contrary to the earlier finding of Dinerstein et al. (1985).

Although temperature fluctuations provide a plausible interpretation for the large discrepancies in abundances derived from the two types of emission line and for discrepancies in electron temperatures deduced from the nebular continuum Balmer discontinuity and from the [O III] forbidden line ratio, the large temperature fluctuations required to reconcile the discrepancies are not predicted by nebular photoionization modelling (Gruenwald & Viegas 1995; Kingdon & Ferland 1995b), with the possible exception of some starburst models examined by Pérez (1997), where some relatively large amplitude of temperature fluctuations were found. Other proposed mechanisms potentially capable of producing large temperature fluctuations include extra heating from shock waves (Peimbert, Sarmiento & Fierro 1991), strong density inhomogeneities (Viegas & Clegg 1994) or abundance gradients (Torres-Peimbert, Peimbert & Peña 1990). Direct observational evidence pointing to the operation of such mechanisms in nebulae has yet to be found.

We have been undertaking a systematic ORL abundance survey for a large sample of Galactic PNe and H II regions, using the ESO 1.52-m, the AAT 3.9-m and the WHT 4.2-m telescopes. So far, about 80 PNe have been observed. For about half of them, we have also obtained 43–197 μm far-IR grating spectra using the Long Wavelength Spectrometer (LWS) on board the *Infrared Space Observatory* (*ISO*). *ISO* 2.4–45 μm Short Wavelength Spectrometer (SWS) spectra are also available for the majority of them. The deep optical observations will deliver for a large sample of PNe accurate recombination line C, N and O abundances, which will be compared to those derived from IR, optical and UV (from the *IUE* archival data) CELs of different excitation energies and critical densities. The abundance discrepancies between the two types of emission lines will be studied in terms of the excitation energies and the critical densities of CELs, the nebular properties (morphology, electron temperature and density, and chemical composition) and the properties of the exciting central stars (luminosities, effective temperature, evolutionary stage and surface composition), in order to probe the underlying physical causes. The mid- and far-IR fine-structure lines observable with *ISO* are particularly useful in testing temperature/density fluctuations as the cause of the discrepancies. With excitation energies $E_{\rm ex} \lesssim 1000$ K, abundances derived from IR fine-structure lines are insensitive to temperature and temperature fluctuations. In addition, the IR lines cover a wide range of critical densities and can be used to quantify density inhomogeneities and their effects on abundance determinations, without complications from thermal or ionization stratification.

As the first of a series of papers on abundance determinations in gaseous nebulae, we present here a detailed case study for the PN NGC 6153, utilizing UV to far-IR observations. The unusual nature of NGC 6153 was first noted by Pottasch et al. (1984), from its strong *IRAS* LRS infrared emission-line spectrum. Analysis of the spectrum showed that NGC 6153 probably has the highest nebular neon abundance known. A subsequent analysis of its UV, optical and LRS spectra by Pottasch, Dennefield & Mo (1986, hereafter PDM) showed that NGC 6153 has higher abundances of almost all measurable elements than any other PN. A more recent analysis by Kingsburgh & Barlow (1994) however yielded a significantly higher [O III] temperature than derived by PDM and consequently a more or less 'normal' chemical composition, except for Ne and possibly also N, which were still enhanced by a factor of 2 relative to the average values for PNe. The peculiar composition of NGC 6153 was reconfirmed during our deep ORL abundance survey. Its optical spectrum is found to be strikingly similar to that of NGC 7009 (LSBC), with extremely rich recombination lines from O II, N II, C II and Ne II, indicating extremely high metal abundances. Of the approximately 80 PNe so far surveyed, only two other objects, M 2-36 and M 1-42, both bulge PNe, show such a prominent recombination-line spectrum. The detection in NGC 6153 of a large number of ORLs from a variety of heavy-element ions provides another opportunity, after NGC 7009, to test the recombination theories of heavy-element ions. The availability at the same time of heavy-element abundances from a large number of CELs, spanning wavelengths from UV to far-IR and covering a wide range in $E_{\rm ex}$ and $N_{\rm crit}$, allows us to test the prevailing interpretation of temperature/density fluctuations as the cause of the large abundance discrepancies between the two types of emission lines. In Section 2 we describe our new spectroscopic observations of NGC 6153, using the ESO 1.52-m telescope in the optical and the space-borne *ISO* LWS in the far-IR, and present line fluxes obtained from the new observations as well as from newly recalibrated *IUE* and *IRAS* LRS spectra retrieved from the archives. In Section 3 we present nebular abundance analyses using UV, optical and IR collisionally excited lines and optical recombination lines. In Section 4 long-slit spectra obtained along the nebular minor axis are used to map the extinction, the electron temperature and density, and the ionic abundances, across the nebular surface. The implications and possible interpretations of the results from this extensive multi-waveband analysis are discussed in Sections 5 and 6. A summary of some results from this study was presented by Liu (1998).

2 OBSERVATIONS

2.1 Optical spectroscopy

2.1.1 Observations

The observations were taken during three runs at the ESO 1.52-m

Table 1. Journal of ESO 1.52-m telescope observations.

Date (UT)	λ-range (Å)	FWHM (Å)	PA (deg)	Exp. Time (sec)
30/07/95	3523–7421	4.5	122.8	120, 2 × 600
25/07/95	4000–4984	1.5	122.8	3 × 1800
11/07/96	3040–4050	1.5	122.8	3 × 1800
10/07/96	4005–4990	1.5	122.8	1800
08/02/97	3530–7428	4.5	Scanning	40, 660
09/02/97	4005–4990	1.5	Scanning	2 × 1800
11/02/97	4005–4990	1.5	Scanning	1140

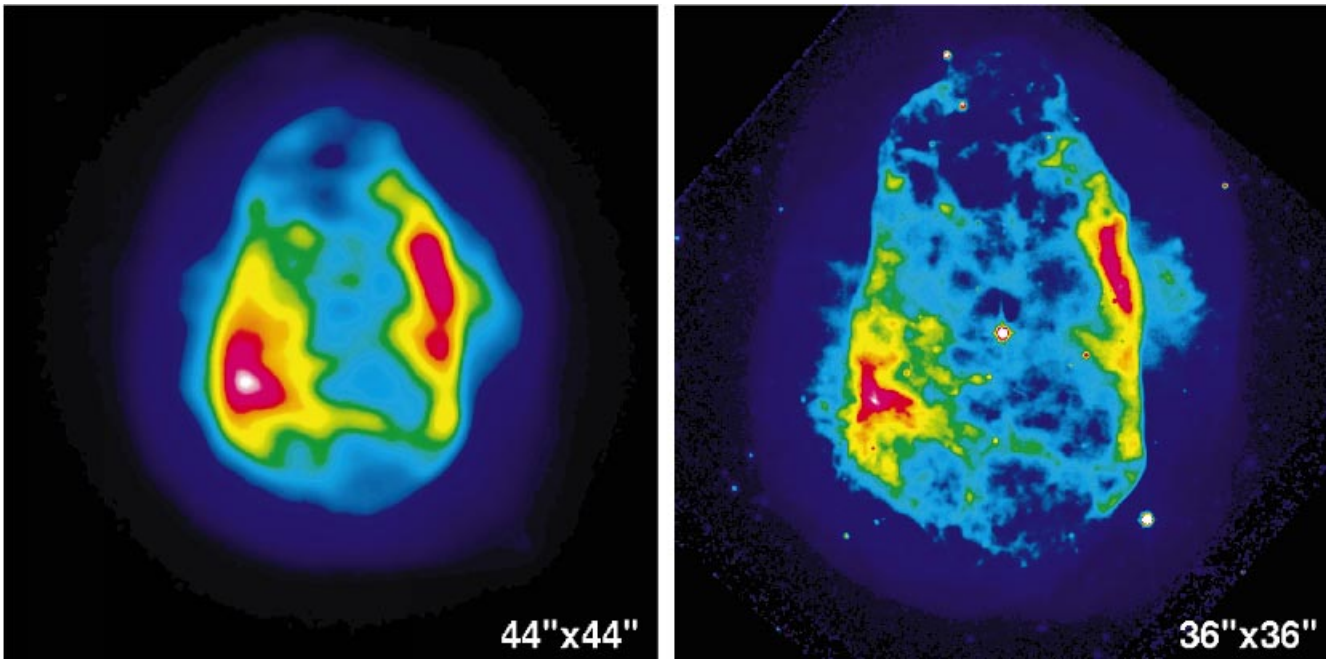

Figure 1. The planetary nebula NGC 6153. The image on the left was obtained with the Manchester Echelle Spectrometer at the AAT 3.9-m telescope in the light of [O III] λ5007. The seeing was approximately 1 arcsec. The image on the right is an *HST* WFPC2 snapshot taken through a broad-band filter F814W. The observed emission in the latter image is probably dominated by H I Paschen lines and the nebular continuum emission. North is up, and east to the left. The 'minor-axis' spectra discussed in the paper were taken with a 2-arcsec-wide slit centred on the central star and oriented in PA = 122.°8. Mean spectra of the whole nebula were obtained by uniformly scanning the long-slit, oriented north–south, across the whole nebular surface by differentially driving the telescope in Right Ascension.

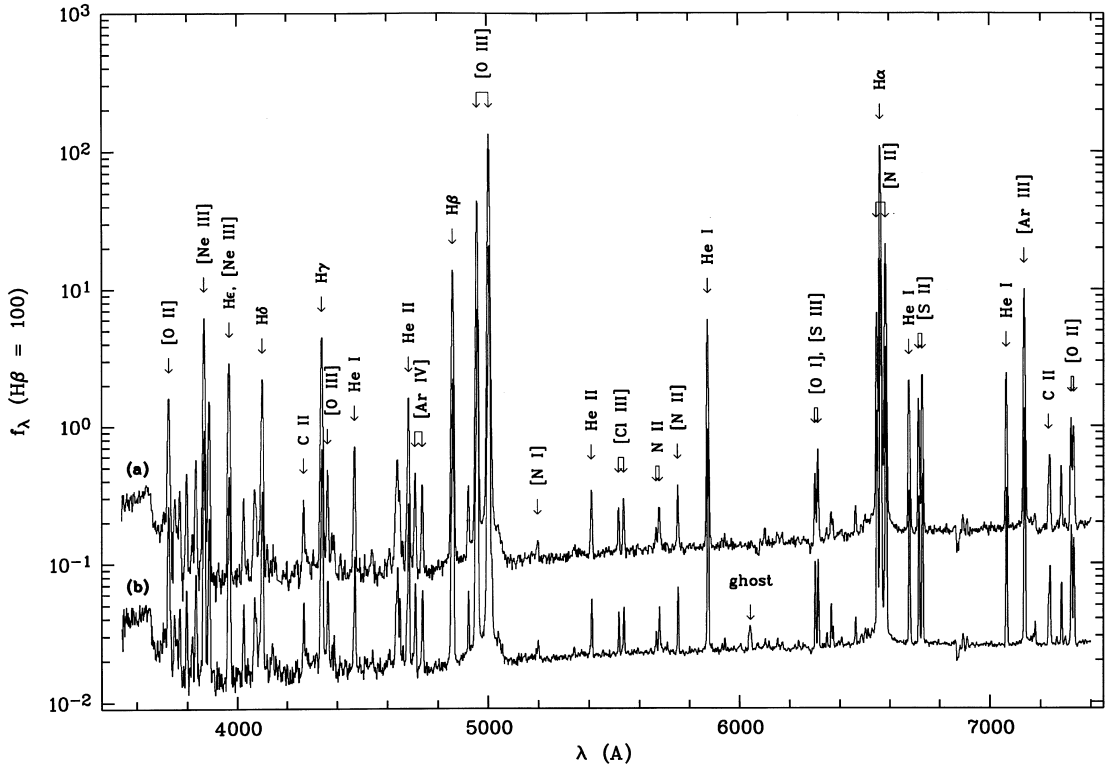

Figure 2. Optical spectra of NGC 6153 from 3540 to 7400 Å. The two spectra plotted are (a) obtained by uniformly scanning the long-slit across the entire nebula, and (b) taken with a fixed slit centred on the central star at PA = 122.°8, roughly defined as the nebular minor axis (Fig. 1). Note that the [O III] λλ4959, 5007 lines and Hα were saturated on these deep exposures (∼10 min), and that C II and N II recombination lines are prominent even in these low-resolution spectra.

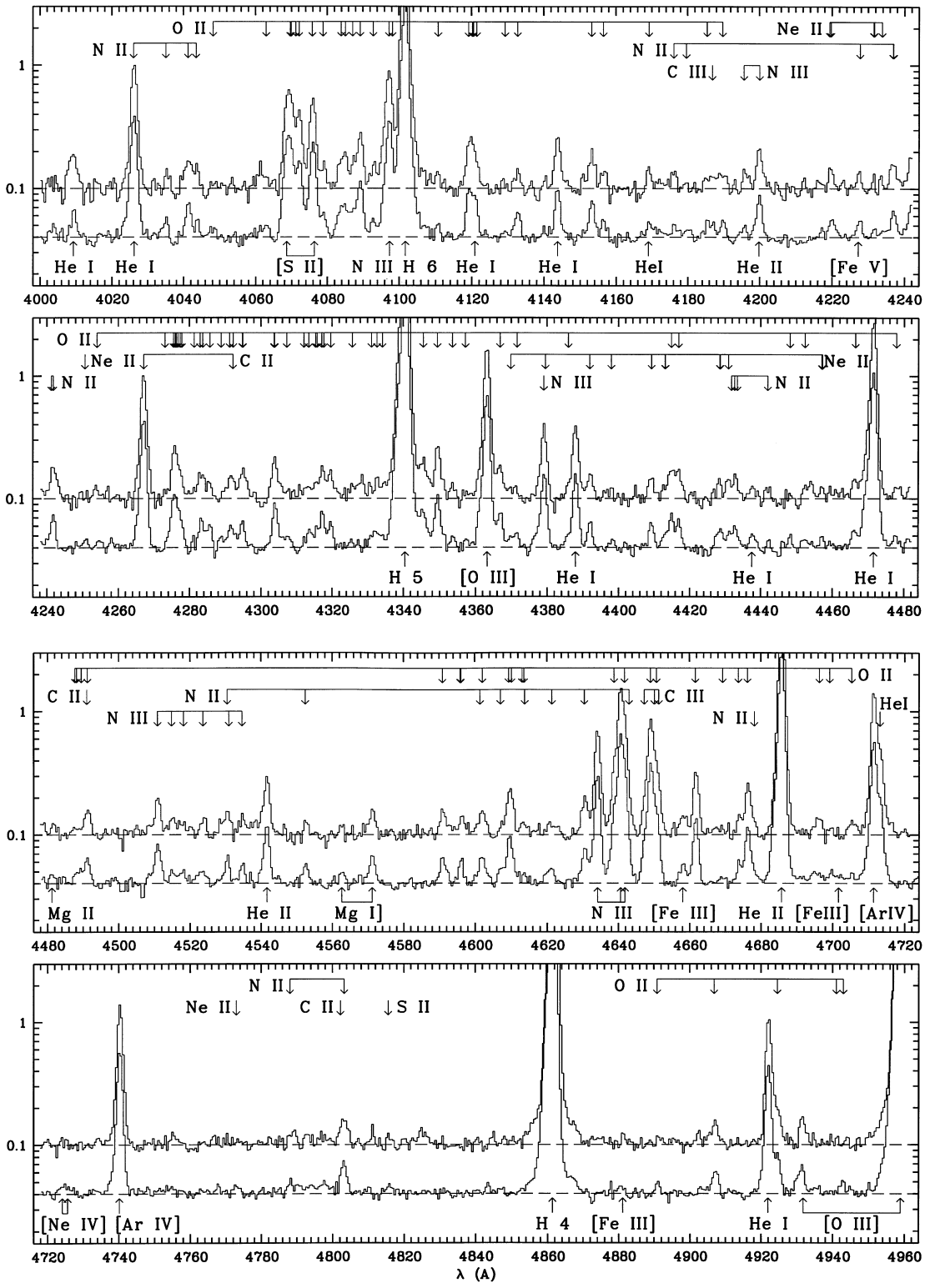

Figure 3. Continuum-subtracted spectra of NGC 6153 from 4000 to 4960 Å, showing the rich recombination-line spectra from C, N, O and Ne ions. The upper spectrum was obtained by uniformly scanning the entire nebular surface using a narrow long-slit, and the lower one was obtained with a fixed slit centred on the central star at PA = 122°.8. Both spectra were normalized such that $F(\mathrm{H}\beta) = 100$.

telescope using the B&C spectrograph. A journal of the observations is given in Table 1. In 1995 July the detector was a Ford 2048 × 2048 15 μm × 15 μm CCD, which was superseded in 1996 and 1997 by a thinned UV-enhanced Loral 2048 × 2048 15 μm × 15 μm chip of much improved quantum efficiency (about a factor of 5 at 4000 Å). The B&C spectrograph has a useful slit length of about 3.5 arcmin. During all three runs, in order to reduce the CCD read-out noise, the CCDs were binned by a factor of 2 along the slit direction, yielding a spatial sampling of 1.63 arcsec per pixel projected on the sky. A slit width of 2 arcsec

Table 2. Observed relative line fluxes, on a scale where H$\beta = 100$.

Minor axis			Entire nebula			Ion	λ_0	Mult	Lower Term	Upper Term	g_1	g_2
λ_{obs}	$F(\lambda)$	$I(\lambda)$	λ_{obs}	$F(\lambda)$	$I(\lambda)$							
3045.88	1.384	5.957	*	*	*	O III	3047.12	V4	3s 3P*	3p 3P	5	5
3121.32	0.203	0.783	*	*	*	O III	3121.71	V12	3p 3S	3d 3P*	3	3
3132.30	6.671	25.40	*	*	*	O III	3132.79	V12	3p 3S	3d 3P*	3	5
3184.70	0.019	0.066	*	*	*	Si III	3185.12	V8	4p 1P*	5s 1S	3	1
3187.43	0.948	3.360	*	*	*	He I	3187.74	V3	2s 3S	4p 3P*	3	9
3202.83	1.539	5.354	*	*	*	He II	3203.10	3.5	3d+ 2D	5f+ 2F*	18	50
3217.86	0.145	0.496	*	*	*	Ne II	3218.19	V13	3p 4D*	3d 4F	8	10
3220.87	0.057	0.193	*	*	*	?	*				*	*
3241.73	0.129	0.429	*	*	*	Si III	3241.62	V6	4p 3P*	5s 3S	5	3
3299.21	0.354	1.101	*	*	*	O III	3299.36	V3	3s 3P*	3p 3S	1	3
3312.24	0.907	2.778	*	*	*	O III	3312.30	V3	3s 3P*	3p 3S	3	3
3334.90	0.245	0.731	*	*	*	Ne II	3334.84	V2	3s 4P	3p 4D*	6	8
3340.75	1.402	4.163	*	*	*	O III	3340.74	V3	3s 3P*	3p 3S	5	3
3354.98	0.157	0.460	*	*	*	Ne II	3355.02	V2	3s 4P	3p 4D*	4	6
3388.36	0.045	0.127	*	*	*	Ne II	3388.42	V20	3p 2D*	3d 2F	4	6
3405.62	0.053	0.146	*	*	*	O III	3405.74	V15	3p 3P	3d 3P*	1	3
3417.41	0.101	0.277	*	*	*	Ne II	3417.69	V19	3p 2D*	3d 4F	6	8
3428.63	0.494	1.340	*	*	*	O III	3428.65	V15	3p 3P	3d 3P*	3	5
3444.01	2.892	7.734	*	*	*	O III	3444.07	V15	3p 3P	3d 3P*	5	5
3447.84	0.048	0.128	*	*	*	He I	3447.59	V7	2s 1S	6p 1P*	1	3
3466.33	0.029	0.076	*	*	*	He I	3465.94		2p 3P*	17d 3D	9	15
3471.16	0.033	0.086	*	*	*	He I	3471.83	V44	2p 3P*	16d 3D	9	15
3478.30	0.046	0.119	*	*	*	He I	3478.97	V43	2p 3P*	15d 3D	9	15
3487.47	0.032	0.082	*	*	*	He I	3487.73	V42	2p 3P*	14d 3D	9	15
3498.35	0.061	0.155	*	*	*	He I	3498.66	V40	2p 3P*	13d 3D	9	15
3512.43	0.072	0.180	*	*	*	He I	3512.52	V38	2p 3P*	12d 3D	9	15
3530.27	0.088	0.217	*	*	*	He I	3530.50	V36	2p 3P*	11d 3D	9	15
3554.37	0.118	0.286	*	*	*	He I	3554.42	V34	2p 3P*	10d 3D	9	15
3568.28	0.104	0.248	*	*	*	Ne II	3568.50	V9	3s′ 2D	3p′ 2F*	6	8
3587.21	0.163	0.382	*	*	*	He I	3587.28	V31	2p 3P*	9d 3D	9	15
3613.63	0.151	0.347	*	*	*	He I	3613.64	V6	2s 1S	5p 1P*	1	3
3634.10	0.245	0.554	*	*	*	He I	3634.25	V28	2p 3P*	8d 3D	9	15
3671.24	0.212	0.470	*	*	*	H 24	3671.48	H24	2p+ 2P*	24d+ 2D	8	*
3673.69	0.219	0.485	*	*	*	H 23	3673.74	H23	2p+ 2P*	23d+ 2D	8	*
3676.34	0.255	0.564	*	*	*	H 22	3676.36	H22	2p+ 2P*	22d+ 2D	8	*
3679.35	0.281	0.620	*	*	*	H 21	3679.36	H21	2p+ 2P*	21d+ 2D	8	*
3682.75	0.311	0.685	*	*	*	H 20	3682.81	H20	2p+ 2P*	20d+ 2D	8	*
3686.82	0.344	0.756	*	*	*	H 19	3686.83	H19	2p+ 2P*	19d+ 2D	8	*
3691.51	0.425	0.932	*	*	*	H 18	3691.56	H18	2p+ 2P*	18d+ 2D	8	*
3694.25	0.205	0.448	*	*	*	Ne II	3694.21	V1	3s 4P	3p 4P*	6	6
3697.11	0.466	1.021	*	*	*	H 17	3697.15	H17	2p+ 2P*	17d+ 2D	8	*
3704.00	0.818	1.784	*	*	*	H 16	3703.86	H16	2p+ 2P*	16d+ 2D	8	*
3705.16	0.198	0.432	*	*	*	He I	3705.02	V25	2p 3P*	7d 3D	9	15
3707.40	0.085	0.185	*	*	*	O III	3707.25	V14	3p 3P	3d 3D*	3	5
3709.77	0.070	0.152	*	*	*	Ne II	3709.62	V1	3s 4P	3p 4P*	4	2
3712.12	0.907	1.970	*	*	*	H 15	3711.97	H15	2p+ 2P*	15d+ 2D	8	*
3715.23	0.092	0.200	*	*	*	O III	3715.08	V14	3p 3P	3d 3D*	5	7
3722.42	1.496	3.233	*	*	*	H 14	3721.94	H14	2p+ 2P*	14d+ 2D	8	*
	*	*	*	*	*	[S III]	3721.63	F2	3p2 3P	3p2 1S	3	1
3726.07	8.817	19.01	*	15.23[a]	32.81[a]	[O II]	3726.03	F1	2p3 4S*	2p3 2D*	4	4
3728.78	4.730	10.18	*	*	*	[O II]	3728.82	F1	2p3 4S*	2p3 2D*	4	6
3734.33	1.051	2.257	*	*	*	H 13	3734.37	H13	2p+ 2P*	13d+ 2D	8	*
3750.09	1.524	3.246	*	*	*	H 12	3750.15	H12	2p+ 2P*	12d+ 2D	8	*
3754.63	0.205	0.435	*	*	*	O III	3754.69	V2	3s 3P*	3p 3D	3	5
3757.17	0.115	0.244	*	*	*	O III	3757.24	V2	3s 3P*	3p 3D	1	3
3759.80	0.675	1.431	*	*	*	O III	3759.87	V2	3s 3P*	3p 3D	5	7
3770.62	1.781	3.751	*	*	*	H 11	3770.63	H11	2p+ 2P*	11d+ 2D	8	*
3774.00	0.048	0.102	*	*	*	O III	3774.02	V2	3s 3P*	3p 3D	3	3
3777.12	0.021	0.044	*	*	*	Ne II	3777.14	V1	3s 4P	3p 4P*	2	4
3791.51	0.053	0.110	*	*	*	O III	3791.27	V2	3s 3P*	3p 3D	5	5
3797.92	2.442	5.068	*	2.722[b]	5.651[b]	H 10	3797.90	H10	2p+ 2P*	10d+ 2D	8	*
3806.27	0.043	0.088	*	*	*	He I	3805.74	V58	2p 1P*	11d 1D	3	5
3813.71	0.056	0.116	*	*	*	He II	3813.50	4.19	4f+ 2F*	19g+ 2G	32	*
3819.69	0.744	1.525	*	*	*	He I	3819.62	V22	2p 3P*	6d 3D	9	15
3835.42	3.818	7.761	*	3.974	8.078	H 9	3835.39	H9	2p+ 2P*	9d+ 2D	8	*
3856.02	0.091	0.183	*	*	*	O II	3856.13	V12	3p 4D*	3d 4D	4	2
	*	*	*	*	*	Si II	3856.02	V1	3p2 2D	4p 2P*	6	4
3858.51	0.054	0.108	*	*	*	He II	3858.07	4.17	4f+ 2F*	17g+ 2G	32	*
3862.65	0.142	0.284	*	*	*	Si II	3862.60	V1	3p2 2D	4p 2P*	4	2
3868.81	48.38	96.42	*	46.81	93.35	[Ne III]	3868.75	F1	2p4 3P	2p4 1D	5	5

Table 2 – *continued*

Minor axis			Entire nebula			Ion	λ_0	Mult	Lower Term	Upper Term	g_1	g_2
λ_{obs}	$F(\lambda)$	$I(\lambda)$	λ_{obs}	$F(\lambda)$	$I(\lambda)$							
3882.46	0.101	0.199	*	*	*	O II	3882.19	V12	3p 4D*	3d 4D	8	8
	*	*	*	*	*	O II	3882.45	V11	3p 4D*	3d 4P	4	4
	*	*	*	*	*	O II	3883.13	V12	3p 4D*	3d 4D	8	6
3888.92	10.69	21.05	*	11.32	22.31	H 8	3889.05	H8	2p+ 2P*	8d+ 2D	8	*
	*	*	*	*	*	He I	3888.65	V2	2s 3S	3p 3P*	3	9
3907.51	0.019	0.036	*	*	*	O II	3907.46	V11	3p 4D*	3d 4P	6	6
3919.14	0.025	0.048	*	*	*	C II	3918.98	V4	3p 2P*	4s 2S	2	2
3920.86	0.031	0.060	*	*	*	C II	3920.69	V4	3p 2P*	4s 2S	4	2
3923.75	0.050	0.096	*	*	*	He II	3923.48	4.15	4f+ 2F*	15g+ 2G	32	*
3926.71	0.073	0.140	*	*	*	He I	3926.54	V58	2p 1P*	8d 1D	3	5
3967.51	15.44	29.00	*	23.88[c]	44.80[c]	[Ne III]	3967.46	F1	2p4 3P	2p4 1D	3	5
3970.12	8.654	16.22	*	*	*	H 7	3970.07	H7	2p+ 2P*	7d+ 2D	8	98
3995.13	0.047	0.087	*	*	*	N II	3994.99	V12	3s 1P*	3p 1D	3	5
3998.80	0.034	0.063	*	*	*	N III	3998.63	V17	4d 2D	5f 2F*	4	6
4003.66	0.041	0.075	*	*	*	N III	4003.58	V17	4d 2D	5f 2F*	6	8
4009.40	0.138	0.252	4009.07	0.198	0.362	He I	4009.26	V55	2p 1P*	7d 1D	3	5
4026.18	1.694	3.066	4026.21	1.740	3.149	He I	4026.21	V18	2p 3P*	5d 3D	9	15
	*	*	*	*	*	N II	4026.08	V39b	3d 3F*	4f 2[5]	7	9
4035.13	0.070	0.126	4035.13	0.059	0.106	N II	4035.08	V39a	3d 3F*	4f 2[4]	5	7
4041.36	0.160	0.286	4041.36	0.140	0.251	N II	4041.31	V39b	3d 3F*	4f 2[5]	9	11
4043.55	0.056	0.100	4043.58	0.086	0.154	N II	4043.53	V39a	3d 3F*	4f 2[4]	7	9
4048.23	0.035	0.063	*	*	*	O II	4048.21	V50b	3d 4F	4f F3*	8	8
4062.96	0.052	0.092	4062.92	0.059	0.104	O II	4062.94	V50a	3d 4F	4f F4*	10	10
4068.62	0.724	1.274	4068.58	0.581	1.022	[S II]	4068.60	F1	2p3 4S*	2p3 2P*	4	4
4069.64	0.537	0.944	4069.61	0.352	0.620	O II	4069.62	V10	3p 4D*	3d 4F	2	4
4069.91	0.235	0.414	4069.87	0.414	0.729	O II	4069.89	V10	3p 4D*	3d 4F	4	6
4071.25	0.047	0.082	4071.22	0.045	0.080	O II	4071.23	V48a	3d 4F	4f G5*	8	10
4072.18	0.596	1.047	4072.14	0.582	1.022	O II	4072.16	V10	3p 4D*	3d 4F	6	8
4075.87	0.730	1.279	4075.85	0.649	1.138	O II	4075.86	V10	3p 4D*	3d 4F	8	10
4076.36	0.244	0.427	4076.33	0.196	0.343	[S II]	4076.35	F1	2p3 4S*	2p3 2P*	2	4
4078.86	0.100	0.175	4078.83	0.099	0.174	O II	4078.84	V10	3p 4D*	3d 4F	4	4
4083.84	0.123	0.215	4083.92	0.112	0.195	O II	4083.90	V48b	3d 4F	4f G4*	6	8
4085.06	0.109	0.190	4085.14	0.122	0.213	O II	4085.11	V10	3p 4D*	3d 4F	6	6
4087.10	0.122	0.212	4087.18	0.112	0.195	O II	4087.15	V48c	3d 4F	4f G3*	4	6
4089.23	0.338	0.588	4089.31	0.312	0.541	O II	4089.29	V48a	3d 4F	4f G5*	10	12
4092.87	0.076	0.131	4092.95	0.106	0.184	O II	4092.93	V10	3p 4D*	3d 4F	8	8
4097.37	1.554	2.685	4097.27	1.668	2.882	N III	4097.33	V1	3s 2S	3p 2P*	2	4
	*	*	*	*	*	O II	4097.25	V20	3p 4P*	3d 4D	2	4
	*	*	*	*	*	O II	4097.26	V48b	3d 4F	4f G4*	8	10
	*	*	*	*	*	O II	4098.24	V46a	3d 4F	4f D3*	4	6
4101.73	15.14	26.07	4101.71	16.10	27.72	H 6	4101.74	H6	2p+ 2P*	6d+ 2D	8	72
4110.71	0.042	0.073	4110.76	0.058	0.099	O II	4110.78	V20	3p 4P*	3d 4D	4	2
4119.14	0.221	0.377	4119.17	0.274	0.467	O II	4119.22	V20	3p 4P*	3d 4D	6	8
4120.20	0.020	0.034	4120.24	0.025	0.042	O II	4120.28	V20	3p 4P*	3d 4D	6	6
4120.47	0.048	0.081	4120.50	0.059	0.100	O II	4120.54	V20	3p 4P*	3d 4D	6	4
4120.76	0.080	0.137	4120.79	0.032	0.054	He I	4120.84	V16	2p 3P*	5s 3S	9	3
4121.39	0.070	0.119	4121.42	0.087	0.147	O II	4121.46	V19	3p 4P*	3d 4P	2	2
4129.25	0.018	0.030	4129.28	0.016	0.027	O II	4129.32	V19	3p 4P*	3d 4P	4	2
4132.73	0.102	0.173	4132.76	0.066	0.111	O II	4132.80	V19	3p 4P*	3d 4P	2	4
4143.75	0.249	0.416	4143.80	0.294	0.493	He I	4143.76	V53	2p 1P*	6d 1D	3	5
4153.32	0.169	0.282	4153.27	0.173	0.289	O II	4153.30	V19	3p 4P*	3d 4P	4	6
4156.55	0.062	0.104	4156.50	0.072	0.120	O II	4156.53	V19	3p 4P*	3d 4P	6	4
4169.25	0.057	0.093	4169.19	0.080	0.132	O II	4169.22	V19	3p 4P*	3d 4P	6	6
	*	*	*	*	*	He I	4168.97	V52	2p 1P*	6s 1S	3	1
4176.19	0.046	0.075	4176.13	0.070	0.115	N II	4176.16	V43a	3d 1D*	4f 1[3]	5	7
4179.70	0.030	0.049	4179.65	0.015	0.024	N II	4179.67	V50a	3d 3D*	4f 2[3]	7	7
4185.47	0.052	0.084	4185.46	0.033	0.053	O II	4185.45	V36	3p′ 2F*	3d′ 2G	6	8
4186.92	0.042	0.068	4186.91	0.048	0.078	C III	4186.90	V18	4f 1F*	5g 1G	7	9
4189.81	0.062	0.101	4189.80	0.070	0.113	O II	4189.79	V36	3p′ 2F*	3d′ 2G	8	10
4195.79	0.038	0.061	4195.77	0.067	0.109	N III	4195.76	V6	3s′ 2P*	3p′ 2D	2	4
4199.86	0.127	0.204	4199.93	0.092	0.148	He II	4199.83	4.11	4f+ 2F*	11g+ 2G	32	*
4200.13	0.068	0.109	4200.11	0.121	0.196	N III	4200.10	V6	3s′ 2P*	3p′ 2D	4	6
4219.75	0.073	0.117	4219.70	0.079	0.126	Ne II	4219.74	V52a	3d 4D	4f 2[4]*	8	10
	*	*	*	*	*	Ne II	4219.37	V52a	3d 4D	4f 2[4]*	8	8
4227.75	0.064	0.101	4227.69	0.053	0.084	N II	4227.74	V33	3p 1D	4s 1P*	5	3
	*	*	*	*	*	[Fe V]	4227.20	F2	3d4 5D	3d4 3H	9	9
4231.64	0.027	0.042	4231.59	0.024	0.038	Ne II	4231.64	V52b	3d 4D	4f 2[3]*	6	8
	*	*	*	*	*	Ne II	4231.53	V52b	3d 4D	4f 2[3]*	6	6
4233.85	0.024	0.038	4233.80	0.028	0.045	Ne II	4233.85	V52a	3d 4D	4f 2[4]*	6	8
4236.92	0.045	0.071	4236.86	0.048	0.075	N II	4236.91	V48a	3d 3D*	4f 1[3]	3	5
4237.06	0.067	0.105	4237.00	0.071	0.111	N II	4237.05	V48b	3d 3D*	4f 1[4]	5	7

Table 2 – *continued*

Minor axis			Entire nebula			Ion	λ_0	Mult	Lower Term	Upper Term	g_1	g_2
λ_{obs}	$F(\lambda)$	$I(\lambda)$	λ_{obs}	$F(\lambda)$	$I(\lambda)$							
4241.25	0.011	0.018	4241.19	0.012	0.018	N II	4241.24	V48a	3d 3D*	4f 1[3]	5	5
4241.79	0.131	0.205	4241.73	0.136	0.213	N II	4241.78	V48b	3d 3D*	4f 1[4]	7	9
4254.71	0.026	0.040	4253.71	0.039	0.060	O II	4254.00	V101	3d′ 2G	4f′ H5*	18	22
4267.18	1.631	2.510	4267.16	1.561	2.402	C II	4267.15	V6	3d 2D	4f 2F*	10	14
4273.06	0.020	0.031	4273.09	0.017	0.026	O II	4273.10	V67a	3d 4D	4f F4*	6	8
4275.51	0.210	0.321	4275.44	0.180	0.275	O II	4275.55	V67a	3d 4D	4f F4*	8	10
4275.95	0.040	0.062	4275.98	0.035	0.053	O II	4275.99	V67b	3d 4D	4f F3*	4	6
4276.24	0.029	0.045	4276.27	0.025	0.038	O II	4276.28	V67b	3d 4D	4f F3*	6	6
4276.71	0.077	0.118	4276.73	0.066	0.101	O II	4276.75	V67b	3d 4D	4f F3*	6	8
4277.39	0.038	0.058	4277.41	0.044	0.068	O II	4277.43	V67c	3d 4D	4f F2*	2	4
4277.85	0.038	0.058	4277.88	0.033	0.050	O II	4277.89	V67b	3d 4D	4f F3*	8	8
4281.27	0.016	0.025	4281.41	0.029	0.045	O II	4281.32	V53b	3d 4P	4f D2*	6	6
4282.91	0.048	0.072	4283.05	0.068	0.104	O II	4282.96	V67c	3d 4D	4f F2*	4	6
4283.68	0.075	0.114	4283.81	0.051	0.077	O II	4283.73	V67c	3d 4D	4f F2*	4	4
4285.64	0.082	0.125	4285.77	0.054	0.082	O II	4285.69	V78b	3d 2F	4f F3*	6	8
4288.77	0.035	0.053	4288.91	0.032	0.049	O II	4288.82	V53c	3d 4P	4f D1*	2	4
	*	*	*	*	*	O II	4288.82	V53c	3d 4P	4f D1*	2	2
4291.20	0.055	0.083	4291.34	0.051	0.077	O II	4291.25	V55	3d 4P	4f G3*	6	8
	≲0.02	≲0.03	*	≲0.03	≲0.05	C II	4292.16		4f 2F*	10g 2G	14	18
4292.16	0.031	0.047	4292.30	0.029	0.043	O II	4292.21	V78c	3d 2F	4f F2*	6	6
4294.76	0.100	0.151	4294.89	0.093	0.140	O II	4294.78	V53b	3d 4P	4f D2*	4	6
	*	*	*	*	*	O II	4294.92	V53b	3d 4P	4f D2*	4	4
4303.93	0.206	0.308	4303.82	0.193	0.289	O II	4303.82	V53a	3d 4P	4f D3*	6	8
	*	*	*	*	*	O II	4303.61	V65a	3d 4D	4f G5*	8	10
4307.37	0.045	0.068	4307.25	0.031	0.046	O II	4307.23	V53b	3d 4P	4f D2*	2	4
4312.24	0.012	0.017	4312.13	0.027	0.041	O II	4312.11	V78a	3d 2F	4f F4*	8	8
4313.58	0.060	0.089	4313.46	0.036	0.054	O II	4313.44	V78a	3d 2F	4f F4*	8	10
4315.53	0.058	0.087	4315.42	0.053	0.078	O II	4315.40	V63c	3d 4D	4f D1*	4	4
	*	*	*	*	*	O II	4315.39	V63c	3d 4D	4f D1*	4	2
	*	*	*	*	*	O II	4315.83	V78b	3d 2F	4f F3*	8	8
4317.27	0.135	0.201	4317.16	0.088	0.130	O II	4317.14	V2	3s 4P	3p 4P*	2	4
4317.84	0.015	0.022	4317.72	0.047	0.070	O II	4317.70	V53a	3d 4P	4f D3*	4	6
4319.76	0.092	0.136	4319.65	0.107	0.159	O II	4319.63	V2	3s 4P	3p 4P*	4	6
4325.90	0.019	0.028	4325.78	0.053	0.079	O II	4325.76	V2	3s 4P	3p 4P*	2	2
4331.27	0.047	0.069	4331.15	0.031	0.046	O II	4331.13	V65b	3d 4D	4f G4*	6	8
4332.84	0.047	0.069	4332.73	0.070	0.103	O II	4332.71	V65b	3d 4D	4f G4*	8	10
4334.33	0.036	0.053	4334.21	0.001	0.002	O II	4334.19	V63b	3d 4D	4f D2*	6	6
4340.46	31.84	46.55	4340.42	33.29	48.67	H 5	4340.47	H5	2p+ 2P*	5d+ 2D	8	50
4345.56	0.176	0.256	4345.67	0.187	0.272	O II	4345.56	V2	3s 4P	3p 4P*	4	2
	*	*	*	*	*	O II	4345.55	V65c	3d 4D	4f G3*	8	8
4349.43	0.266	0.387	4349.54	0.285	0.413	O II	4349.43	V2	3s 4P	3p 4P*	6	6
4353.60	0.037	0.053	4353.71	0.049	0.071	O II	4353.59	V76c	3d 2F	4f G3*	6	8
4357.26	0.024	0.035	4357.37	0.021	0.031	O II	4357.25	V63a	3d 4D*	4f D3*	6	8
	*	*	*	*	*	O II	4357.25	V63a	3d 4D*	4f D3*	6	6
4363.21	2.852	4.102	4363.19	2.895	4.164	[O III]	4363.21	F2	2p2 1D	2p2 1S	5	1
4366.97	0.158	0.227	4366.93	0.151	0.217	O II	4366.89	V2	3s 4P	3p 4P*	6	4
4369.88	0.039	0.056	4369.53	0.039	0.056	Ne II	4369.86	V56	3d 4F	4f 0[3]*	4	6
4371.70	0.046	0.066	4371.66	0.029	0.042	O II	4371.62	V76b	3d 2F	4f G4*	8	10
4377.18	0.057	0.082	4377.26	0.032	0.045	?	*				*	*
4379.19	0.486	0.691	4379.15	0.463	0.659	N III	4379.11	V18	4f 2F*	5g 2G	14	18
	*	*	*	*	*	Ne II	4379.55	V60b	3d 2F	4f 1[4]*	8	10
4385.79	0.043	0.060	4385.71	0.038	0.054	O II	4386.01		3d′ 2D	4f′ G4*	6	8
4388.00	0.462	0.653	4387.97	0.516	0.730	He I	4387.93	V51	2p 1P*	5d 1D	3	5
4392.06	0.098	0.138	4392.04	0.108	0.152	Ne II	4391.99	V55e	3d 4F	4f 2[5]*	10	12
	*	*	*	*	*	Ne II	4392.00	V55e	3d 4F	4f 2[5]*	10	10
4398.06	0.024	0.033	4398.03	0.032	0.045	Ne II	4397.99	V57b	3d 4F	4f 1[4]*	6	8
4409.36	0.095	0.133	4409.34	0.089	0.124	Ne II	4409.30	V55e	3d 4F	4f 2[5]*	8	10
4413.17	0.048	0.067	4413.26	0.041	0.058	Ne II	4413.22	V65	3d 4P	4f 0[3]*	6	8
	*	*	*	*	*	Ne II	4413.11	V57c	3d 4F	4f 1[3]*	4	6
	*	*	*	*	*	Ne II	4413.11	V65	3d 4P	4f 0[3]*	6	6
4414.96	0.133	0.184	4414.94	0.133	0.184	O II	4414.90	V5	3s 2P	3p 2D*	4	6
4417.03	0.101	0.140	4417.01	0.124	0.171	O II	4416.97	V5	3s 2P	3p 2D*	2	4
4428.62	0.075	0.102	4428.59	0.061	0.083	Ne II	4428.64	V60c	3d 2F	4f 1[3]*	6	8
	*	*	*	*	*	Ne II	4428.52	V61b	3d 2D	4f 2[3]*	6	8
4430.92	0.043	0.059	4430.90	0.063	0.086	Ne II	4430.94	V61a	3d 2D	4f 2[4]*	6	8
4431.80	0.011	0.015	4431.77	0.011	0.015	N II	4431.82	V55a	3d 3P*	4f 2[3]	5	5
4432.72	0.064	0.087	4432.69	0.062	0.084	N II	4432.74	V55a	3d 3P*	4f 2[3]	5	7
4433.46	0.015	0.021	4433.43	0.015	0.020	N II	4433.48	V55b	3d 3P*	4f 2[2]	1	3
4437.54	0.049	0.067	4437.51	0.043	0.058	He I	4437.55	V50	2p 1P*	5s 1S	3	1
4442.00	0.015	0.021	4441.98	0.037	0.050	N II	4442.02	V55a	3d 3P*	4f 2[3]	3	5
4448.17	0.037	0.050	4448.14	0.011	0.015	O II	4448.19	V35	3p′ 2F*	3d′ 2F	8	8

Table 2 – *continued*

Minor axis			Entire nebula			Ion	λ_0	Mult	Lower Term	Upper Term	g_1	g_2
λ_{obs}	$F(\lambda)$	$I(\lambda)$	λ_{obs}	$F(\lambda)$	$I(\lambda)$							
4452.36	0.032	0.043	4452.33	0.046	0.063	O II	4452.37	V5	3s 2P	3p 2D*	4	4
4457.03	0.036	0.049	4457.01	0.038	0.051	Ne II	4457.05	V61d	3d 2D	4f 2[2]*	4	6
	*	*	*	*	*	Ne II	4457.24	V61d	3d 2D	4f 2[2]*	4	4
4466.39	0.070	0.094	4466.37	0.079	0.106	O II	4466.42	V86b	3d 2P	4f D2*	4	6
4471.49	4.640	6.172	4471.49	4.836	6.432	He I	4471.50	V14	2p 3P*	4d 3D	9	15
4477.89	0.046	0.060	4477.89	0.032	0.043	O II	4477.90	V88	3d 2P	4f G3*	4	6
4481.20	0.033	0.043	4481.20	0.034	0.045	Mg II	4481.21	V4	3d 2D	4f 2F*	10	14
4487.71	0.012	0.016	4487.71	0.008	0.010	O II	4487.72	V104	3d′ 2P	4f′ D2*	2	4
4488.19	0.024	0.032	4488.19	0.016	0.020	O II	4488.20	V104	3d′ 2P	4f′ D2*	4	6
4489.48	0.035	0.046	4489.48	0.024	0.032	O II	4489.49	V86b	3d 2P	4f D2*	2	4
	≲0.03	≲0.04	*	≲0.05	≲0.07	C II	4491.07		4f 2F*	9g 2G	14	18
4491.22	0.073	0.095	4491.22	0.051	0.067	O II	4491.23	V86a	3d 2P	4f D3*	4	6
4510.91	0.204	0.264	4510.92	0.189	0.245	N III	4510.91	V3	3s′ 4P*	3p′ 4D	4	6
	*	*	*	*	*	N III	4510.91	V3	3s′ 4P*	3p′ 4D	2	4
4514.86	0.049	0.064	4514.87	0.076	0.098	N III	4514.86	V3	3s′ 4P*	3p′ 4D	6	8
4518.15	0.051	0.066	4518.16	0.053	0.068	N III	4518.15	V3	3s′ 4P*	3p′ 4D	2	2
4523.58	0.055	0.070	4523.59	0.069	0.089	N III	4523.58	V3	3s′ 4P*	3p′ 4D	4	4
4530.42	0.096	0.122	4530.14	0.141	0.180	N II	4530.41	V58b	3d 1F*	4f 2[5]	7	9
	*	*	*	*	*	N III	4530.86	V3	3s′ 4P*	3p′ 4D	4	2
4534.57	0.079	0.100	4534.59	0.078	0.099	N III	4534.58	V3	3s′ 4P*	3p′ 4D	6	6
4541.58	0.359	0.454	4541.60	0.358	0.453	He II	4541.59	4.9	4f+ 2F*	9g+ 2G	32	*
4552.52	0.080	0.100	4552.54	0.045	0.057	N II	4552.53	V58a	3d 1F*	4f 2[4]	7	9
4562.77	0.044	0.055	4562.55	0.030	0.038	Mg I]	4562.60		3s2 1S	3s3p 3P*	1	5
4571.13	0.131	0.162	4571.17	0.111	0.138	Mg I]	4571.10		3s2 1S	3s3p 3P*	1	3
4591.02	0.115	0.140	4591.24	0.115	0.140	O II	4590.97	V15	3s′ 2D	3p′ 2F*	6	8
4596.21	0.096	0.117	4596.43	0.082	0.100	O II	4596.18	V15	3s′ 2D	3p′ 2F*	4	6
	*	*	*	*	*	O II	4595.96	V15	3s′ 2D	3p′ 2F*	6	6
4601.52	0.045	0.054	4601.75	0.066	0.080	N II	4601.48	V5	3s 3P*	3p 3P	3	5
4602.16	0.086	0.104	4602.40	0.058	0.070	O II	4602.13	V92b	3d 2D	4f F3*	4	6
4607.19	0.060	0.073	4607.43	0.032	0.039	N II	4607.16	V5	3s 3P*	3p 3P	1	3
4609.48	0.196	0.236	4609.71	0.255	0.307	O II	4609.44	V92a	3d 2D	4f F4*	6	8
4610.24	0.078	0.094	4610.47	0.025	0.030	O II	4610.20	V92c	3d 2D	4f F2*	4	6
4613.52	0.036	0.043	4613.51	0.054	0.065	N II	4613.87	V5	3s 3P*	3p 3P	3	3
	*	*	*	*	*	O II	4613.14	V92b	3d 2D	4f F3*	6	6
	*	*	*	*	*	O II	4613.68	V92b	3d 2D	4f F3*	6	8
4619.88	0.039	0.046	4620.29	0.029	0.034	?	*				*	*
4621.43	0.050	0.059	4621.67	0.036	0.043	N II	4621.39	V5	3s 3P*	3p 3P	3	1
4630.58	0.168	0.199	4630.59	0.180	0.214	N II	4630.54	V5	3s 3P*	3p 3P	5	5
4634.17	1.084	1.281	4634.18	1.004	1.187	N III	4634.14	V2	3p 2P*	3d 2D	2	4
4639.93	0.530	0.624	4638.90	0.455	0.536	O II	4638.86	V1	3s 4P	3p 4D*	2	4
4640.67	2.212	2.601	4640.68	2.141	2.518	N III	4640.64	V2	3p 2P*	3d 2D	4	6
4641.85	0.745	0.875	4641.85	0.734	0.863	O II	4641.81	V1	3s 4P	3p 4D*	4	6
4641.88	0.217	0.255	4641.89	0.201	0.236	N III	4641.84	V2	3p 2P*	3d 2D	4	4
4643.12	0.104	0.122	4643.13	0.123	0.144	N II	4643.08	V5	3s 3P*	3p 3P	5	3
4647.48	0.244	0.285	4647.51	0.237	0.278	C III	4647.42	V1	3s 3S	3p 3P*	3	5
4649.19	1.271	1.486	4649.23	1.175	1.374	O II	4649.13	V1	3s 4P	3p 4D*	6	8
4650.31	0.146	0.171	4650.34	0.142	0.166	C III	4650.25	V1	3s 3S	3p 3P*	3	3
4650.90	0.302	0.352	4650.93	0.284	0.332	O II	4650.84	V1	3s 4P	3p 4D*	2	2
4651.53	0.049	0.057	4651.56	0.047	0.055	C III	4651.47	V1	3s 3S	3p 3P*	3	1
4658.26	0.076	0.088	4658.36	0.082	0.096	[Fe III]	4658.10	F3	3d6 5D	3d6 3F2	9	9
4661.68	0.379	0.439	4661.73	0.372	0.431	O II	4661.63	V1	3s 4P	3p 4D*	4	4
4669.32	0.021	0.024	4669.36	0.023	0.026	O II	4669.27	V89b	3d 2D	4f D2*	4	6
4673.79	0.079	0.091	4673.83	0.071	0.081	O II	4673.73	V1	3s 4P	3p 4D*	4	2
4676.29	0.304	0.348	4676.33	0.262	0.300	O II	4676.24	V1	3s 4P	3p 4D*	6	6
4678.19	0.046	0.053	4678.24	0.046	0.053	N II	4678.14	V61b	3d 1P*	4f 2[2]	3	5
4685.78	12.23	13.91	4685.79	11.23	12.77	He II	4685.68	3.4	3d+ 2D	4f+ 2F*	18	32
4694.63	0.041	0.047	4695.26	0.036	0.041	?	*				*	*
4696.45	0.033	0.037	4696.51	0.055	0.062	O II	4696.35	V1	3s 4P	3p 4D*	6	4
4699.32	0.042	0.047	4699.38	0.021	0.023	O II	4699.22	V25	3p 2D*	3d 2F	4	6
4701.96	0.031	0.035	4701.26	0.004	0.004	[Fe III]	4701.62	F3	3d6 5D	3d6 3F2	7	7
4705.45	0.036	0.040	4705.51	0.054	0.060	O II	4705.35	V25	3p 2D*	3d 2F	6	8
4711.49	2.245	2.508	4711.52	2.257	2.521	[Ar IV]	4711.37	F1	3p3 4S*	3p3 2D*	4	6
4713.30	0.603	0.673	4713.32	0.617	0.689	He I	4713.17	V12	2p 3P*	4s 3S	9	3
4724.27	0.028	0.030	*	*	*	[Ne IV]	4724.15	F1	2p3 2D*	2p3 2P*	4	4
4725.75	0.021	0.023	*	*	*	[Ne IV]	4725.62	F1	2p3 2D*	2p3 2P*	4	2
4740.29	2.261	2.472	4740.32	2.138	2.338	[Ar IV]	4740.17	F1	3p3 4S*	3p3 2D*	4	4
4767.73	0.027	0.029	4766.73	0.030	0.032	?	*				*	*
4772.93	0.031	0.033	4773.33	0.016	0.017	Ne II	4772.93		4p 4D*	5d 4F	6	8
4788.27	0.047	0.050	4788.29	0.046	0.049	N II	4788.13	V20	3p 3D	3d 3D*	5	5
	≲0.05	≲0.06	*	≲0.05	≲0.05	C II	4802.23		4f 2F*	8g 2G	14	18
4803.43	0.112	0.117	4803.45	0.097	0.101	N II	4803.29	V20	3p 3D	3d 3D*	7	7

Table 2 – *continued*

Minor axis			Entire nebula			Ion	λ_0	Mult	Lower Term	Upper Term	g_1	g_2
λ_{obs}	$F(\lambda)$	$I(\lambda)$	λ_{obs}	$F(\lambda)$	$I(\lambda)$							
4815.86	0.032	0.033	4815.82	0.030	0.031	S II	4815.55	V9	4s 4P	4p 4S*	6	4
4861.46	100.0	100.0	4861.48	100.0	100.0	H 4	4861.33	H4	2p+ 2P*	4d+ 2D	8	32
4880.53	0.027	0.027	4881.44	0.034	0.033	[Fe III]	4881.11	F2	3d6 5D	3d6 3H	9	9
4891.01	0.037	0.036	4891.08	0.024	0.024	O II	4890.86	V28	3p 4S*	3d 4P	4	2
4903.32	0.022	0.021	4905.04	0.030	0.029	?	*				*	*
4906.98	0.098	0.095	4907.06	0.095	0.092	O II	4906.83	V28	3p 4S*	3d 4P	4	4
4922.08	1.682	1.609	4922.16	1.677	1.604	He I	4921.93	V48	2p 1P*	4d 1D	3	5
4924.68	0.192	0.183	4924.76	0.192	0.184	O II	4924.53	V28	3p 4S*	3d 4P	4	6
4931.30	0.125	0.119	4931.61	0.123	0.117	[O III]	4931.80	F1	2p2 3P	2p2 1D	1	5
4935.54	0.025	0.024	4934.56	0.023	0.022	?	*				*	*
4941.22	0.010	0.010	4941.30	0.018	0.017	O II	4941.07	V33	3p 2P*	3d 2D	2	4
4943.15	0.042	0.039	4943.23	0.011	0.010	O II	4943.00	V33	3p 2P*	3d 2D	4	6
4958.62	316.7	294.7	4958.70	317.6	295.6	[O III]	4958.91	F1	2p2 3P	2p2 1D	3	5
5006.56	953.1	856.4	5006.61	987.4	887.2	[O III]	5006.84	F1	2p2 3P	2p2 1D	5	5
5040.99	0.299	0.262	5040.58	0.207	0.181	Si II	5041.03	V5	4p 2P*	4d 2D	2	4
5047.42	0.176	0.153	5047.36	0.119	0.104	He I	5047.74	V47	2p 1P*	4s 1S	3	1
5056.51	0.120	0.104	5055.93	0.109	0.095	Si II	5055.98	V5	4p 2P*	4d 2D	4	6
	*	*	*	*	*	Si II	5056.31	V5	4p 2P*	4d 2D	4	4
5191.03	0.120	0.094	5191.69	0.125	0.098	[Ar III]	5191.82	F3	2p4 1D	2p4 1S	5	1
5198.77	0.336	0.262	5198.93	0.304	0.238	[N I]	5199.84	F1	2p3 4S*	2p3 2D*	4	4
	*	*	*	*	*	[N I]	5200.26	F1	2p3 4S*	2p3 2D*	4	6
5341.54	0.163	0.115	5340.42	0.140	0.099	C II	5342.38		4f 2F*	7g 2G	14	18
5411.25	1.462	0.980	5411.39	1.511	1.013	He II	5411.52	4.7	4f+ 2F*	7g+ 2G	32	98
5454.42	0.084	0.055	*	*	*	S II	5453.83	V6	4s 4P	4p 4D*	6	8
5517.41	0.868	0.547	5517.51	0.865	0.545	[Cl III]	5517.66	F1	2p3 4S*	2p3 2D*	4	6
5537.50	1.085	0.677	5537.78	1.113	0.694	[Cl III]	5537.60	F1	2p3 4S*	2p3 2D*	4	4
5578.12	0.055	0.034	*	*	*	[O I]	5577.34	F3	2p4 1D	2p4 1S	5	1
5592.90	0.081	0.049	5593.43	0.096	0.058	O III	5592.37	V5	3s 1P*	3p 1P	3	3
5666.54	0.405	0.236	5666.59	0.376	0.220	N II	5666.63	V3	3s 3P*	3p 3D	3	5
5675.93	0.205	0.119	5675.98	0.217	0.126	N II	5676.02	V3	3s 3P*	3p 3D	1	3
5679.48	0.924	0.536	5679.53	0.749	0.434	N II	5679.56	V3	3s 3P*	3p 3D	5	7
5686.13	0.148	0.086	5686.18	0.157	0.091	N II	5686.21	V3	3s 3P*	3p 3D	3	3
5710.68	0.171	0.097	5710.73	0.099	0.057	N II	5710.77	V3	3s 3P*	3p 3D	5	5
5754.48	1.771	0.989	5754.49	1.476	0.825	[N II]	5754.60	F3	2p2 1D	2p2 1S	5	1
5800.65	0.082	0.045	5802.43	0.073	0.040	C IV	5801.51	V1	3s 2S	3p 2P*	2	4
5811.07	0.039	0.021	*	*	*	C IV	5812.14	V1	3s 2S	3p 2P*	2	2
	*	*	5817.06	0.059	0.032	O II	5817.19		5p 4D*	5s′ 2D	4	4
5875.60	35.13	18.47	5875.57	35.63	18.74	He I	5875.66	V11	2p 3P*	3d 3D	9	15
5890.36	0.094	0.049	*	*	*	C II	5890.34	V5	3d 2D	4p 2P*	10	6
5912.53	0.046	0.024	5914.46	0.043	0.022	He II	5913.26	5.26	5g+ 2G	26h+ 2H*	50	*
5928.18	0.065	0.033	5927.72	0.103	0.053	N II	5927.81	V28	3p 3P	3d 3D*	1	3
5932.14	0.096	0.049	5931.69	0.103	0.053	N II	5931.78	V28	3p 3P	3d 3D*	3	5
	*	*	*	*	*	He II	5931.84	5.25	5g+ 2G	25h+ 2H*	50	*
5940.61	0.067	0.034	*	*	*	N II	5940.24	V28	3p 3P	3d 3D*	3	3
5942.02	0.181	0.092	5941.56	0.175	0.089	N II	5941.65	V28	3p 3P	3d 3D*	5	7
5952.76	0.055	0.028	5952.30	0.059	0.030	He II	5952.94	5.24	5g+ 2G	24h+ 2H*	50	*
	*	*	*	*	*	N II	5952.39	V28	3p 3P	3d 3D*	5	5
5978.17	0.079	0.040	5976.54	0.057	0.029	He II	5977.03	5.23	5g+ 2G	23h+ 2H*	50	*
6004.11	0.076	0.038	6004.57	0.068	0.034	He II	6004.73	5.22	5g+ 2G	22h+ 2H*	50	*
6024.94	0.042	0.021	6023.97	0.045	0.022	[Mn V]	6024.40		3d3 4F	3d3 4P	4	4
	*	*	6037.44	0.055	0.027	He II	6036.70	5.21	5g+ 2G	21h+ 2H*	50	*
6074.25	0.121	0.058	*	*	*	He II	6074.10	5.20	5g+ 2G	20h+ 2H*	50	*
6097.07	0.088	0.042	6096.92	0.063	0.030	?	*				*	*
6103.13	0.206	0.097	6102.55	0.273	0.129	[K IV]	6101.83	F1	3p4 3P	3d4 1D	5	5
6117.41	0.155	0.072	6117.60	0.099	0.046	He II	6118.20	5.19	5g+ 2G	19h+ 2H*	50	*
6151.46	0.220	0.101	6150.48	0.165	0.076	C II	6151.43	V16.04	4d 2D	6f 2F*	10	14
6157.94	0.079	0.036	6156.05	0.124	0.057	[Mn V]	6157.60		3d3 4F	3d3 4P	6	4
6167.25	0.090	0.041	6165.52	0.089	0.041	[Mn V]	6166.00		3d3 4F	3d3 4P	8	6
6171.86	0.127	0.058	6171.35	0.167	0.076	He II	6170.60	5.18	5g+ 2G	18h+ 2H*	50	*
	*	*	6197.81	0.046	0.021	O II	6197.92		2p4 2P	3p′ 2F*	4	6
6220.42	0.085	0.038	*	*	*	[Mn V]	6219.10		3d3 4F	3d3 4P	6	2
6234.34	0.155	0.069	6232.97	0.109	0.048	He II	6233.80	5.17	5g+ 2G	17h+ 2H*	50	*
6252.39	0.079	0.035	6251.43	0.040	0.017	?	*				*	*
6259.39	0.082	0.036	6256.97	0.075	0.033	C II	6258.78	V10.03	4p 2P*	5d 2D	4	6
6300.75	2.954	1.272	6300.82	1.815	0.781	[O I]	6300.34	F1	2p4 3P	2p4 1D	5	5
6312.41	3.180	1.362	6312.40	3.088	1.322	[S III]	6312.10	F3	2p2 1D	2p2 1S	5	1
	*	*	*	*	*	He II	6310.80	5.16	5g+ 2G	16h+ 2H*	50	*
6347.17	0.284	0.120	6346.67	0.228	0.096	Si II	6347.10	V2	4s 2S	4p 2P*	2	4
6364.27	1.004	0.420	6364.38	0.568	0.238	[O I]	6363.78	F1	2p4 3P	2p4 1D	3	5
6371.67	0.395	0.165	6371.77	0.362	0.151	Si II	6371.38	V2	4s 2S	4p 2P*	2	2
6394.06	0.112	0.046	6397.69	0.113	0.047	[Mn V]	6393.60		3d3 4F	3d3 4P	10	6

Table 2 – *continued*

Minor axis			Entire nebula			Ion	λ_0	Mult	Lower Term	Upper Term	g_1	g_2
λ_{obs}	$F(\lambda)$	$I(\lambda)$	λ_{obs}	$F(\lambda)$	$I(\lambda)$							
6406.26	0.170	0.070	6406.18	0.157	0.064	He II	6406.30	5.15	5g+ 2G	15h+ 2H*	50	*
6462.09	0.603	0.241	6462.69	0.618	0.248	C II	6461.95		4f 2F*	6g 2G	14	18
6481.96	0.113	0.045	6483.47	0.094	0.037	N II	6482.05	V8	3s 1P*	3p 1P	3	3
6486.61	0.146	0.058	6487.49	0.065	0.026	?	*				*	*
6497.82	0.099	0.039	6497.13	0.131	0.052	?	*				*	*
6501.64	0.208	0.082	6501.78	0.267	0.105	?	*				*	*
6511.07	0.017	0.007	6510.84	0.139	0.055	?	*				*	*
6528.00	0.118	0.046	6526.87	0.136	0.053	He II	6527.11	5.14	5g+ 2G	14h+ 2H*	50	*
6548.70	48.55	18.74	6548.56	39.99	15.43	[N II]	6548.10	F1	2p2 3P	2p2 1D	3	5
6563.30	740.0	283.8	6563.19	772.7	296.3	H 3	6562.77	H3	2p+ 2P*	3d+ 2D	8	18
6584.07	148.0	56.26	6583.94	127.3	48.39	[N II]	6583.50	F1	2p2 3P	2p2 1D	5	5
6678.73	12.74	4.656	6678.69	13.37	4.886	He I	6678.16	V46	2p 1P*	3d 1D	3	5
6717.15	10.36	3.727	6717.07	8.738	3.144	[S II]	6716.44	F2	2p3 4S*	2p3 2D*	4	6
6731.52	16.87	6.032	6731.38	14.62	5.228	[S II]	6730.82	F2	2p3 4S*	2p3 2D*	4	4
6794.69	0.074	0.026	*	*	*	[K IV]	6795.00	F1	3p4 3P	3p4 1D	3	5
7065.67	13.71	4.299	7065.52	13.78	4.321	He I	7065.25	V10	2p 3P*	3s 3S	9	3
7136.16	55.57	16.97	7135.90	61.88	18.89	[Ar III]	7135.80	F1	3p4 3P	3p4 1D	5	5
7161.14	0.195	0.059	7161.30	0.256	0.078	He I	7160.56		3s 3S	10p 3P*	3	9
7170.14	0.240	0.072	7170.94	0.132	0.040	[Ar IV]	7170.62	F2	3p3 2D*	3p3 2P*	4	4
7177.85	0.528	0.159	7177.49	0.344	0.103	He II	7177.50	5.11	5g+ 2G	11h+ 2H*	50	*
7231.44	1.280	0.378	7231.17	1.207	0.356	C II	7231.32	V3	3p 2P*	3d 2D	2	4
7236.85	2.985	0.879	7236.65	2.557	0.753	C II	7236.42	V3	3p 2P*	3d 2D	4	6
	*	*	*	*	*	C II	7237.17	V3	3p 2P*	3d 2D	4	4
	*	*	*	*	*	[Ar IV]	7237.26	F2	3p3 2D*	3p3 2P*	6	4
7263.36	0.153	0.045	7266.30	0.138	0.040	[Ar IV]	7262.76	F2	3p3 2D*	3p3 2P*	4	2
7281.59	1.955	0.566	7281.40	1.938	0.561	He I	7281.35	V45	2p 1P*	3s 1S	3	1
7293.18	0.049	0.014	7295.78	0.165	0.048	?	*				*	*
7297.06	0.131	0.038	7299.66	0.031	0.009	He I	7298.04		3s 3S	9p 3P*	3	9
7320.04	6.722	1.921	7319.59	6.076	1.737	[O II]	7318.92	F2	2p3 2D*	2p3 2P*	6	2
	*	*	*	*	*	[O II]	7319.99	F2	2p3 2D*	2p3 2P*	6	4
7330.34	5.397	1.537	7329.85	5.471	1.558	[O II]	7329.67	F2	2p3 2D*	2p3 2P*	4	2
	*	*	*	*	*	[O II]	7330.73	F2	2p3 2D*	2p3 2P*	4	4

[a] Includes H 14, [S III] λ3722, [O II] λλ3726, 3729 and H 13;
[b] Includes O III λ3791, H 10 and He I λ3806;
[c] Includes [Ne III] λ3967 and H 7.

was used throughout the observations. Two wavelength regions were observed in 1995 and 1997. A 2400 groove mm^{-1} holographic grating was used in first order to cover the λλ3995–4978 wavelength region at a spectral resolution of 1.5 Å FWHM. Three exposures were obtained during each run, each with an integration time of 30 min, except one in 1997 of 1140 s. A second grating in first order, along with a WG345 order-sorting filter, was used to cover the λλ3535–7400 wavelength range, at a resolution of 4.5 Å. The grating had extremely low second-order transmission, and the spectra obtained were free of contamination from second spectral order beyond 6800 Å, up to the end of the wavelength coverage. Both short and long exposures, with typical integration times of 2 and 10 min, were obtained to ensure that strong lines such as Hα and the [O III] λλ4959, 5007 lines were not saturated on the short exposures. In 1996, an extra wavelength range, λλ3040–4040, was observed with the 2400 groove mm^{-1} holographic grating. Three exposures, each of 30-min integration time, were obtained.

In 1995 and 1996, the slit was positioned through the central star and the two bright condensations in PA = 122°.8, roughly defined as the nebular minor axis (Fig. 1). NGC 6153 has an angular size of approximately 27 by 34 arcsec (Fig. 1). Uncertainties may arise from ionization stratification when comparing ionic abundances derived from ground-based narrow-slit optical spectroscopy and from UV and IR observations obtained with space-borne facilities, which use large apertures and thus yield total line fluxes for the whole nebula. To avoid such uncertainties, during the 1997 run the 2-arcsec-wide and ∼3.5-arcmin-long slit of the B&C spectrograph was used to scan uniformly across the whole nebular surface by differentially driving the telescope in Right Ascension. The mean spectra thus obtained, combined with the total Hβ flux measured with a large aperture [$\log F(\mathrm{H}\beta) = -10.86$ erg cm^{-2} s^{-1}; Cahn, Kaler & Stanghellini 1992], yield integrated fluxes over the whole nebula for all lines detected in our deep slit spectra, which are directly comparable to those obtained with the space-borne facilities.

2.1.2 *Data reduction*

The spectra were reduced with standard procedures using the LONG92 package in MIDAS.[1] The spectra were bias-subtracted, flat-fielded and cosmic rays removed, and then wavelength-calibrated using exposures of a He-Ar calibration lamp. During the 1997 run, twilight sky flat-fields were also obtained, which were used to correct the small variations in illumination along the slit, which are ≲1 per cent, except near the edges of the spectral coverage where the peak-to-peak variations amount to about 3 per cent. For the 1995 and 1996 runs, the spectra were flux-calibrated using wide-slit (8-arcsec) observations of the *HST* standard stars Feige 110 and (the nucleus of planetary nebula) NGC 7293 (Walsh 1993). In 1997, the CTIO standard stars LTT 4364, LTT 6248 (Hamuy et al. 1994) and the *HST* standard HD 49798 (Walsh 1993) were used.

[1] MIDAS is developed and distributed by the European Southern Observatory.

Shortwards of 3400 Å, the spectra are affected by ozone absorption bands (Schachter 1991). The bands were not resolved and have a typical width of ~15 Å, i.e., much wider than the nebular emission lines. To remove the ozone absorption, in 1996 the standard stars Feige 110 and the nucleus of NGC 7293 were also observed with a narrow 2-arcsec slit, i.e., the same as that used for nebular observations. Both stars have no noticeable intrinsic absorption features within this wavelength region, except for a weak He II line at 3203 Å in the spectrum of Feige 110. These narrow-slit spectra were used to derive the ozone opacity per unit airmass as a function of wavelength relative to the mean atmospheric extinction curve of the ESO La Silla site. The opacity curve, scaled by the airmasses of the nebular exposures, was then used to divide out the ozone absorption bands. For an airmass of unity, the peak-to-peak corrections amount to ~10 per cent.

Fig. 2 shows the medium-resolution spectra of NGC 6153 from 3540 to 7400 Å, after integrating along the slit. Both the minor-axis spectrum and the mean spectrum for the whole nebula obtained by scanning across the nebular surface are plotted, with prominent features identified. The spectra have not been corrected for interstellar dust extinction. Note the remarkable strengths of the C II λ4267, λλ7231, 7237 and N II λ5670 recombination lines, which stand out clearly even on these spectra of relatively low resolution. Many of the C, N, O and Ne recombination lines fall between 4000 and 4960 Å. Spectra of this wavelength region are plotted in Fig. 3. To accommodate the wide range of line strengths, even amongst the ORLs from heavy-element ions, the spectra were continuum-subtracted (a first-order polynomial was sufficient to fit the continuum for the whole wavelength range plotted), and a constant value of 0.1 added before being plotted in Fig. 3 on a logarithmic scale. The minor-axis spectrum was further scaled down by a factor of 2.5 to separate it from the scanned spectrum for the whole nebula. In Fig. 3, recombination lines from C, N, O and Ne ions are marked above the spectra, whereas those from H I, He I and He II are marked below the spectra along with CELs. The N III lines at 4097, 4634 and 4640 Å are dominated by Bowen fluorescence excitation, and are therefore not suitable for abundance determinations.

A full list of lines and their measured fluxes, detected in the minor-axis and scanned spectra, are presented in Table 2. Columns 1–3 give respectively the observed wavelengths (after correction for Doppler shifts using H I Balmer lines) and the observed $[F(\lambda)]$ and dereddened $[I(\lambda)]$ fluxes from the minor-axis spectrum. Results from the scanned spectrum are listed in columns 4–6. The remaining columns of Table 2 give, in sequence, the ionic identification, laboratory wavelength, multiplet number (with a prefix 'V' for permitted lines and 'F' for forbidden lines), the lower and upper spectral terms of the transition, and the statistical weights of the lower and upper levels. All fluxes are normalized such that $\mathrm{H}\beta = 100$, with the dereddened flux given by

$$I(\lambda) = 10^{c(\mathrm{H}\beta)f(\lambda)}F(\lambda),$$

where $c(\mathrm{H}\beta) = 1.30$ is the logarithmic extinction at $\mathrm{H}\beta$ (cf. Section 3.1), and $f(\lambda)$ is the standard Galactic extinction curve for a total-to-selective extinction ratio of $R = 3.1$ (Howarth 1983).

All the line fluxes tabulated in Table 2 were derived using Gaussian line profile fitting techniques, except for the strongest ones for which the fluxes derived by simply integrating over the line profiles were adopted. NGC 6153 has an [O III] expansion velocity of ~22 km s^{-1} (Anandarao & Banerjee 1988; Meatheringham, Wood & Faulkner 1988), which yields a line profile splitting of 0.66 Å at 4500 Å, smaller than the spectral resolution of 1.5 Å FWHM of our high-resolution spectra. Thus in all cases, the observed linewidths are dominated by instrumental broadening. For blended features, multiple Gaussians of equal linewidths were used to fit the observed profiles. To further constrain the fits, we often made use of the laboratory wavelengths, which are accurately known for nearly all of the identified features, by assuming that the difference between the observed wavelengths of any two blended features is the same as for their laboratory wavelengths. In a few cases where several lines blended closely together and the data were not sufficient to yield unique fluxes for the individual components, we proceeded by fixing the relative intensities of some of the components arising from the same ion until a reasonable fit was achieved. As an example, the broad feature near 4275 Å is a blend of more than 10 O II recombination lines, all from the 3d–4f configuration. After neglecting a few minor components, this whole feature was fitted by the sum of seven Gaussians, with their relative intensities fixed as those predicted by recombination theory (LSBC). Although the fluxes of individual components thus derived do not contain independent information, the fit reproduced well the broad asymmetric profile of the feature. The feature at 4650 Å is a blend of two O II lines at 4649.13 and 4650.84 Å (multiplet V 1) and three C III lines from multiplet V 1. The whole blend was fitted by assuming that the C III λλ4647.42, 4650.25 and 4651.47 lines have intensity ratios of 5:3:1, as predicted for *LS*-coupling. As a final example, the intensity ratio of the [S II] λλ4068, 4075 doublet is found to be nearly independent of T_e and N_e for the nebular conditions of concern here. In fitting the 4065–4082 Å region, we have therefore fixed the intensity ratio to $\lambda4075/\ \lambda4068 = 0.337$, the value predicted for $T_e = 9100$ K and $N_e = 3500$ cm^{-3} (cf. Section 3.2).

Typical line flux errors are estimated to be less than 5 per cent for lines with observed fluxes $F(\lambda) \geq 0.2$ [in units of $F(\mathrm{H}\beta) = 100$], 10 per cent for those with $0.1 \leq F(\lambda) < 0.2$, 20 per cent for $0.05 \leq F(\lambda) < 0.1$, and 30 per cent or higher for lines with $F(\lambda) < 0.05$. For a given flux range, the errors for lines

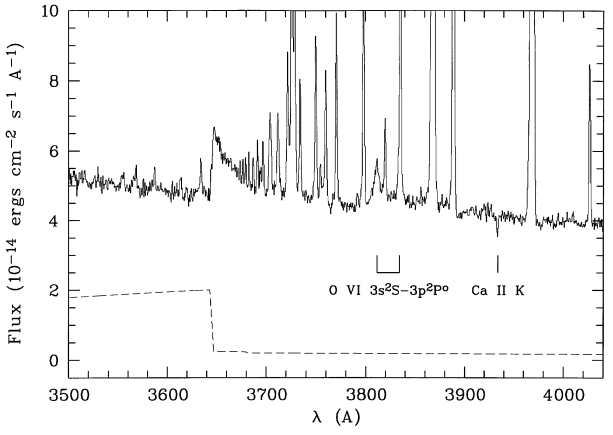

Figure 4. Dereddened spectrum of the central star of NGC 6153 from 3500 to 4040 Å after subtraction of the nebular continuum (dashed line), showing the broad stellar O VI λ3811 line and the Ca II K absorption line at 3933.66 Å which, at 18 ± 7 km s^{-1}, is blueshifted by 27 km s^{-1} relative to the nebular systemic velocity as measured from the adjacent Balmer lines. Apart from the O VI and Ca II K lines, all other lines present in the spectrum are of nebular origin. The broad feature redwards of 3646 Å is due to the converging high-order Balmer lines.

shortwards of 3400 Å are somewhat larger, due to the decreasing CCD efficiency and the effects of ozone absorption.

2.1.3 *O* VI *emission from the central star*

A broad emission line, identified as O VI $3s\,^2S–3p\,^2P^o$ λ3811.35 (multiplet 1), has been detected from the central star of NGC 6153. Fig. 4 shows the spectrum of the star from 3500 to 4040 Å. The spectrum was extracted from the long-slit minor-axis spectrum by integrating over a slit length of 4.89 arcsec centred on the position of the central star. After correcting for extinction using a reddening constant of $c(\mathrm{H}\beta) = 1.30$ (cf. Section 3.1), the contribution from the nebular continuum was subtracted. The nebular continuum was calculated from the flux of Hϵ at 3970 Å, using an electron temperature of 6000 K as derived from the ratio of the nebular continuum Balmer discontinuity to H 11, an electron density of 3500 cm^{-3}, and He ionic abundances of $\mathrm{He}^+/\mathrm{H}^+ = 0.118$ and $\mathrm{He}^{2+}/\mathrm{H}^+ = 0.019$ (cf. Section 3.2 Tables 6 and 9, and Sections 4.2, 4.3, Figs 14–16). The λ3811 feature has an observed peak wavelength of 3811.36 Å, after correcting for the nebular radial velocity measured from nearby Balmer lines. This wavelength agrees very well with the rest wavelength of 3811.35 Å of the stronger component of the O VI $3s\,^2S–3p\,^2P^o$ $\lambda\lambda$3811, 3834 doublet. It has a FWHM of 5.7 Å, about 4 times larger than the instrumental width of 1.5 Å FWHM, confirming that it is a stellar emission line. After the nebular continuum subtraction, the line has an emission equivalent width of 2.3 ± 0.5 Å. The other component of the O VI doublet, at 3834.24 Å, is lost in the strong nebular H 9 line at 3835.35 Å. For optically thin emission, the λ3834.24 line should have an intensity half that of the λ3811.35 line. Apart from the O VI λ3811 line, no other stellar emission lines are detected, except possibly the C IV $3s\,^2S–3p\,^2P^o$ doublet at 5801 and 5812 Å, with estimated equivalent widths of 1.4 ± 0.3 and 0.8 ± 0.2 Å. The lines are not resolved at the spectral resolution of 4.5 Å FWHM available for this wavelength region. However, nebular emission in these lines would not be expected from a PN of NGC 6153's excitation class.

The detection of broad O VI λ3811.35 emission from the central star, as well as C IV $\lambda\lambda$5801,12 emission, implies that it is hydrogen-deficient (Mendez 1991). Central stars showing these features in emission were originally classified by Smith & Aller (1969) as members of an O VI 'sequence'. Those which show these lines strongly in emission have been classified as WO stars by Crowther, De Marco & Barlow (1998), while those showing them only weakly in emission have been classified as [WC]–PG1159 WEL (weak emission line) stars by Parthasarathy, Acker & Stenholm (1998). The relative weakness of its O VI and C IV lines puts the central star of NGC 6153 in the latter category, similar to the central stars of Abell 30 and Abell 78, which have well-known hydrogen-deficient central nebular condensations. We shall return to the possible significance of this link in Section 6.

2.1.4 *Ca* II *absorption*

The Ca II $4s\,^2S_{1/2}–4p\,^2P^o_{3/2}$ K line at 3933.66 Å is clearly detected in absorption in our deep spectrum (Fig. 4). The H component of the Ca II doublet, at 3968.47 Å, is lost in the strong emission from the [Ne III] λ3967.46 line and Hϵ λ3970.07. The K line has an equivalent width of 0.20 ± 0.04 Å, and is almost certainly saturated unless it consists of several unresolved components at different radial velocities. At a radial velocity of $V_{\mathrm{LSR}} = 18 \pm 7\,\mathrm{km\,s^{-1}}$, the absorption line is blueshifted by 27 $\mathrm{km\,s^{-1}}$ relative to the nebular radial velocity ($V_{\mathrm{LSR}} = +44.9\,\mathrm{km\,s^{-1}}$; Schneider et al. 1983), i.e., approximately the same as the nebular expansion velocity (Anandarao & Banerjee 1988; Meatheringham et al. 1988). The predicted Galactic rotational velocity towards NGC 6153 ($l = 341.^\circ8$, $b = 5.^\circ4$) remains negative out to distances $d > 10$ kpc. At the Shklovsky distance of 1.3 kpc for NGC 6153 (Cahn et al. 1992), the Galactic rotation curve predicts a radial velocity of $\sim -10\,\mathrm{km\,s^{-1}}$ (Fich, Blitz & Stark 1989). Thus, despite the large interstellar extinction towards NGC 6153 (Section 3.1), the measured radial velocity of the Ca II K line suggests that the absorption arises from a neutral envelope around NGC 6153, rather than from intervening diffuse clouds along the line of sight towards NGC 6153. On the other hand, the weakness of the [O I] $\lambda\lambda$6300, 6363 and [N I] $\lambda\lambda$5198, 5200 emission lines from NGC 6153 (Table 2), and the non-detection of the [O I] 63-, 146-μm and [C II] 158-μm lines after background subtraction (Table 3), suggest that NGC 6153 has little neutral material and is probably matter-bounded rather than ionization-bounded. Observations of higher spectral resolution would be invaluable in clarifying the origin of the strong Ca II K line absorption detected towards NGC 6153.

2.2 Far-infrared spectroscopy with the *ISO* LWS

NGC 6153 was observed with the Long Wavelength Spectrometer (LWS; Clegg et al. 1996) on board the *Infrared Space Observatory* (*ISO*; Kessler et al. 1996) during *ISO* Rev. 84 on 1996 February 9, as part of the LWS Post-Main-Sequence Guaranteed Time Programme in which more than 30 Galactic PNe have been observed with the LWS. Fig. 5 shows the on- and off-source LWS spectra of NGC 6153. Due to extended background emission, there is some continuum fringing longwards of 120 μm, which is removed after the background subtraction. A full list of line fluxes measured in our GT programme will be reported by Liu et al. (in preparation; cf. Liu 1997 for some preliminary results). For convenience, lines fluxes for NGC 6153, on- and off-source, are also given here in Table 3. Note that the 'on-off' fluxes were not values obtained by simply subtracting the 'off' fluxes from the 'on' ones; instead, they were measured directly from the background-subtracted spectrum, which is free of fringing. The LWS has a beamsize of ~70 arcsec, big enough to capture emission from the entire nebula of NGC 6153. Only three ionic lines have been

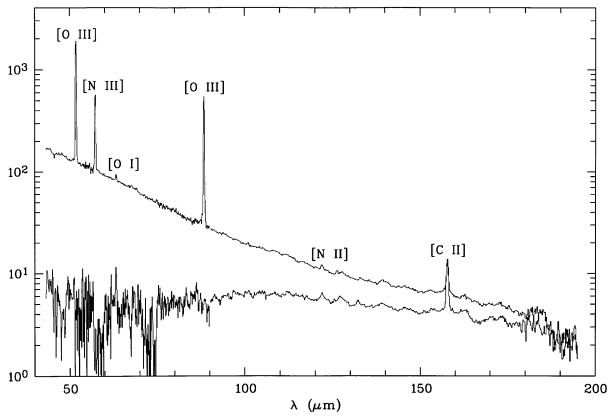

Figure 5. On- (source plus background; upper curve) and off-source (lower curve) far-IR spectra of NGC 6153 obtained with the Long Wavelength Spectrometer on board the *Infrared Space Observatory*. The flux is in units of $10^{-12}\,\mathrm{erg\,cm^{-2}\,s^{-1}\,\mu m^{-1}}$.

Table 3. *ISO* LWS fluxes.

Line	$F(\lambda)$ (10^{-12} erg cm^{-2} s^{-1})			$I(\lambda)$ [$I(\mathrm{H}\beta) = 100$]		
	on	off	on-off	on	off	on-off
[O III] 52 μm	570	≤5	570	267	≤2	266
[N III] 57 μm	153	≤2	155	72	≤1	72
[O I] 63 μm	4.2	2.9	≤2	2.0	1.3	≤.7
[O III] 88 μm	158	≤.8	158	74	≤.4	74
[N II] 122 μm	.66	.82	≤.4	.31	.39	≤.2
[O I] 146 μm	≤.2	.30	≤.2	≤.1	.14	≤.1
[C II] 158 μm	4.9	5.6	≤.3	2.3	2.6	≤.1

detected from NGC 6153, the [O III] 52- and 88-μm and [N III] 57-μm lines. The [O I], [N II] and [C II] lines seen in the on-source spectrum are entirely due to Galactic background emission. The last three columns of Table 3 give line fluxes after normalization to $\mathrm{H}\beta = 100$, assuming a dereddened total $\mathrm{H}\beta$ flux of $\log I(\mathrm{H}\beta) = -9.67$ erg cm^{-2} s^{-1} (cf. Section 3.1).

2.3 The *IRAS* LRS mid-infrared spectrum

The 7.6–22.7 μm mid-infrared spectrum of NGC 6153 was observed with the Low-resolution spectrometer on board the *IRAS* satellite (Pottasch et al. 1984; PDM). Although the *ISO* Short Wavelength Spectrometer (SWS) spectrum of NGC 6153 obtained by the SWS Consortium covers a wider wavelength range (2.4–45 μm) with much improved spectral resolution and sensitivity, the LRS spectrum has the advantage that it yields the total nebular line fluxes because of its large aperture of at least 2 arcmin, compared to the aperture of 14×20 arcsec^2 for SWS bands 1–2 (2.4–12 μm), 14×27 arcsec^2 for bands 3A, 3C and 3D (12–27.5 μm), 20×27 arcsec^2 for band 3E (27.5–29 μm) and 20×33 arcsec^2 for band 4 (29–45.2 μm). Given the nebular angular size of NGC 6153 (~27×34 arcsec^2; Fig. 1), the SWS spectrum is expected to miss part of the emission from NGC 6153, especially for SWS bands 1–2. We have extracted, recalibrated and spliced the LRS blue and red spectra, and have appended wavelength-specific absolute uncertainties to the data of NGC 6153, in accordance with the techniques described by Cohen, Walker & Witteborn (1992). The recalibrated spectrum is plotted in Fig. 6, and the measured line fluxes are listed in Table 4. The [S IV] 10.5-μm line flux from the recalibrated spectrum is 1.7 times higher than listed by PDM, whereas that of the [Ne III] 15.5-μm line is 1.4 times smaller. The intensities of lines detected by the LRS, normalized to $\mathrm{H}\beta = 100$ assuming a dereddened total $\mathrm{H}\beta$ flux of $\log I(\mathrm{H}\beta) = -9.67$ erg cm^{-2} s^{-1} (cf. Section 3.1), are given in the last column of Table 4.

2.4 The *IUE* observations

NGC 6153 was observed by the *IUE* on 1984 October 1, 1986 February 24 and 1988 August 13. On each occasion, low-resolution spectra were obtained with both the Short Wavelength and the Long Wavelength Prime cameras, covering the wavelength ranges 1150–1975 and 1910–3300 Å. All observations were obtained with the *IUE* large aperture, a 10.3×23 arcsec^2 oval. Two exposures were obtained in 1984, with exposure times of 1800 and 7200 s for the LWP camera (LWP04475L and LWP04476L) and 3600 and 10 020 s for the SWP camera (SWP24092L and SWP24093L). The exposure times for the

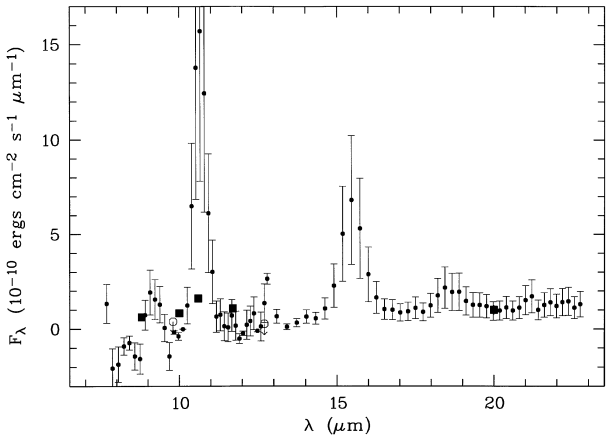

Figure 6. The recalibrated *IRAS* LRS spectrum of NGC 6153. Filled squares (or open circles with a down arrow for upper limits) are ground-based 18-arcsec-aperture photometric data from Cohen & Barlow (1980).

Table 4. *IRAS* LRS fluxes.

Line	$F(\lambda)$ (10^{-10} erg cm^{-2} s^{-1})	$I(\lambda)$ [$I(\mathrm{H}\beta) = 100$]
[Ar III] 9.0 μm	1.2	56
[S IV] 10.5 μm	7.7	360
[Ne II] 12.8 μm	0.5	23
[Ne III] 15.5 μm	5.4	252
[S III] 18.7 μm	1.0	47

LWP and SWP cameras in 1986 were respectively 6660 and 12 600 s (LWP07715L and SWP27779L) and 10 200 and 3600 s in 1988 (LWP13841L and SWP34077L). The calibrated spectra are available from the *IUE* Final Archive at the ESA centre in Vilspa. The retrieved data were co-added, weighted by the integration time. The average SWP spectrum is plotted in Fig. 7, with the three detected lines labelled. The spectrum shows a significant improvement in signal-to-noise (S/N) ratio compared to that analysed by PDM, although no extra lines were detected. In the LWP wavelength region, apart from the strong O III Bowen fluorescence line at 3133 Å, three weak lines are detected – the O III Bowen lines at 2837 and 3047 Å and the He II 6–3 line at 2733 Å. The derived line fluxes are listed in Table 5.

The angular size of NGC 6153 (Fig. 1) is bigger than the *IUE* large aperture. The position angles of the major axis of the *IUE* large aperture during the 1984, 1986 and 1988 observations were 1°, 170° and 345° respectively. We note that the coordinates pointed at by *IUE* during the 1984 and 1986 runs were $\alpha(1950) = 16^{\mathrm{h}}28^{\mathrm{m}}05^{\mathrm{s}}$, $\delta(1950) = -40°08'50''$, which differ by 8 arcsec from those given by Milne (1973) and $\alpha(1950) = 16^{\mathrm{h}}28^{\mathrm{m}}05^{\mathrm{s}}$, $\delta(1950) = -40°08'58''$, which were adopted for the 1988 observations. The He II λ1640 fluxes derived from the three observations however agree within the uncertainties. On the other hand, the logarithmic $\mathrm{H}\beta$ extinction constant $c(\mathrm{H}\beta) = 1.63$, derived from the ratio of the *IUE* λ1640 line flux to the λ4686 line flux derived from our optical scanned spectrum (Table 2, column 5), is more than 0.3 dex larger than the reddening constants derived from either the observed H I Balmer decrement or from the ratio of the 5 GHz *free–free* radio continuum to $\mathrm{H}\beta$, suggesting that the *IUE* observations may have captured only half the λ1640 emission from NGC 6153. The O III λ3133 line was well detected in our ground-based optical spectrum taken along

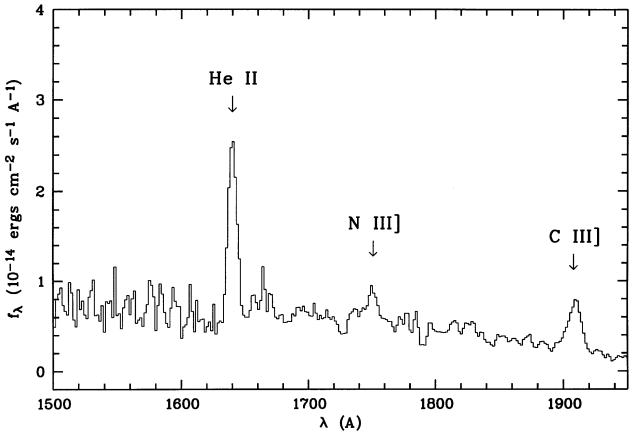

Figure 7. The *IUE* large-aperture spectrum of NGC 6153 from 1500 to 1950 Å.

Table 5. *IUE* fluxes.

Line	$F(\lambda)$ (10^{-14} erg cm^{-2} s^{-1})	$I(\lambda)$ [$I(\mathrm{H}\beta) = 100$]
C IV λ1549	≲5	≲30
He II λ1640	16.5	81.7
O III] λ1663	≲4	≲20
N III] λ1751	3.44	16.2
C III] λ1908	7.10	46.2
He II λ2733	1.4:	1.8:
O III λ2837	4.1:	4.2:
O III λ3047	2.9:	2.0:
O III λ3133	38.6	24.0

the nebular minor axis, with an observed flux relative to Hβ of 0.0667 (Table 2, column 2), which together with a total Hβ flux of $\log F(\mathrm{H}\beta) = -10.86$ erg cm^{-2} s^{-1} (Cahn et al. 1992) yields a total λ3133 flux of 9.2×10^{-13} erg cm^{-2} s^{-1}, 2.4 times higher than that measured with the *IUE*, again suggesting that the *IUE* may have missed half the nebular emission from NGC 6153. Since only about 10 per cent of He is doubly ionized in NGC 6153 (cf. Section 3.5, Table 9), and since both the He II λ1640 line and the O III λ3133 Bowen fluorescence line are likely to arise from only a small inner region of high ionization degree, the fact that the *IUE* captured only half the total fluxes from these two lines is somewhat puzzling.

In order to normalize the *IUE* fluxes to Hβ, we first dereddened the *IUE* spectrum using a reddening constant of $c(\mathrm{H}\beta) = 1.30$ (Section 3.1) and then normalized the dereddened fluxes such that He II $I(\lambda1640)/I(\lambda4686) = 6.43$, the ratio predicted by case B recombination of He II for $T_\mathrm{e} = 9100$ K and $N_\mathrm{e} = 3500$ cm^{-3} (Storey & Hummer 1995). The results are listed in the last column of Table 5.

3 NEBULAR ANALYSIS

3.1 Reddening summary

Using the Galactic reddening law of Howarth (1983), the observed Balmer Hα/Hβ, Hγ/Hβ and Hδ/Hβ decrements yield an average logarithmic extinction at Hβ of $c(\mathrm{H}\beta) = 1.27 \pm 0.06$ and 1.30 ± 0.01, from the scanned and the minor-axis spectra respectively. The observed ratio of He II λ3203/λ4686 on the minor axis yields $c(\mathrm{H}\beta) = 1.38$. For $T_\mathrm{e} = 9100$ K, $\mathrm{He}^{2+}/\mathrm{H}^+ = 0.01$ and $\mathrm{He}^+/\mathrm{H}^+ = 0.12$ (Tables 6 and 9), the 5-GHz free–free radio continuum flux density, $S(5\,\mathrm{GHz}) = 0.632$ Jy, and the total Hβ flux, $\log F(\mathrm{H}\beta) = -10.86$ erg cm^{-2} s^{-1} (Cahn et al. 1992), give $c(\mathrm{H}\beta) = 1.19$ [or $c(\mathrm{H}\beta) = 1.27$ for $T_\mathrm{e} = 6080$ K, the temperature derived from the nebular continuum Balmer discontinuity; Table 6]. From the He II λ4686 flux of the scanned optical spectrum and the *IUE* λ1640 flux we find $c(\mathrm{H}\beta) = 1.63$, significantly higher than those derived from the H I Balmer decrement and from the radio continuum flux density. As discussed in Section 2.4, the discrepancy is probably caused by the fact that the *IUE* may have captured only half the λ1640 emission from NGC 6153 in its 10.3×23 arcsec^2 oval aperture. We dereddened both the *IUE* and the optical spectra with $c(\mathrm{H}\beta) = 1.30$. For the IR lines, they were normalized to Hβ using a dereddened flux of $\log I(\mathrm{H}\beta) = \log F(\mathrm{H}\beta) + c(\mathrm{H}\beta) = -9.67$ erg cm^{-2} s^{-1}, where $c(\mathrm{H}\beta) = 1.19$ as derived from the radio continuum flux density. [For $c(\mathrm{H}\beta) = 1.27$, the intensities of all IR lines relative to Hβ (Tables 3 and 4), and thus the ionic abundances deduced from them (Table 8), should be reduced by 0.08 dex, i.e., multiplied by 0.832.]

Table 6. Plasma diagnostics.

Diagnostic	Minor axis	Entire nebula
	T_e (K)	
[O III] (88 μm + 52 μm)/(λ4959 + λ5007)		7210/8380[a]
[Ne III] 15.5 μm/(λ3868 + λ3967)		8620
[O III] (λ4959 + λ5007)/λ4363	9140	9110
[Ar III] λ7135/λ5192	9400	9200
[N II] (λ6548 + λ6584)/λ5754	10310[b]	10220[b]
[O II] (λ7320 + λ7330)/λ3727	16410[c]	17910[c]
BJ/H 11	6080	
	N_e (cm^{-3})	
[O III] 88 μm/52 μm		1660
[Ar IV] λ4740/λ4711	3050	2400
[Cl III] λ5537/λ5517	3540	3830
[O II] λ3729/λ3726	3340	
[S II] λ6731/λ6716	3530	3970
Balmer decrement	2000	

[a] For $N_\mathrm{e} = 3500$ and 1660 cm^{-3} respectively;
[b] Neglecting recombination excitation of the auroral λ5754 line (cf. Section 3.3);
[c] Neglecting recombination excitation of both the nebular and auroral lines (cf. Section 3.3).

3.2 Electron temperatures and densities

The electron temperatures and densities derived from various CEL diagnostic ratios are given in Table 6, obtained by solving the level populations for multilevel (≥5) atomic models. References for the adopted atomic data are listed in Table 7. For the scanned data, only low-resolution spectra (FWHM 4.5 Å) are available for the [O II] λλ3726, 3729 doublet, which is blended with H 14, [S III] λ3722 and H 13. The contributions of the latter lines were subtracted assuming that their intensities (relative to Hβ) are the same as measured on the high-resolution spectra taken along the minor axis. Similarly, on the low-resolution spectra, [Ne III] λ3967 is blended with Hε and was corrected for using the Hε intensity measured from the minor-axis high-resolution spectrum. The [O II] λ7330 line is blended with the [Ar IV] λ7331 line. From the observed intensity of the [Ar IV] λ7263 line, we find that the

Table 7. References for atomic data.

Ion	Collisionally excited lines	
	Transition probabilities	Collision strengths
C III	Keenan et al. 1992 Fleming et al. 1996	Keenan et al. 1992
N II	Nussbaumer & Rusca 1979	Stafford et al. 1994
N III	Fang et al. 1993	Blum & Pradhan 1992
O II	Zeippen 1982	Pradhan 1976
O III	Nussbaumer & Storey 1981	Aggarwal 1983
Ne II	Mendoza 1983	Bayes et al. 1985
Ne III	Mendoza 1983	Butler & Zeippen 1994
Ne IV	Zeippen 1982	Giles 1981
S II	Mendoza & Zeippen 1982a Keenan et al. 1993	Keenan et al. 1996
S III	Mendoza & Zeippen 1982b	Mendoza 1983
S IV	Storey (unpublished)	Saraph & Storey 1999
Cl III	Mendoza & Zeippen 1982a	Butler & Zeippen 1989
Ar III	Mendoza & Zeippen 1983	Johnson & Kingston 1990
Ar IV	Mendoza & Zeippen 1982a	Zeippen et al. 1987

	Optical recombination lines	
Ion	Effective recomb. coeffs.	Case
H I	Storey & Hummer 1995	B
He I	Brocklehurst 1972	B: singlets A: triplets
He II	Storey & Hummer 1995	B
C II	Davey et al. 1999	B
C III	Péquignot et al. 1991 Nussbaumer & Storey 1984	A
N II	Escalante & Victor 1990	B: triplets A: singlets
N III	Péquignot et al. 1991 Nussbaumer & Storey 1984	A
O II	Storey 1994	B: quartets
	Liu et al. 1995a	A: doublets
Ne II	Kisielius et al. 1998	B: doublets
	Storey (unpublished)	A: quartets

[Ar IV] λ7331 line contributes less than 1 per cent of the observed flux of the 7330-Å feature and so can be ignored.

The derived electron densities from the density diagnostics listed in Table 6 depend little on the assumed temperature, and so a constant value of 9100 K was used, as derived from the T_e-sensitive [O III] nebular to auroral line ratio. We note that the [O II] nebular lines may be excited by recombination as well as by collisions (see Section 3.3). However, this will not affect the λ3729/λ3726 ratio, and therefore it remains as a valid density diagnostic.

The electron temperatures listed in Table 6 were derived for a density of $3500\,\mathrm{cm}^{-3}$, the average value returned by the four optical N_e-diagnostics. For this relatively low density, the derived temperatures are insensitive to the adopted N_e, except for that deduced from the [O III] $(88\,\mu\mathrm{m} + 52\,\mu\mathrm{m})/(\lambda4959 + \lambda5007)$ ratio, due to the fairly low N_{crit} values (see Osterbrock 1989) of the 52- and 88-μm lines, and those deduced from the [O II] auroral to nebular line ratio. For the former diagnostic, the temperature obtained for $N_e = 1660\,\mathrm{cm}^{-3}$, the value given by the density-sensitive 88 μm/52 μm ratio, is also listed in Table 6. For $N_e =$ 1660 and $3500\,\mathrm{cm}^{-3}$, the temperatures derived from the $(88\,\mu\mathrm{m} + 52\,\mu\mathrm{m})/(\lambda4959 + \lambda5007)$ ratio are respectively 730 and 1900 K lower than the value of 9110 K deduced from the [O III] optical nebular to auroral line ratio. For the [O II] $(\lambda7320 + \lambda7330)/\lambda3727$ auroral to nebular diagnostic ratio, lowering N_e from the adopted value of $3500\,\mathrm{cm}^{-3}$ will dramatically increase the resultant temperatures – surpassing 2×10^4 K for $N_e = 2500\,\mathrm{cm}^{-3}$.

The [Ne III] 15.5-μm line has a much higher N_{crit} than the [O III] fine-structure lines. The electron temperatures derived from the 15.5-μm/(λ3868 + λ3967) ratio for $N_e = 3500$ and $1660\,\mathrm{cm}^{-3}$ differ by only 40 K, and are about 500 K lower than that derived from the [O III] optical nebular to auroral line ratio.

The [Ar III] 9.0-μm line also has a high N_{crit}, similar to that of the [Ne III] 15.5-μm line. The 9.0-μm line is, however, much weaker, and its flux measured from the LRS spectrum is very uncertain. The T_e-diagnostic ratio [Ar III] 9.0 μm/λ7135 was therefore not used. The [Ar III] λ5192 auroral line is only marginally detected in our optical low-resolution spectra. The electron temperatures given by the λ7135/λ5192 ratio are not far from those deduced from the [O III] nebular to auroral line ratio (Table 6).

The electron densities derived from the four optical diagnostic ratios agree remarkably well. In contrast, N_e deduced from the [O III] far-IR fine-structure line ratio 88 μm/52 μm is about a factor of 2 lower. The ionization potential of O^+, 35.1 eV, falls between those of Cl^+ and Ar^{2+}, 23.8 and 40.7 eV respectively, and we expect that the [O III], [Cl III] and [Ar IV] lines all arise from similar ionization regions. The fact that the [Cl III] and [Ar IV] doublets yield similar densities which are a factor of 2 higher than given by the [O III] far-IR line ratio suggests the presence of moderate density inhomogeneity in the nebula – the [O III] far-IR lines are quenched by collisional de-excitation in high-density condensations because of their low critical densities,[2] 500 and $3500\,\mathrm{cm}^{-3}$ respectively for the 88- and 52-μm lines, significantly lower than those of the [Cl III] and [Ar IV] doublets (6400, 34 000, 14 000 and $130\,000\,\mathrm{cm}^{-3}$ for the λλ5517, 5537, 4711 and 4740 lines respectively). The implications of density fluctuations for abundance determinations will be addressed in Section 5.4.

Together with the temperatures derived from CEL ratios, Table 6 also gives the mean Balmer jump temperature along the nebular minor axis, derived from the ratio of the nebular continuum Balmer discontinuity at 3646 Å to H 11 λ3770 (Fig. 8). The Balmer jump temperature for the whole nebula is not listed because of the lack of a high-resolution spectrum for this wavelength region. We used the ratio of the Balmer discontinuity to H 11 rather than to Hβ, since the temperature thus derived is much less sensitive to uncertainties in the reddening correction and flux calibration, given the small wavelength difference between the Balmer discontinuity and H 11. In addition to the H I Balmer discontinuity at 3646 Å, the He I and He II continua also have weak discontinuities, at 3678 and 3646 Å respectively, which contribute to the observed magnitude of the continuum jump and cannot be easily separated from the H I Balmer jump. The Balmer jump temperature was therefore derived by comparing the observed and predicted values of the Balmer jump to H 11 ratio, defined as $[I_c(\lambda3643) - I_c(\lambda3681)]/I(\mathrm{H}\,11)$, where $I_c(\lambda3643)$ and $I_c(\lambda3681)$ are the nebular continua at 3643 and 3681 Å respectively. The temperature thus deduced has a weak dependence on the He^+/H^+ and He^{2+}/H^+ abundance ratios. In Fig. 9, the predicted $[I_c(\lambda3643) - I_c(\lambda3681)]/I(\mathrm{H}\,11)$ ratio as a function of T_e is plotted for three He ionic abundance combinations. The emissivities of the H I Balmer lines and of the H I, He I and He II continua were taken respectively from Storey & Hummer (1995) and Brown & Mathews (1970). From the high-resolution minor-axis spectrum of NGC 6153, we find $[F_c(\lambda3643) - F_c(\lambda3681)]/F(\mathrm{H}\,11) = 0.151$ and, after reddening corrections, $[I_c(\lambda3643) - I_c(\lambda3681)]/I(\mathrm{H}\,11) = 0.161$, which,

[2] Throughout the paper, critical densities, N_{crit}, are quoted for an electron temperature of 10^4 K.

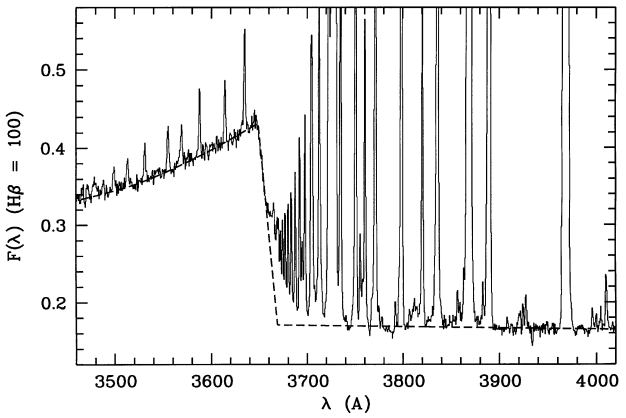

Figure 8. The far-blue minor-axis spectrum of NGC 6153 from 3460 to 4020 Å, showing the nebular continuum Balmer discontinuity at 3646 Å. The ratio of the Balmer jump to H 11 λ3770 yields an electron temperature of 6080 K, about 3000 K lower than derived from the [O III] nebular to auroral line ratio. The dashed line is a two-part fit to the continuum, bluewards and redwards of the Balmer jump. The observed continuum level includes a small contribution from the central star. The stellar continuum is, however, expected to be smooth over the plotted wavelength range and thus should not affect the magnitude of the observed Balmer discontinuity. The spectrum has not been corrected for extinction and is normalized such that $F(\mathrm{H}\beta) = 100$.

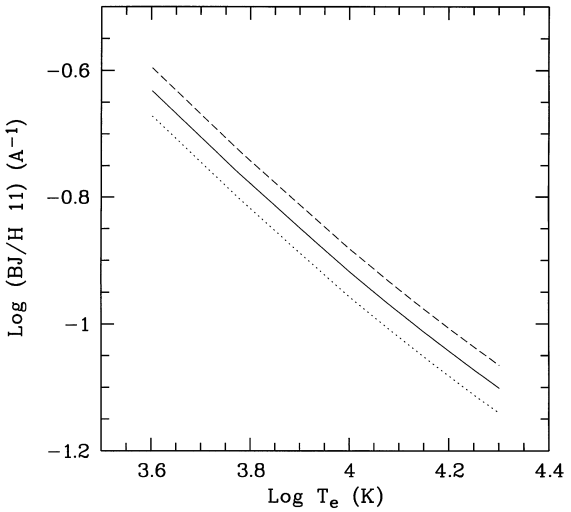

Figure 9. The Balmer discontinuity to H 11 ratio, $\mathrm{BJ/H\,11} \equiv [I_c(\lambda3681) - I_c(\lambda3643)]/I(\mathrm{H11})$, as a function of T_e for (a) $\mathrm{He^+/H^+} = 0.1$ and $\mathrm{He^{2+}/H^+} = 0$ (dotted line), (b) $\mathrm{He^+/H^+} = \mathrm{He^{2+}/H^+} = 0.05$ (solid line), and (c) $\mathrm{He^+/H^+} = 0$ and $\mathrm{He^{2+}/H^+} = 0.1$ (dashed line). $I_c(\lambda3643)$ and $I_c(\lambda3681)$ are the nebular continuum fluxes at 3643 and 3681 Å respectively, which bracket the H Balmer discontinuity at 3646 Å and two weak discontinuities at 3646 (He II) and 3678 Å (He I). The relation can be fitted with a power law $T_e = a(\mathrm{BJ/H\,11})^{-1.5}$ (K), where BJ/H 11 is in units of $\mathrm{Å}^{-1}$ and $a = 377$, 432 and 490 for cases (a), (b) and (c) respectively.

together with the He ionic abundances derived in Table 9, yield $T_e(\mathrm{BJ}) = 6080$ K. The value is probably accurate to about 500 K. For comparison, $[I_c(\lambda3643) - I_c(\lambda3681)]/I(\mathrm{H}\beta) = 6.00 \times 10^{-3}$, yielding $T_e(\mathrm{BJ}) = 6380$ K.

The Balmer jump temperature of 6080 K deduced for NGC 6153 is just over 3000 K lower than the [O III] forbidden line temperature T_e([O III]). That T_e(BJ) can be significantly lower than

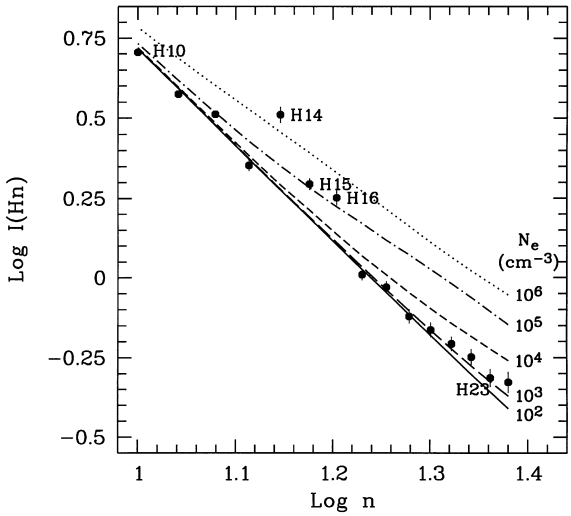

Figure 10. Observed intensities (in units where $\mathrm{H}\beta = 100$) of high-order Balmer lines ($n \rightarrow 2$, $n = 10, 11, \ldots, 24$) as a function of the principal quantum number n. H 14 at 3721.94 Å is blended with the [S III] λ3721.63 line. H 15 at 3711.97 Å and H 16 at 3703.86 Å may also be contaminated by some weak unknown lines. The various curves show respectively the predicted Balmer decrements for electron densities from $N_e = 10^2$ to $10^6\,\mathrm{cm^{-3}}$. A constant temperature of 6000 K, approximately the value derived from the nebular continuum Balmer discontinuity, has been assumed in all cases.

T_e([O III]) for the same nebula was first observed by Peimbert (1971) for several PNe and the H II region M 42, and was interpreted by him as caused by the presence of large temperature fluctuations in the nebulae (Peimbert 1967). The emissivity of the nebular continuum, produced by radiative recombination of the H and He ions with electrons, has a negative, power-law dependence on T_e. In contrast, the emissivities of CELs, such as the [O III] nebular and auroral lines, increase exponentially as a function of T_e. Thus for a thermally inhomogeneous nebula, the CEL emission from the nebula will be strongly biased towards the high-temperature regions, whereas the continuum emission will be biased towards regions of lower temperatures. As a result, the electron temperature derived from the Balmer discontinuity will be lower than that derived from the [O III] forbidden lines. One of the consequences of the presence of large temperature fluctuations in nebulae is that the standard abundance determinations based on CEL analyses may significantly underestimate the heavy-element abundances in those nebulae. A full discussion of temperature fluctuations and their effects on abundance determinations will be given in Section 5.

While the ratio of the Balmer discontinuity to a H I recombination line such as H 11 or Hβ measures the plasma electron temperature, the ratios of the high-order Balmer lines relative to Hβ, $I(n \rightarrow 2, n \gtrsim 10)$, are sensitive to N_e and thus provide a valuable density diagnostic. This diagnostic is insensitive to the adopted T_e and can be used to probe ionized high-density material ($N_e \gtrsim 10^6\,\mathrm{cm^{-3}}$). With our spectral resolution, the Balmer decrement can be measured up to $n = 24$. The intensities derived from the long-slit spectrum taken along the nebular major axis are plotted in Fig. 10 as a function of n for $10 \leq n \leq 24$. Given the crowding of the high-order Balmer lines, there are no line-free spectral windows from the Balmer discontinuity at 3646 Å up to 3740 Å. The continuum level over this spectral range was therefore estimated by linear extrapolation from longer wavelengths (Fig. 8).

Given the short wavelength range involved and the flatness of the continuum,[3] the continuum level thus derived should be secure and the resultant Balmer line intensities should be accurate to within a few per cent. However, as discussed earlier, the He I recombination spectrum has a small discontinuity at 3678 Å, which affects the continuum level under the last three Balmer lines of interest here, i.e., H 22 at 3676.36 Å, H 23 at 3673.74 Å and H 24 at 3671.48 Å. To account for this, the magnitude of the He I continuum jump was calculated using the H I Balmer discontinuity temperature of 6080 K and the He^+/H^+ abundance of 0.123 (Table 9), and added to the adopted fit of local continuum level extrapolated linearly from longer wavelengths. After the correction, the derived intensities of H 22 to H 24 decrease by approximately 10 per cent compared to those before the correction.

Fig. 10 shows that except for H 14, H 15 and H 16, which are affected by line blending, the measured intensities of all other Balmer lines from $n = 10$ to 24, as a function of n, fall on a smooth curve, and a resultant least-squares optimization with all data points given equal weight (but excluding H 14 to H 16) yields a best-fitting density of $2000^{+2000}_{-1000}\,\mathrm{cm}^{-3}$ for $T_e = 6000$ K, or $3000^{+5000}_{-2000}\,\mathrm{cm}^{-3}$ for $T_e = 10\,000$ K. The use of a different extinction to the adopted value of $c(\mathrm{H}\beta) = 1.30$ only increases the residuals of the fit. Given that the ionized region of a gaseous nebula is defined by the ionized hydrogen, the observed intensities of higher order Balmer lines from NGC 6153 clearly show that there is no evidence of a significant amount of material in condensations with densities of the order of $10^6\,\mathrm{cm}^{-3}$. The implication of this key result will be further discussed in Section 5.4.

3.3 Recombination excitation of the N II and O II auroral lines

In Table 6 the temperatures derived from the [N II] (λ6548 + λ6584)/λ5754 ratio, and in particular those deduced from the [O II] (λ7320 + λ7330)/λ3727 ratio, are significantly higher than those derived from the [O III] nebular to auroral line ratio. We will show below that the abnormally high [N II] and [O II] temperatures are caused by contamination of the [N II] and [O II] auroral lines by recombination excitation.

In NGC 6153, nearly all N and O atoms are in their doubly ionized stages (cf. Sections 3.4 and 3.5). As discussed by Rubin (1986), recombination of N^{2+} and O^{2+} can be important in exciting the weak [N II] auroral λ5754 line and the [O II] auroral and nebular $\lambda\lambda$7320, 7330, $\lambda\lambda$3726, 3729 lines, leading to apparent high electron temperatures from the (λ6548 + λ6584)/λ5754 and (λ7320 + λ7330)/λ3727 ratios. From the radiative recombination coefficients for the metastable levels of [N II] calculated by Péquignot et al. (1991) and the dielectronic recombination coefficients given by Nussbaumer & Storey (1984), we find that the intensity of the λ5754 line due to recombination excitation can be fitted by

$$\frac{I_R(\lambda5754)}{I(\mathrm{H}\beta)} = 3.19t^{0.30} \times \frac{N^{2+}}{H^+}, \qquad (1)$$

where $t \equiv T_e/10^4$ K and $0.5 \le t \le 2.0$.

[3] The continuum emission in this wavelength range consists of the Paschen continuum and the two-photon emission from the nebula (cf. Brown & Mathews 1970), as well as some contribution from the central star. The Paschen continuum decreases towards short wavelengths as λ^3. This decrease is partly compensated by an increasing contribution from the two-photon emission and stellar continuum, yielding a fairly flat nebular continuum level.

In Appendix A we describe the results of a new calculation of the recombination coefficients of the O^+ metastable levels $^2P^o$ and $^2D^o$ of the ground configuration $2p^3$. The new coefficients, together with the transition probabilities of Zeippen (1982), have been used to calculate the predicted intensity of the [O II] $\lambda\lambda$7320, 7330 auroral lines due to recombination excitation. The result can be fitted in the range $0.5 \le t \le 1.0$ by

$$\frac{I_R(\lambda7320 + \lambda7330)}{I(\mathrm{H}\beta)} = 9.36t^{0.44} \times \frac{O^{2+}}{H^+}. \qquad (2)$$

For NGC 6153, the observed [N III] 57-μm line flux yields $N^{2+}/H^+ = 1.92 \times 10^{-4}$ for $N_e = 1660\,\mathrm{cm}^{-3}$ (Table 8). Thus from equation (1) we have $I_R(\lambda5754)/I(\mathrm{H}\beta) = 0.000\,595$, about 7 per cent of the observed intensity of the λ5754 line relative to Hβ, $I(\lambda5754)/I(\mathrm{H}\beta) = 0.008\,25$. After subtracting $I_R(\lambda5754)$ from the observed flux, the [N II] (λ6548 + λ6584)/λ5754 ratio yields $T_e = 9910$ K, 310 K lower than the value deduced before the correction (cf. Table 6). For $N_e = 3500\,\mathrm{cm}^{-3}$, the 57-$\mu$m line yields $N^{2+}/H^+ = 3.56 \times 10^{-4}$ and thus $I_R(\lambda5754)/I(\mathrm{H}\beta) = 0.001\,10$, leading to a corrected [N II] temperature of 9640 K, i.e., 590 K lower. As we will show later (Section 3.5.3), the N^{2+}/H^+ ionic abundance derived from N II recombination lines is 5 times higher, $N^{2+}/H^+ = 17.2 \times 10^{-4}$, yielding a predicted contribution of $I_R(\lambda5754)/I(\mathrm{H}\beta) = 0.005\,33$, about 64 per cent of the observed value. After correcting for this $I_R(\lambda5754)$, the [N II] nebular to auroral line ratio yields a temperature of only 7110 K, which is in better agreement with the Balmer jump temperature of 6080 K than with the value of 9110 K given by the [O III] nebular to auroral line ratio.

For pure recombination excitation, the [N II] nebular $\lambda\lambda$6548, 6584 lines and the auroral λ5754 line have intensity ratios of $I_R(\lambda\lambda6548, 6584)/I_R(\lambda5754) = 5.6$, 5.9 and 6.3 for $T_e = 5000$, 10 000 and 15 000 K respectively. The actual observed nebular to auroral line ratio is about 13 times larger; thus the effects of recombination excitation on the [N II] nebular lines are small and amount to only 10 per cent even for the high N^{2+}/H^+ abundance ratio derived from N II recombination lines (Section 3.5.3).

For O^{2+}/H^+, the [O III] 52, 88-μm lines measured by the *ISO* LWS yield an abundance of 5.61×10^{-4}, in close agreement with the value derived from the $\lambda\lambda$4959, 5007 lines (Table 8). For such an O^{2+}/H^+ abundance, equation (2) then predicts a recombination intensity relative to Hβ of 0.0050 for the [O II] $\lambda\lambda$7320, 7330 lines, or 15 per cent of the value of 0.032 95 from the scanned observations. For $O^{2+}/H^+ = 5.61 \times 10^{-4}$, recombination excitation will contribute about 15 per cent of the observed intensity of the $\lambda\lambda$3726, 3729 lines. After correcting for the recombination excitation contribution to both the $\lambda\lambda$7320, 7330 lines and the $\lambda\lambda$3726, 3729 lines, the [O II] nebular to auroral line ratio yields a temperature of $T_e = 17\,350$ K, nearly the same as 17 910 K deduced before the corrections.

However, if $O^{2+}/H^+ = 40 \times 10^{-4}$, as derived from the O II recombination lines (cf. Tables 14 and 15), then $I_R(\lambda7320 + \lambda7330)/I(\mathrm{H}\beta) = 0.030$ for $T_e = 6100$ K or 0.036 for $T_e = 9100$ K, identical within the errors with the observed value of 0.033. Similarly, for $\lambda\lambda$3726, 3729, the intensity predicted from recombination excitation alone yields 0.272, very similar to the observed value of 0.265. In fact, for pure recombination excitation, the [O II] nebular $\lambda\lambda$3726, 3729 lines and the auroral $\lambda\lambda$7320, 7330 lines have intensity ratios of $I_R(\lambda\lambda3726, 3729)/I_R(\lambda\lambda7320, 7330) = 7.8$, 7.7 and 7.5 for $T_e = 5000$, 10 000 and 15 000 K respectively, compared to the observed ratio of 8.0. Thus,

if the O^{2+}/H^+ abundance is really as high as that derived from O II recombination lines, then the observed fluxes from both the [O II] nebular and auroral lines are consistent with pure recombination excitation, and therefore their ratio is no longer a useful temperature diagnostic. However, in such a case we can use the ratio of [O III] $\lambda\lambda$4959, 5007 to [O II] $\lambda\lambda$7320, 7330 to derive the temperature, since the former lines are presumably collisionally excited. From this ratio, we find $T_e = 6200$ K, which is in good agreement with the value of 6100 K derived from the nebular continuum Balmer discontinuity, and in reasonable agreement with the value of 7110 K derived from the [N II] nebular to auroral line ratio *after* correcting for the recombination excitation of λ5754, by the amount predicted by the N^{2+}/H^+ abundance ratio deduced from the N II recombination lines.

In standard nebular abundance analyses, the N^+/H^+ and O^+/H^+ abundances are usually derived from intensities of the [N II] nebular $\lambda\lambda$6548, 6584 lines and of the [O II] nebular $\lambda\lambda$3726, 3729 lines respectively, assuming the electron temperature deduced from the [N II] nebular to auroral line ratio (λ6548 + λ6584)/λ5754 for both ions. Because of the recombination excitation of the λ5754 line, which leads to overestimated [N II] temperatures, the N^+/H^+ ratio can be significantly underestimated for some nebulae, in particular for those of relatively high excitation classes where more N is in the doubly ionized stage. The effects of recombination excitation on the O^+/H^+ abundances derived from the $\lambda\lambda$3726, 3729 lines are more complicated. While correcting for recombination excitation of the [N II] λ5754 line will increase the O^+/H^+ abundance derived from the $\lambda\lambda$3726, 3729 lines owing to a lower [N II] temperature, the enhancement is offset or even diminished after correcting for the recombination excitation contribution to the $\lambda\lambda$3726, 3729 lines, which have much larger effective (radiative plus dielectronic) recombination coefficients than the [N II] $\lambda\lambda$6548, 6584 lines. The net effects of recombination excitation on the O^+/H^+ and N^+/O^+ abundance ratios depend on the actual electron temperature and N^{2+}/H^+ and O^{2+}/H^+ abundances.

To summarize, for a low-density uniform nebula, as tacitly assumed above, it is possible to explain the entire fluxes of the [O II] nebular lines $\lambda\lambda$3726, 3729 and of the auroral lines $\lambda\lambda$7320, 7330 observed from NGC 6153 by recombination excitation alone. However, we shall show in Section 5.5 that it is possible to construct two-component nebular models which also reproduce the observed intensities of these lines, incorporating processes of recombination excitation as well as of collisional excitation *and* de-excitation. Similarly, the electron temperature derived from the [N II] nebular to auroral line ratio could well be overestimated, due to recombination excitation of the auroral λ5754 line. Given the large uncertainties of the [N II] temperatures, we have adopted T_e([O III]) when calculating the forbidden-line O^+/H^+ and N^+/H^+ abundances.

For the [O III] auroral λ4363 line, recombination excitation yields an intensity

$$\frac{I_R(\lambda4363)}{I(H\beta)} = 12.4t^{0.59} \times \frac{O^{3+}}{H^+}. \quad (3)$$

The O^{3+}/H^+ abundance ratio in NGC 6153 is not available from either CELs or ORLs. However, it can be estimated from the He ionic abundances using $O^{3+}/H^+ = [(He/He^+)^{2/3} - 1] \times (O^+/H^+ + O^{2+}/H^+) = 0.058 \times (O^+/H^+ + O^{2+}/H^+)$ (cf. Table 9 and Section 3.7). Using the O^+/H^+ and the O^{2+}/H^+ abundances listed in Table 8, derived from CELs, the estimated contribution from recombination to the observed λ4363 flux is found to be less than 1 per cent and thus can be ignored. The correction becomes noticeable if we adopt the O^{2+}/H^+ ratio derived from the O II recombination lines (Table 18). In this case, the contribution amounts to approximately 7 per cent and, after correcting for recombination excitation of the λ4363 line, the [O III] nebular to auroral line ratio would yield a temperature of 8950 K, i.e., about 200 K lower than before the correction. Thus, even if we adopt the high O abundance derived from ORLs, the effect of recombination excitation on T_e([O III]) remains small, if not completely negligible. To maintain consistency for the analysis of CELs, the [O III] temperatures without correction will be adopted in the abundance determinations, as detailed in the following sections.

Among the other optical forbidden lines from singly ionized species, we expect recombination may play a role in exciting the [S II] lines, in particular its transauroral lines at 4048 and 4076 Å. The fluxes of the latter two lines are quite uncertain, as both of them are blended with strong lines from O II multiplet V 1 (Table 2), in particular the λ4076.35 line which is blended with the much stronger O II λ4075.86 line. The [S II] $\lambda4068/(\lambda6716 + \lambda6731)$ ratios deduced from the integrated minor-axis spectrum and from the scanned spectrum for the whole nebula are 0.130 and 0.122 respectively (Table 2), yielding respectively electron temperatures of 7530 and 7220 K for $N_e = 3500\,cm^{-3}$, assuming pure collisional excitation. These temperatures are much lower than those yielded by the [O II] auroral to nebular line ratios, and even lower than those yielded by the [N II] and [O III] nebular to auroral line ratios. Lowering the electron density will, however, dramatically increase the resultant temperatures derived from the $\lambda4068/(\lambda6716 + \lambda6731)$ ratio. For $N_e = 2000\,cm^{-3}$, the observed ratios yield $T_e = 9810$ and 9270 K respectively for the minor axis and the whole nebula. A more sophisticated analysis is, however, hindered by the lack of the effective recombination coefficients for the [S II] metastable levels.

3.4 Ionic abundances from CELs

The ionic abundances derived from UV, optical and infrared CELs are given in Table 8. A constant temperature of 9100 K and a density of $3500\,cm^{-3}$ have been assumed, except for the N^{2+}/H^+ ratio derived from the [N III] 57-μm line and the O^{2+}/H^+ ratio derived from the [O III] 52, 88-μm lines, for which we have adopted the abundances deduced for $N_e = 1660\,cm^{-3}$, the density given by the observed [O III] 88 μm/52 μm line ratio. For $N_e = 3500\,cm^{-3}$, the N^{2+}/H^+ and O^{2+}/H^+ ratios derived from these far-IR fine-structure lines are respectively factors of 1.8 and 1.7 higher. The critical densities of the other IR fine-structure lines in Table 8 are sufficiently large that the abundances derived from them are essentially the same whichever density is adopted. Since recombination can be important in exciting the [O II] $\lambda\lambda$3726, 3729 doublet (cf. Section 3.3), the O^+/H^+ abundances deduced from it should be treated as upper limits.

The [Ne IV] $\lambda\lambda$4724, 4726 lines were only marginally detected on the high-resolution minor-axis spectrum. The observed flux yields $Ne^{3+}/H^+ = 9.6 \times 10^{-5}$. Because of the very high excitation energy, E_{ex}, of the auroral $\lambda\lambda$4724, 4726 lines, the abundance ratio derived from them is very sensitive to the adopted T_e, and seems much too high considering the small ionic concentration of He^{2+} in NGC 6153 and the fact that Ne^{2+} has an ionization potential higher than He^+. It is possible that the $\lambda\lambda$4724, 4726 lines are contaminated by other weak lines. Given these uncertainties, the Ne^{3+}/H^+ deduced from the $\lambda\lambda$4724, 4726

Table 8. Ionic abundances from collisionally excited lines[a].

Lines	X^{i+}/H^+	Minor axis	Entire nebula
C III] λ1908	C^{2+}/H^+		2.50(−4)
[N II] λλ6548,6584	N^+/H^+	1.24(−5)	1.09(−5)
N III] λ1751	N^{2+}/H^+		5.20(−4)
[N III] 57 μm	N^{2+}/H^+		1.92(−4)[b]
[O II] λλ3726,3729	O^+/H^+	≤2.62(−5)[c]	≤2.32(−5)[c]
[O III] λλ4959,5007	O^{2+}/H^+	4.33(−4)	4.45(−4)
[O III] 52, 88 μm	O^{2+}/H^+		5.61(−4)[d]
[Ne II] 12.8 μm	Ne^+/H^+		3.36(−5)[e]
[Ne III] λλ3868,3967	Ne^{2+}/H^+	1.44(−4)	1.40(−4)
[Ne III] 15.5 μm	Ne^{2+}/H^+		1.74(−4)[f]
[S II] λλ6716,6731	S^+/H^+	4.57(−7)	3.92(−7)
[S III] λλ6312	S^{2+}/H^+	4.62(−6)	4.48(−6)
[S III] 18.7 μm	S^{2+}/H^+		6.06(−6)[g]
[S IV] 10.5 μm	S^{3+}/H^+		9.56(−6)[h]
[Cl III] λλ5517,5537	Cl^{2+}/H^+	1.13(−7)	1.14(−7)
[Ar III] λλ7135	Ar^{2+}/H^+	1.78(−6)	1.98(−6)
[Ar III] 9.0 μm	Ar^{2+}/H^+		5.62(−6)[i]
[Ar IV] λλ4711,4740	Ar^{3+}/H^+	6.15(−7)	6.00(−7)

[a] Assuming $T_e = 9100$ K and $N_e = 3500\,cm^{-3}$ unless otherwise specified. The numbers in parentheses are power of 10;
[b] For $N_e = 1660\,cm^{-3}$. $N^{2+}/H^+ = 3.56(-4)$ if $N_e = 3500\,cm^{-3}$;
[c] Upper limit due to possible recombination excitation of the [O II] λλ3726, 3729 doublet (cf. Section 3.3);
[d] For $N_e = 1660\,cm^{-3}$. $O^{2+}/H^+ = 9.55(-4)$ if $N_e = 3500\,cm^{-3}$;
[e] $Ne^+/H^+ = 3.34(-5)$ for $N_e = 1660\,cm^{-3}$;
[f] $Ne^{2+}/H^+ = 1.70(-4)$ for $N_e = 1660\,cm^{-3}$;
[g] $S^{2+}/H^+ = 5.35(-6)$ for $N_e = 1660\,cm^{-3}$;
[h] $S^{3+}/H^+ = 8.60(-6)$ for $N_e = 1660\,cm^{-3}$;
[i] $Ar^{2+}/H^+ = 5.52(-6)$ for $N_e = 1660\,cm^{-3}$.

lines is not listed in Table 8 and will be discarded in our abundance analysis.

The C IV λλ1548, 1550 resonance lines and the O III] λλ1661, 1666 lines have not been detected by the *IUE*. For $T_e = 9100$ K, their flux upper limits (Table 5) yield respectively abundance ratios of $C^{3+}/H^+ \lesssim 2\times10^{-4}$ and $O^{2+}/H^+ \lesssim 2\times10^{-3}$.

3.5 Ionic abundances from ORLs

In the following subsections we present He, C, N, O and Ne ionic abundances derived from ORLs. Such ionic abundances depend only weakly on the adopted temperature, $X^{i+}/H^+ \sim T_e^{\alpha}$, where $|\alpha| < 1$, and are essentially independent of N_e. A constant temperature of $T_e = 9100$ K and a density of $N_e = 3500\,cm^{-3}$ were assumed throughout.

3.5.1 He^+/H^+ and He^{2+}/H^+

The ionic and total He abundances derived from He I and He II recombination lines are given in Table 9. The He^+/H^+ abundances derived from the λλ4471, 5876 and 6678 lines were averaged with weights of 1:3:1, roughly proportional to the intrinsic intensity ratios of the three lines. Case A recombination was assumed for the triplet lines λ4471 and λ5876, and case B for the singlet λ6678 line. The effective recombination coefficients were from Brocklehurst (1972). For the λ4471 line, the effective coefficient given by Brocklehurst differs by only 1.5 per cent from the recent calculations of Smits (1996). The differences between the two calculations are even smaller for the other two He I lines. Contributions to the observed fluxes by collisional excitation from the He^0 $2s\,^3S$ metastable level by electron impacts were corrected for using the formulae derived by Kingdon & Ferland (1995a),

Table 9. He abundances.

He^{i+}/H^+	Line	Minor axis	Entire nebula
He^+/H^+	He I λ4471	0.123	0.128
He^+/H^+	He I λ5876	0.127	0.128
He^+/H^+	He I λ6678	0.112	0.118
He^+/H^+	Mean	0.123	0.126
He^{2+}/H^+	He II λ4686	0.011	0.010
He/H		0.134	0.137

which are based on new collision strengths of Sawey & Berrington (1993) from a 29-state quantal calculation of He I extending to $n = 5$. For the adopted T_e and N_e, the corrections amount to 2.4, 6.2 and 2.9 per cent for the λλ4471, 5876 and 6678 lines respectively. The λ6678 line is blended with the He II line $n =$ 5–13 λ6683.20. The contribution from the latter line to the observed flux was corrected for using the He II λ4686 line. The corrections amount to 2.0 and 1.7 per cent for the minor-axis and scanned spectra respectively.

The He^{2+}/H^+ abundance ratio was calculated from the He II λ4686 line only, using the effective recombination coefficients of Storey & Hummer (1995). The elemental He abundance relative to H is given by $He/H = He^+/H^+ + He^{2+}/H^+$, and equals 0.134 and 0.137 for the minor-axis and scanned spectra respectively.

While the He^+/H^+ abundances derived from the two triplet lines λ4471 and λ5876 agree remarkably well (Table 9), the values deduced from the singlet λ6678 line are systematically lower by 8–10 per cent for both data sets. Since the intensity of the λ6678 line relative to λ4471 increases with decreasing temperature, lowering the temperature from the current value of 9100 K to 6100 K as deduced from the Balmer jump would only increase the discrepancy – from 8 to 12 per cent in the case of scanned data. Such a large discrepancy is hard to explain by errors in the reddening correction, given the excellent agreement between the λ4471 and λ5876 lines and the fact that in order to reconcile the He^+/H^+ abundances derived from the λ5876 and λ6678 lines, a reddening constant of $c(H\beta) = 0.99$ is required, instead of the adopted value of $c(H\beta) = 1.30$ derived from the observed Balmer decrement. Such a large error in the reddening correction seems unlikely. For the adopted T_e and N_e, the collisional excitation correction for the λ6678 line is very similar to that of the λ4471 line, amounting to only 2–3 per cent; thus the discrepancy is also difficult to explain in terms of errors in the collision excitation corrections. The possibility that the discrepancy may be due to some unfavourable combination of various sources of systematic errors, such as the collisional excitation correction, the relative flux calibration and the reddening correction, is however difficult to rule out.

Several He I recombination line series have been observed in our spectra. The reddening-corrected observed intensities relative to the λ4471 line are compared to the theoretical predictions of Brocklehurst (1972) and Smits (1996) in Table 10. The intensities are normalized to $I_r(\lambda4471) = 1.00$, the intensity of the λ4471 line after collisional excitation correction. For $T_e = 9100$ K and $N_e = 3500\,cm^{-3}$, $I_r(\lambda4471) = I(\lambda4471)/1.0245$, where $I(\lambda4471)$ is the observed (total) intensity of the λ4471 line (Kingdon & Ferland 1995a). Note that the collisional excitation correction has not been made for other lines in Table 10. Given the relatively low T_e and N_e of NGC 6153, the corrections are only of any significance for lines arising from the $n = 3$ upper levels, and should be completely negligible for lines from higher states. Table 10 shows excellent agreement between the observations and

Table 10. He I lines detected from NGC 6153. The intensities have been corrected for extinction and are normalized such that I_r(He I λ4471) = 1.00, the observed intensity of the He I λ4471 line after correction for collisional excitation. Collisional excitation of other lines has not been corrected for. The results are compared to the theoretical values deduced from Brocklehurst (1972) and Smits (1996).

λ_0	n	I_{obs} Minor axis	I_{obs} Entire nebula	I_{pred} B72	I_{pred} S96
		$2s\,^1S - np\,^1P^o$ series			
3447.59	6	.021	*	.063	
3613.64	5	.058	*	.111	
		$2p\,^1P^o - ns\,^1S$ series			
4437.55	5	.011	.0092	.016	
5047.74	4	.025	.0166	.038	
7281.35	3	.094	.089	.133	.138
		$2p\,^1P^o - nd\,^1D$ series			
3805.74	11	.015	*	.011	
3926.54	8	.023	*	.028	
4009.26	7	.042	.058	.043	
4143.76	6	.069	.078	.070	
4387.93	5	.108	.116	.127	.122
4921.93	4	.267	.256	.274	.266
6678.16[a]	3	.757	.764	.804	.786
		$2s\,^3S - np\,^3P^o$ series			
3187.74	4	.558	*	.886	.884
3888.65	3	1.75	1.88	2.20	2.16
		$2p\,^3P^o - ns\,^3S$ series			
4120.84	5	.028	.009	.036	
4713.17	4	.112	.110	.087	.098
7065.25	3	.714	.688	.313	.442
		$2p\,^3P^o - nd\,^3D$ series			
3465.94	17	.013	*	.011	
3471.83	16	.014	*	.013	
3478.97	15	.020	*	.016	
3487.73	14	.014	*	.020	
3498.66	13	.026	*	.024	
3512.52	12	.030	*	.031	
3530.50	11	.036	*	.040	
3554.42	10	.048	*	.054	
3587.28	9	.063	*	.074	
3634.25	8	.092	*	.107	
3705.02	7	.072	*	.161	
3819.62	6	.253	*	.262	
4026.21	5	.509	.502	.471	.463
4471.50	4	1.02	1.02	1.00	1.00
5875.66	3	3.06	2.98	2.81	2.76

[a] Corrected for the contribution from He II λ6683.20.

recombination theory for the $2p\,^3P^o$–$nd\,^3D$ and $2p\,^1P^o$–$nd\,^1D$ series.[4] The $2s\,^3S$–$np\,^3P^o$ series is clearly affected by self-absorption, which leads to the enhancement of the $2p\,^3P^o$–$ns\,^3S$ series, in particular the λ7065 line. Table 10 however also shows significant departures of the observations from theory: the observed intensities of the $2s\,^1S$–$np\,^1P^o$ series relative to λ4471 are a factor of 2–3 lower, while those of the $2p\,^1P^o$–$ns\,^1S$ series

[4] The weakness of the He I λ3705.02 line, which is blended with H 16, is probably caused by poor line profile fitting. The intensity of H 16 derived from the fitting seems too strong compared to other lines of the Balmer series (cf. Fig. 10).

Table 11. Recombination line C^{2+}/H^+ abundances.

λ_0 (Å)	Mult	Minor axis I_{obs}	Minor axis $\frac{C^{2+}}{H^+}$ (10^{-3})	Entire nebula I_{obs}	Entire nebula $\frac{C^{2+}}{H^+}$ (10^{-3})
7231.32	V3	0.378	0.90	0.356	0.85
7236.42,7.17[a]	V3	.825	0.99	0.723	0.86
V 3 $3p\,^2P^o$–$3d\,^2D$		**1.20**	**0.96**	**1.08**	**0.86**
3918.98	V4	0.048	2.65	*	*
3920.69	V4	0.060	1.66	*	*
V 4 $3p\,^2P^o$–$4s\,^2S$		**.108**	**1.99**		
V 5 $3d\,^2D$–$4p\,^2P^o$ λ5890		**.049**	**1.25**	*	*
V 6 $3d\,^2D$–$4f\,^2F^o$ λ4267		**2.51**	**2.35**	**2.40**	**2.25**

[a] Corrected for a contribution (5 per cent) from [Ar IV] λ7237.16, assuming [Ar IV] $I(\lambda7237.16)/I(\lambda7170.62) = 0.75$.

are systematically lower by 40 per cent. As in the case of the triplet series $2s\,^3S$–$np\,^3P^o$, the $2s\,^1S$–$np\,^1P^o$ series can be suppressed by effects of self-absorption from the metastable $2s\,^1S$ state. However, such effects will also lead to enhanced intensities of the $2p\,^1P^o$–$ns\,^1S$, just as the $2p\,^3P^o$–$ns\,^3S$ series in the case of triplet states. This is in contradiction to what is observed. High-quality measurements of He I recombination lines, in particular the relatively weak singlet series $2s\,^1S$–$np\,^1P^o$ and $2p\,^1P^o$–$ns\,^1S$ in other nebulae, may help clarify the situations.

3.5.2 C^{2+}/H^+

The C^{2+}/H^+ abundance ratios derived from the C II 3–3 transitions and from the 3d–4f λ4267 line are presented in Table 11. They were derived using the recent calculations of Davey et al. (1999) of the case B effective recombination coefficients, which include both radiative and dielectronic recombination processes. Radiative recombination coefficients for multiplets V 3 and V 6 are also available from Péquignot et al. (1991). For V 3, C^{2+}/H^+ abundances derived using recombination coefficients from the latter source are about 7 per cent higher than those given in Table 11, and are only one percent higher for V 6. The effective recombination coefficient for multiplet V 3 is extremely case-sensitive: case A yields C^{2+}/H^+ abundances 20 times higher than case B. Comparison of case B C^{2+}/H^+ abundances with those deduced from multiplet V 6, which are case-insensitive, suggests that case B should be a good approximation, although there could be some small departure from it. Multiplets V 4 and V 5 have a much more moderate dependence on case A or B: the case A effective recombination coefficients are a factor 2–3 lower than case B values. Again, comparison of results from multiplets V 4 and V 6 suggests that case B is a better approximation for multiplet V 4. The multiplet V 5 λ5890 line is only marginally detected, and its flux could be uncertain by a factor of 2.

An important result from our deep optical spectroscopic observations is the detection of C II recombination lines from states higher than the $4f\,^2F^o$ level. The observed intensities of these high E_{ex} lines relative to the 3d–4f λ4267 line are compared in Table 12 to the predictions of recombination theory (Davey et. al. 1999). In all cases, the agreement between the observations and theory is remarkable. The 3d–4f λ4267 line is mainly fed by $4f\,^2F^o$–$ng\,^2G$ transitions, with $4f\,^2F^o$–$5g\,^2G$ λ9903 contributing about half the photons. The λ9903 line unfortunately falls outside our spectral coverage. Nevertheless, the $4f\,^2F^o$–$6g\,^2G$ λ6462 and

Table 12. High-excitation C II recombination lines.

λ_0 (Å)	Transition	Minor axis I_{obs}	Entire nebula I_{obs}	I_{pred}
4267.15	3d–4f	1.000	1.000	1.000
6258.78	4p–5d	0.014	0.014	0.012
6151.43	4d–6f	0.040	0.032	0.040
6461.95	4f–6g	0.096	0.103	0.103
5342.38	4f–7g	0.046	0.041	0.053
4802.23	4f–8g	≤0.02	≤0.02	0.031
4491.07	4f–9g	≤0.01	≤0.03	0.020
4292.16	4f–10g	≤0.01	≤0.02	*

the 4f ^{2}F^o–7g ^{2}G λ5342 lines are clearly detected, with intensities relative to the λ4267 line which are in excellent agreement with the predictions of recombination theory. This result strongly suggests that there is no unknown process other than recombination selectively populating the 4f ^{2}F^o level that might lead to overestimated λ4267 line C^{2+}/H^+ abundances. The latter are often found to be significantly higher than derived from the collisionally excited C III] λ1908 line (e.g. Rola & Stasińska 1994, and references therein), as is the case here for NGC 6153 (cf. Tables 8 and 11).

The $n = 8$ λ4802, $n = 9$ λ4491 and $n = 10$ λ4292 lines of the 4f ^{2}F^o–ng ^{2}G series were not detected. The first two are lost in the wings of known O II recombination lines, and the third is blended with N II lines. Since the wavelengths of the three C II lines, as well as those of the blended O II or N II recombination lines, are accurately known, and since the intensities of these O II or N II lines relative to nearby isolated O II or N II recombination lines are also known from recombination theory, it is possible to obtain upper limits on the intensities of these three C II lines using the technique of Gaussian line profile fitting. The flux upper limits thus obtained are also presented in Table 12, and are consistent with theoretical predictions.

Given the high S/N ratio of the λ4267 line (∼50) and the independence of C^{2+}/H^+ abundances derived from it on the assumption of either case A or case B, we shall adopt C^{2+}/H^+ ratios based on this recombination line alone.

3.5.3 N^{2+}/H^+

A number of N II multiplets have been detected, both singlets and triplets. N^{2+}/H^+ ionic abundances derived from them are presented in Table 13. The strongest multiplet is V 3 3s ^{3}P^o–3p ^{3}D and its effective recombination coefficient is fairly insensitive to the assumption of case A or B: the case B value is only 20 per cent higher than for case A. The two singlets, multiplets V 8 and V 12, are also case-insensitive, as are all the 3d–4f transitions. Most of these lines are, however, quite weak, with large flux uncertainties, except for a few such as the λ4041.31 line, the strongest among the 3d–4f transitions. Except for V 3, the other three 3–3 triplet transitions, V 5, V 20 and V 28, are all extremely case-sensitive. Comparison of N^{2+}/H^+ abundances derived from them for case B, as assumed here, with those derived from other case-insensitive transitions suggests that case B should be a good approximation for the triplets, although there is also some evidence of departure from it, especially for multiplet V 28.

All the N^{2+}/H^+ abundances were derived using effective recombination coefficients from Escalante & Victor (1990), assuming case A for singlets and case B for triplets. For those

Table 13. Recombination line N^{2+}/H^+ abundances.

λ_0 (Å)	Mult	Minor axis I_{obs}	Minor axis $\frac{N^{2+}}{H^+}$ (10^{-3})	Entire nebula I_{obs}	Entire nebula $\frac{N^{2+}}{H^+}$ (10^{-3})
5666.63	V3	.236	1.80	.220	1.68
5676.02	V3	.119	2.05	.126	2.17
5679.56	V3	.536	2.20	.434	1.78
5686.21	V3	.086	1.98	.091	2.09
5710.77	V3	.097	3.36	.057	1.97
V 3 3s ^{3}P^o–3p ^{3}D		**1.08**	**1.98**	**.933**	**1.84**
4601.48	V5	.054	1.34	.080	1.98
4607.16	V5	.073	2.26	.039	1.21
4613.87[a]	V5	.000	0.00	.065	0.95
4621.39	V5	.059	1.83	.043	1.34
4630.54	V5	.199	1.65	.214	1.78
4643.08[b]	V5	.122	3.04	.144	3.59
V 5 3s ^{3}P^o–3p ^{3}P		**.494**	**1.71**	**.483**	**1.67**
V 8 3s ^{1}P^o–3p ^{1}P λ6482		**.045**	**2.44**	**.037**	**2.01**
V12 3s ^{1}P^o–3p ^{1}D λ3995		**.087**	**1.24**		
4788.13	V20	.050	1.33	.049	1.30
4803.29	V20	.117	1.74	.101	1.50
V 20 3p ^{3}D–3d ^{3}D^o		**.256**	**1.55**	**.232**	**1.39**
5927.81	V28	.033	1.33	.053	2.13
5931.78[c]	V28	.036	0.64	.041	0.73
5940.24,1.65	V28	.034	1.83	*	*
5941.65	V28	.092	0.88	.089	0.86
5952.39[d]	V28	.014	0.75	.017	0.92
V 28 3p ^{3}P–3d ^{3}D^o		**.210**	**0.94**	**.232**	**0.98**
		3d–4f transitions			
4035.08[e]	V39a	.110	1.22	.093	1.04
4043.53	V39a	.100	0.85	.154	1.30
4041.31[f]	V39b	.272	1.77	.238	1.54
4176.16	V43a	.075	1.04	.115	1.60
4236.91	V48a	.071	1.63	.075	1.72
4241.24,.78	V48a	.205	2.20	.213	2.28
4237.05	V48b	.105	1.63	.111	1.72
4179.67[g]	V50a	.049	4.83	.024	2.36
4431.82,2.74	V55a	.102	1.83	.099	1.77
4442.02	V55a	.021	0.83	.050	1.97
4433.48	V55b	.021	1.86	.020	1.77
4552.53	V58a	.100	3.92	.057	2.24
4530.41[h]	V58b	.122	1.15	.180	1.70
4678.14	V61b	.053	0.82	.053	0.82
Sum		**1.42**	**1.52**	**1.50**	**1.60**

[a] Corrected (100 and 65 per cent respectively for the minor axis and the whole nebula) for the contributions from O II 3d–4f ^{2}D$_{5/2}$–F[3]$_{5/2}$ λ4613.14 and ^{2}D$_{5/2}$–F[3]$_{7/2}$ λ4613.68 (V 92b) lines, using O II $I(\lambda4613.14 + \lambda4613.68)/I(\lambda4089.29) = 0.078$ (LSBC). Not used to calculate the total intensity of the multiplet;

[b] Affected by nearby strong N III and O II emission, not used in calculating the total intensity of the multiplet;

[c] Corrected for the He II λ5931.84 line (26 and 23 per cent, respectively, for the minor axis and the entire nebula) using He II $I(\lambda5932)/I(\lambda4686) = 9.13 \times 10^{-4}$;

[d] Corrected for the He II λ5952.94 line (50 and 43 per cent, respectively, for the minor axis and the entire nebula), using He II $I(\lambda5953)/I(\lambda4686) = 1.03 \times 10^{-3}$;

[e] Corrected for a 12 per cent contribution from O II 3d ^{4}F$_{5/2}$–4f F[3]$_{5/2}$ λ4035.06 (V 50b), using O II $I(\lambda4035.06)/I(\lambda4089.29) = 0.027$;

[f] Corrected for a 5 per cent contribution from O II 3d–4f ^{4}F$_{5/2}$–F[2]$_{5/2}$ λ4041.29 and ^{4}F$_{5/2}$–F[2]$_{3/2}$ λ4041.95 (V 50c), using O II $I(\lambda4041.29 + \lambda4041.95)/I(\lambda4089.29) = 0.024$;

[g] Includes 11 per cent contribution from N II 3d ^{3}D$_3$–4f 2[3]$_2$ λ4178.86 (V 50a);

[h] Corrected for a 2 per cent contribution from N III λ4530.86, using N III $I(\lambda4530.86)/I(\lambda4514.86) = 0.042$.

whose effective recombination coefficients are also available from Péquignot et al. (1991), the differences between the two atomic data sets are generally insignificant. For the 3d–4f transitions, apart from N^{2+}/H^+ abundances derived from individual transitions, we also present in Table 13 the abundances derived after co-adding the fluxes of all detected 3d–4f lines, 1.52 and 1.60×10^{-3} for the minor axis and the entire nebula respectively. For comparison, the mean ionic abundances obtained by averaging the values derived from individual 3d–4f lines, giving equal weight, are (1.85 ± 0.30) and $(1.73 \pm 0.12) \times 10^{-3}$ for the minor axis and the entire nebula respectively, where the uncertainties are 1σ standard errors. The abundances derived from the total intensities of all the 3d–4f transitions are preferred over the average values of abundances from individual lines, since strong lines are better detected with smaller (relative) flux uncertainties.

We finally adopt the recombination line N^{2+}/H^+ abundance ratios by averaging the results from multiplet V 3 and from the total flux of all detected 3d–4f transitions. This yields $N^{2+}/H^+ = 1.75$ and 1.72×10^{-3} for the minor axis and for the entire nebula respectively.

3.5.4 O^{2+}/H^+

NGC 6153 presents the best O II recombination-line spectrum that has been observed so far from an ionized nebula. More lines are detected, and the line strengths relative to Hβ are even stronger, than for the PN NGC 7009 previously studied by LSBC. O^{2+}/H^+ ionic abundance ratios are presented in Table 14 for 3s–3p and 3p–3d transitions and in Table 15 for 3d–4f transitions. Effective recombination coefficients are from Storey (1994) for 3s–3p transitions (*LS*-coupling) and from LSBC for 3p–3d and 3d–4f transitions (intermediate coupling), assuming case A for doublets and case B for quartets. All multiplets except V 11, V 19 and V 28, are fairly case-insensitive. Comparison of case B abundances derived from these three multiplets with other case-insensitive multiplets suggests that case B is a good approximation for the quartets. Similarly, the doublets follow case A rather than case C. As in the case of the N II lines, for the O II 3d–4f transitions we adopt abundances derived after co-adding the intensities of all detected lines, yielding $O^{2+}/H^+ = 5.40$ and 4.92×10^{-3} for the minor axis and for the whole nebula. The mean ionic abundances obtained from averaging the values derived from individual 3d–4f lines, giving equal weight, are (5.75 ± 0.22) and $(5.11 \pm 0.36) \times 10^{-3}$ for the minor axis and for the whole nebula respectively.

O^{2+}/H^+ ionic abundances derived from individual 3d–4f transitions agree very well and are consistent with those derived from the 3p–3d multiplets. Of the three detected 3s–3p multiplets, for which only *LS*-coupling effective recombination coefficients are available, the O^{2+}/H^+ abundances derived from the ^2P–$^2D^o$ (V 5) doublet agree quite well with the values from 3p–3d and 3d–4f transitions. On the other hand, the abundances from the quartet–quartet transitions, multiplets V 1 and V 2, are significantly lower, by about 40 per cent and a factor of 2 respectively. Similar discrepancies were found for NGC 7009 by LSBC and were interpreted as probably caused by the breakdown of *LS*-coupling among the (^{3}P)*n*d states, which allows them to bypass the (^{3}P)*n*p term and decay directly to the ground configurations, which is not permitted in pure *LS*-coupling. The abnormally low values derived from V 2 could also be partly caused by departure from case B. For case A, the abundances derived from this multiplet would be a factor of 1.4 higher. However, the effective recombination coefficients for case A and B for multiplet V 1 differ by only 4 per cent.

For both NGC 7009 and NGC 6153, the observed λ4156.53 line of multiplet V 19 is too strong compared to other components of

Table 14. O^{2+}/H^+ abundances from 3–3 recombination lines.

λ_0 (Å)	Mult	Minor axis I_{obs}	Minor axis $\frac{O^{2+}}{H^+}$ (10^{-3})	Entire nebula I_{obs}	Entire nebula $\frac{O^{2+}}{H^+}$ (10^{-3})
4696.35	V1	0.037	3.00	0.062	5.02
4676.24	V1	0.348	3.12	0.300	2.69
4673.73	V1	0.091	4.42	0.081	3.93
4661.63	V1	0.439	3.30	0.431	3.24
4650.84	V1	0.352	3.39	0.332	3.19
4649.13	V1	1.486	2.98	1.374	2.76
4641.81[a]	V1	0.875	3.34	0.863	3.29
4638.86[a]	V1	0.624	6.00	0.536	5.16
V 1 3s ^{4}P–3p ^{4}D^o		**3.899**	**3.13**	**3.654**	**2.93**
4366.89	V2	0.227	2.82	0.217	2.69
4349.43	V2	0.387	2.05	0.413	2.18
4345.56[b]	V2	0.237	3.16	0.255	3.40
4325.76	V2	0.028	1.85	0.079	5.23
4319.63	V2	0.136	1.67	0.159	1.95
4317.14	V2	0.201	2.66	0.130	1.72
V 2 3s ^{4}P–3p ^{4}P^o		**1.272**	**2.35**	**1.311**	**2.42**
4452.37	V5	0.043	7.63	0.063	11.2
4416.97	V5	0.140	4.94	0.171	6.04
4414.90	V5	0.184	3.60	0.184	3.60
V 5 3s ^{2}P–3p ^{2}D^o		**0.367**	**4.32**	**0.418**	**4.92**
4092.93	V10	0.131	3.99	0.184	5.60
4085.11	V10	0.190	4.22	0.213	4.74
4078.84	V10	0.175	4.77	0.174	4.75
4075.86	V10	1.279	3.68	1.138	3.27
4072.16	V10	1.047	4.35	1.022	4.25
4069.62,.89	V10	1.358	5.25	1.349	5.22
V 10 3p ^{4}D^o–3d ^{4}F		**4.196**	**4.35**	**4.096**	**4.24**
3907.46	V11	0.036	3.58	*	*
V 11 3p ^{4}D^o–3d ^{4}P		**0.103**	**3.58**		
3882.19,3.13[c]	V12	0.175	4.96	*	*
V 12 3p ^{4}D^o–3d ^{4}D		**0.382**	**4.96**		
4169.22[d]	V19	0.058	2.18	0.097	3.64
4156.53	V19	0.104	8.33	0.120	9.61
4153.30	V19	0.282	3.59	0.289	3.69
4132.80	V19	0.173	3.15	0.111	2.02
4129.32	V19	0.030	4.56	0.027	4.11
4121.46	V19	0.119	4.24	0.147	5.23
V 19 3p ^{4}P^o–3d ^{4}P		**0.770**	**3.70**	**0.796**	**3.82**
4119.22,20.28,.54	V20	0.492	4.24	0.609	5.25
4110.78	V20	0.073	3.02	0.099	4.10
V 20 3p ^{4}P^o–3d ^{4}D		**0.887**	**4.03**	**1.112**	**5.05**
4705.35	V25	0.040	3.66	0.060	5.50
4699.22	V25	0.047	7.08	0.023	3.47
V 25 3p ^{2}D^o–3d ^{2}F		**0.089**	**4.96**	**0.085**	**4.73**
4924.53	V28	0.183	4.29	0.184	4.32
4906.83	V28	0.095	3.79	0.092	3.67
4890.86	V28	0.036	3.08	0.024	2.05
V 28 3p ^{4}S^o–3d ^{4}P		**0.314**	**3.95**	**0.300**	**3.78**
4943.00	V33	0.039	8.72	0.010	2.23
4941.07	V33	0.010	4.39	0.017	7.47
V 33 3p ^{2}P^o–3d ^{2}D		**0.054**	**7.26**	**0.030**	**4.00**

[a] Affected by nearby strong N III lines; not included when calculating the total intensity of O II multiplet V 1;
[b] Includes a 6 per cent contribution from O II 3d ^{4}D$_{7/2}$–4f G[3]$_{7/2}$ λ4345.55 (V 65c);
[c] Corrected for the contribution from O II λ3882.45 (multiplet V 11), estimated to be $I_{obs} = 0.024$, using the λ3907.46 line of the same multiplet;
[d] The contribution from He I 2p ^{1}P^o–6s ^{1}S λ4168.97 is corrected for using the He I 2p ^{1}P^o–5s ^{1}S λ4437.55 line, assuming $I(\lambda 4168.97)/I(\lambda 4437.55) = 0.52$ (Brocklehurst 1972).

Table 15. O^{2+}/H^+ abundances from 3d–4f recombination lines.

λ_0 (Å)	Mult	Minor axis		Entire nebula	
		I_{obs}	$\frac{O^{2+}}{H^+}$ (10^{-3})	I_{obs}	$\frac{O^{2+}}{H^+}$ (10^{-3})
4089.29	V48a	0.588	5.21	0.541	4.80
4071.23	V48a	0.082	4.27	0.080	4.16
4083.90	V48b	0.215	6.67	0.195	6.05
4087.15[a]	V48c	0.212	6.48	0.195	5.96
4062.94	V50a	0.092	6.42	0.104	7.34
4048.21[b]	V50b	0.063	5.91	*	*
4273–78[c]	V67	0.693	4.84	0.611	4.26
4281–84[d]	V53,67	0.211	5.30	0.226	5.68
4303.82[e]	V53a	0.308	5.64	0.289	5.29
4317.70	V53a	0.022	2.75	0.070	8.74
4307.23	V53b	0.068	5.75	0.046	3.89
4294.78[f]	V53b	0.151	4.68	0.140	4.34
4288.82	V53c	0.053	4.70	0.049	4.35
4291–92[g]	V55,78	0.130	4.52	0.120	4.18
4357.25[h]	V63a	0.035	5.42	0.031	4.81
4334.19[i]	V63b	0.053	8.85	0.002	0.33
4315.40[j]	V63c	0.087	6.92	0.078	6.21
4331.13	V65b	0.069	7.93	0.046	5.29
4332.71	V65b	0.069	6.41	0.103	9.58
4371.62	V76b	0.066	5.93	0.042	3.77
4353.59[k]	V76c	0.053	4.48	0.071	6.00
4313.44[l]	V78a	0.089	5.14	0.054	4.61
4285.69	V78b	0.125	5.84	0.082	3.83
4491.23	V86a	0.095	6.15	0.067	4.34
4466.42[m]	V86b	0.094	8.19	0.106	9.23
4489.49	V86b	0.046	6.24	0.032	4.34
4477.90	V88	0.060	6.19	0.043	4.44
4669.27[n]	V89b	0.024	5.29	0.026	5.73
4609.44	V92a	0.236	4.88	0.307	6.35
4602.13	V92b	0.104	5.40	0.070	3.63
4610.20[o]	V92c	0.094	5.99	0.030	1.91
Sum		**4.287**	**5.40**	**3.856**	**4.92**

[a] Includes a 6 per cent contribution from O II $3d\,^4F_{9/2}$–$4f\,G[5]_{9/2}$ 4088.27 (V 48a);
[b] Includes a 22 per cent contribution from O II $3d\,^4F_{7/2}$–$4f\,F[4]_{9/2}$ λ4046.11 (V 50a) and $3d\,^4F_{7/2}$–$4f\,F[3]_{5/2}$ λ4047.80 (V 50b);
[c] Includes 11 O II 3d–4f transitions;
[d] Includes O II $3d\,^4P_{5/2}$–$4f\,D[2]_{5/2}$ λ4281.32 (V 53b), $3d\,^4P_{5/2}$–$4f\,D[2]_{3/2}$ λ4281.46 (V 53b), $3d\,^2F_{5/2}$–$4f\,F[4]_{7/2}$ λ4282.02 (V 78b), $3d\,^4D_{3/2}$–$4f\,F[2]_{5/2}$ λ4282.96 (V 67c), $3d\,^4D_{5/2}$–$4f\,F[2]_{5/2}$ λ4283.25 (V 67c), $3d\,^4D_{3/2}$–$4f\,F[2]_{3/2}$ λ4283.73 (V 67c), $3d\,^4D_{5/2}$–$4f\,F[2]_{3/2}$ λ4284.00 (V 67c), and $3d\,^4D_{7/2}$–$4f\,F[2]_{5/2}$ λ4284.39 (V 67c);
[e] Includes a 15 per cent contribution from O II $3d\,^4D_{5/2}$–$4f\,G[5]_{9/2}$ λ4303.61 (V 65a) and $3d\,^4P_{5/2}$–$4f\,D[3]_{5/2}$ λ4304.08 (V 53a);
[f] Includes a 19 per cent contribution from O II $3d\,^4P_{3/2}$–$4f\,D[2]_{3/2}$ λ4294.92 (V 53b);
[g] Includes O II $3d\,^4P_{5/2}$–$4f\,G[3]_{7/2}$ λ4291.25 (V 55), $3d\,^4P_{5/2}$–$4f\,G[3]_{5/2}$ λ4291.86 (V 55), $3d\,^2F_{5/2}$–$4f\,F[2]_{5/2}$ λ4292.21 (V 78c) and $3d\,^2F_{5/2}$–$4f\,F[2]_{3/2}$ λ4292.95 (V 78c);
[h] Includes a 13 per cent contribution from O II $3d\,^4D_{3/2}$–$4f\,D[3]_{5/2}$ λ4357.25 (V 63a);
[i] Includes a 30 per cent contribution from O II $3d\,^4D_{3/2}$–$4f\,D[2]_{3/2}$ λ4334.33 (V 63b) and $3d\,^4D_{5/2}$–$4f\,D[2]_{3/2}$ λ4334.03 (V 63b);
[j] Includes a 58 per cent contribution from O II $3d\,^4D_{3/2}$–$4f\,D[1]_{1/2}$ λ4315.39 (V 63c), $3d\,^2F_{7/2}$–$4f\,F[3]_{5/2}$ λ4315.39 (V 78b), $3d\,^4D_{5/2}$–$4f\,D[1]_{3/2}$ λ4315.69 (V 63c) and $3d\,^2F_{7/2}$–$4f\,F[3]_{7/2}$ λ4315.83 (V 78b);
[k] Includes a 3 per cent contribution from O II $3d\,^2F_{5/2}$–$4f\,G[3]_{5/2}$ λ4354.18 (V 76c);
[l] Includes a 34 per cent contribution from O II $3d\,^2F_{7/2}$–$4f\,F[4]_{7/2}$ λ4312.11 (V 78a);
[m] Includes a 10 per cent contribution from O II $3d\,^2P_{3/2}$–$4f\,D[2]_{3/2}$ λ4466.59 (V 86b);
[n] Includes a 45 per cent contribution from O II $3d\,^2D_{3/2}$–$4f\,D[2]_{3/2}$ λ4669.43 (V 89b);
[o] Includes a 25 per cent contribution from O II $3d\,^2D_{3/2}$–$4f\,F[2]_{3/2}$ λ4611.07 (V 92c).

the multiplet. No convincing candidates for lines which might blend with the O II λ4156.53 line, and thus cause the discrepancy, were found by LSBC. We note, however, that in NGC 6153 the intensity ratios of the λ4156.53 ($J = 5/2$–$3/2$) line to the λ4132.80 ($J = 1/2$–$3/2$) line (from the same upper level), 0.6 and 1.1 respectively for the minor axis and for the whole nebula, are about a factor of 2 lower than the values of 1.7 and 2.1 found for the NGC 7009 slit positions of PA = 0° and 45° (LSBC). This intensity ratio depends only on a ratio of transition probabilities, and the fact that it is observed to vary by a factor of 2 does suggest that blending of the λ4156.53 line with some unknown feature is the most likely cause of the discrepancy.

Of the eight observed 3p–3d multiplets, the intensities of those from the upper terms $3d\,^4F$ (V 10) and $3d\,^4D$ (V 12, 20) are almost independent of the assumption of case A or case B. However, multiplets V 11, 19 and 28 from the $3d\,^4P$ upper term, which can decay to the O^+ $2p^3\,^4S^o$ ground state via resonance transitions, are extremely case-sensitive: their case A effective recombination coefficients are more than 20 times smaller than the case B values. For case C to apply to doublets requires transitions to the $2p^3\,^2D^o$ ground state to be optically thick, which is unlikely. Thus the doublets can also be regarded as case-insensitive. It is interesting to note that the O^{2+}/H^+ values derived from the doublets and from the quartets V 10, 12 and 20, all essentially case-insensitive, are systematically higher than those derived from the case-sensitive quartets V 11, 19 and 28. The case-insensitive multiplets V 10, 12, 20, 25 and 33 (excluding V 33 for the minor axis, which gives a value too high compared to those from other multiplets, possibly caused by measurement errors of two very faint and marginally detected lines) yields average O^{2+}/H^+ abundances of (4.6 ± 0.3) and $(4.5 \pm 0.3) \times 10^{-3}$, where the uncertainties are 1σ standard errors, for the minor axis and for the whole nebula respectively. This can be compared to the corresponding average values of (3.7 ± 0.1) and $(3.80 \pm 0.02) \times 10^{-3}$ from multiplets V 11, 19 and 28 (V 19 and 28 only for the whole nebula). It is possible that there is a small departure from the assumed case B towards case A, which would increase the derived abundances for the latter three multiplets, from the $3d\,^4P$ upper term.

The mean O^{2+}/H^+ abundance ratios derived by averaging the values from all 3–3 multiplets (excluding the value from V 33 for the minor axis) plus the co-added 3d–4f transitions (the values in boldface in Tables 14 and 15) are (4.07 ± 0.28) and $(4.08 \pm 0.29) \times 10^{-3}$ for the minor axis and the entire nebula of NGC 6153 respectively. These will be adopted as the recombination line values in our following discussion.

3.5.5 Ne^{2+}/H^+

Several Ne II multiplets have been detected, including about a dozen 3d–4f transitions. Table 16 gives the Ne^{2+}/H^+ abundances ratios derived from these ORLs. For the 3s–3p and 3p–3d transitions the effective recombination coefficients are from recent calculations by Kisielius et al. (1998) assuming *LS*-coupling. Case A is assumed for the quartets V 1, 2 and 13 and case B for the doublet V 20. For the 3d–4f transitions, intermediate coupling effective recombination coefficients (Storey, unpublished) were used. These calculations assumed that the three fine-structure levels of the $2p^4\,^3P_{2,1,0}$ ground terms of Ne^{2+} are thermalized, i.e., with level populations proportional to their statistical weight

Table 16. Recombination line Ne^{2+}/H^+ abundances.

λ_0 (Å)	Mult	Minor axis I_{obs}	Minor axis $\frac{Ne^{2+}}{H^+}$ (10^{-3})	Entire nebula I_{obs}	Entire nebula $\frac{Ne^{2+}}{H^+}$ (10^{-3})
3694.21	V1	0.448	1.36	*	*
3709.62	V1	0.152	1.16	*	*
3777.14	V1	0.044	0.34	*	*
V 1 3s ^{4}P–3p ^{4}P^o		**1.06**	**1.09**		
3334.84	V2	0.731	1.10	*	*
3355.02	V2	0.460	1.31	*	*
V 2 3s ^{4}P–3p ^{4}D^o		**1.95**	**1.17**		
3218.19	V13	0.496	1.20	*	*
V 13 3p ^{4}D^o–3d ^{4}F		**1.39**	**1.20**		
3388.42	V20	0.127	0.57	*	*
V 20 3p ^{2}D^o–3d ^{2}F		**0.318**	**0.57**		
4772.93		0.033	0.52	0.017	0.27
4p ^{4}D^o–5d ^{4}F		**0.135**	**0.52**	**0.069**	**0.27**
3d–4f transitions					
4219.74[a]	V52a	0.117	2.18	0.126	2.35
4233.85	V52a	0.038	2.84	0.045	3.36
4231.64[b]	V52b	0.042	3.31	0.038	2.99
4250.65	V52b	0.044	5.19	*	*
4391.99[c]	V55e	0.138	1.43	0.152	1.57
4409.30	V55e	0.133	2.07	0.124	1.93
4369.86	V56	0.056	*	0.056	*
4397.99	V57b	0.033	0.99	0.045	1.35
4428.64[d]	V60c	0.102	2.41	0.083	1.97
4430.94[e]	V61a	0.059	2.16	0.086	3.15
4457.05[f]	V61d	0.049	5.15	0.051	5.36
4413.22[g]	V65	0.067	2.90	0.058	2.51
Sum[h]		**0.729**	**1.99**	**0.803**	**2.06**

[a] Neglecting Ne II 3d $^4D_{7/2}$–4f 2[4]$_{7/2}$ λ4219.37 (V 52a), which may contribute a few per cent of the observed intensity;
[b] Neglecting Ne II 3d $^4D_{5/2}$–4f 2[3]$_{5/2}$ λ4231.53 (V 52b);
[c] Neglecting Ne II 3d $^4F_{9/2}$–4f 2[5]$_{9/2}$ λ4392.00 (V 55e);
[d] Including the contributions from Ne II 3d $^2D_{5/2}$–4f 2[3]$_{7/2}$ λ4428.52 (V 61b); but neglecting 3d $^2F_{5/2}$–4f 1[3]$_{5/2}$ λ4428.52 (V 60c);
[e] Including Ne II 3d $^4F_{3/2}$–4f 1[2]$_{5/2}$ λ4430.90 (V 57a);
[f] Neglecting Ne II 3d $^2D_{3/2}$–4f 2[2]$_{3/2}$ λ4457.24 (V 61d);
[g] Neglecting Ne II 3d $^4P_{5/2}$–4f 0[3]$_{5/2}$ λ4413.11 (V 65) and 3d $^4F_{3/2}$–4f 1[3]$_{5/2}$ λ4413.11 (V 57c);
[h] Excluding the λ4250.65 and λ4457.05 lines.

$(2J + 1)$. However, the $^3P_1$ and $^3P_0$ levels have quite large critical densities, 2.0×10^5 and $2.9 \times 10^4\,cm^{-3}$. Thus for electron densities lower than these critical densities, the $^3P_1$ and $^3P_0$ levels are underpopulated compared to thermal equilibrium. For $T_e = 9100$ K and $N_e = 3500\,cm^{-3}$, as derived for NGC 6153, the $^3P_{2,1,0}$ levels are populated with ratios 1:0.009:0.009, instead of the LTE values of 1:0.6:0.2. The effects of the non-equilibrium level populations on the effective recombination coefficients adopted here for the 3d–4f transitions are not clear and will vary from line to line. The strongest 3d–4f lines originate from the $^3P_2$ level and the population of this level is underestimated by a factor of about 5/9 if thermal equilibrium is assumed. The recombination coefficients for the strongest lines may therefore be underestimated by this factor, with a corresponding overestimate of the derived Ne^{2+}/H^+ ratio.

The effective recombination coefficient of Ne II multiplet V 20 decreases by only 5 per cent from case A to case B and those for all other lines are essentially case-insensitive. The Ne^{2+}/H^+ ratio of 0.57×10^{-3} derived from multiplet V 20, based on an extremely weak and marginally detected line, is very uncertain and could be in error by a factor of 2 or more. The Ne^{2+}/H^+ abundances derived from the other three 3–3 multiplets, V 1, 2 and 13, are in excellent agreement, with an average value of 1.15×10^{-3}, which is about a factor of 2 lower than those derived from the 3d–4f transitions. The discrepancy could be caused by uncertainties in the effective recombination coefficients for the 3d–4f lines described above. We adopt $Ne^{2+}/H^+ = 1.59 \times 10^{-3}$, the average of the values from the 3–3 and 3d–4f transitions for both the minor axis and the entire nebula of NGC 6153.

Table 17. Recombination line C^{3+}/H^+ and N^{3+}/H^+ abundances.

		Minor axis		Entire nebula	
λ_0 (Å)	Mult	I_{obs}	$10^4 \times \frac{C^{3+}}{H^+}$	I_{obs}	$10^4 \times \frac{C^{3+}}{H^+}$
4650	V1	.513	1.56	.499	1.52
4187	V18	.068	1.02	.078	1.17
λ_0 (Å)	Mult	I_{obs}	$10^4 \times \frac{N^{3+}}{H^+}$	I_{obs}	$10^4 \times \frac{N^{3+}}{H^+}$
4379[a]	V18	.606	2.51	.566	2.34

[a] Corrected for a contribution of 13 per cent from Ne II λ4379.55 (V 60b), assuming Ne II $I(\lambda 4379.55)/I(\lambda 4391.99) = 0.61$.

Table 18. Adopted recombination line abundances, X^{i+}/H^+, for C, N, O and Ne ions, in units of 10^{-4}.

Ion	Minor axis	Entire nebula
C^{2+}	23.5	22.5
C^{3+}	1.29	1.34
N^{2+}	17.5	17.2
N^{3+}	2.51	2.34
O^{2+}	40.7	40.8
Ne^{2+}	15.9	15.9

3.5.6 *C^{3+}/H^+ and N^{3+}/H^+*

The C^{3+}/H^+ and N^{3+}/H^+ abundance ratios derived from the λ4650 (V 1) and λ4187 (V 18) C III recombination lines and from the λ4379 (V 18) N III recombination line are listed in Table 17. The N III 4d ^{2}D–5f ^{2}F^o λ4002 line of multiplet V 17 is also detected along the minor axis. However, no effective recombination coefficient is available for this line. A number of O III permitted lines have been detected. Nearly all these lines are excited by the Bowen fluorescence mechanism or by the radiative charge transfer reaction of O^{3+} and H^0 (Liu & Danziger 1993a; Liu, Danziger & Murdin 1993), instead of by recombination. The λ3715 O III 3p ^{3}P–3d ^{3}D^o multiplet V 14 cannot be excited by the Bowen fluorescence mechanism or by a charge transfer reaction. It is likely to be excited only by recombination and is therefore a useful abundance indicator for O^{3+}/H^+. Unfortunately, no recombination coefficient is available for this multiplet. The effective recombination coefficient for the O III 3p ^{3}D–3d ^{3}F^o multiplet V 8 at 3265 Å is available from Péquignot et al. (1991), and was used to derive O^{3+}/H^+ abundances in a number of high-excitation PNe by Liu & Danziger (1993a). This multiplet has not been detected in our spectra of NGC 6153.

Our adopted C, N, O and Ne ionic abundances from optical recombination lines are summarized in Table 18.

3.5.7 Other permitted transitions from heavy elements

A number of ORLs from doubly excited spectral terms have been detected. For N III we have detected multiplet V 3 $3s'\,^4P^o$–$3p'\,^4D$ near 4515 Å and V 6 $3s'\,^2P^o$–$3p'\,^2D$ at 4200 Å of parentage $2p(^3P^o)$. For O II, we see V 15 $3s'\,^2D$–$3p'\,^2F^o$ at 4590 Å, V 35 $3p'\,^2F^o$–$3d'\,^2F$ at 4448 Å, V 36 $3p'\,^2F^o$–$3d'\,^2G$ at 4190 Å, V 101 $3d'\,^2G$–$4f'\,^2H[5]^o$ at 4254 Å and V 104 $3d'\,^2P$–$4f'\,^2D[2]^o$ at 4488 Å, all of parentage $2p^2(^1D)$. The excitation of these lines is probably dominated by dielectronic recombination, and they are potentially valuable abundance diagnostics. However, relevant atomic data for the analysis of these lines are not yet available.

Nearly all the optical O III lines excited by the Bowen fluorescence mechanism and by the charge transfer reaction of $O^{3+} + H^0$ have been detected. The N III lines at 4640 Å (multiplet V 2) and at 4097 Å (V 1), produced by a secondary Bowen fluorescence mechanism, are also detected. Detailed observational studies of the O III Bowen fluorescence mechanism and the O^{3+} radiative charge transfer reaction for a number of high-excitation PNe were presented by Liu & Danziger (1993a) and Liu et al. (1993). The efficiency of the Bowen fluorescence process, $\Re$, defined as the fraction of all those He^+ Lyα photons created following recombination which are converted to photons in O III transitions, other those in $2p3d$–$2p^2$ transitions, can be derived from the observed intensity of He II λ4686 and the pure Bowen fluorescence line O III λ3133,

$$\Re = 1.02\,\frac{\alpha(\mathrm{He\,II}\,\lambda4686)}{\alpha(\mathrm{He\,II\,Ly}\alpha)} \times \frac{I(\lambda3133)}{I(\lambda4686)},$$

where α(He II λ4686) and α(He II Lyα) are respectively the effective recombination coefficients of the He II λ4686 and Lyα lines. For $T_e = 9100$ K and $N_e = 3500\,\mathrm{cm}^{-3}$ α(He II λ4686)/α(He II Lyα) = 0.319 (Storey & Hummer 1995). For the minor axis of NGC 6153, our observations yield $I(\lambda3133)/I(\lambda4686) = 1.83$, thus $\Re = 0.59$. The efficiency of the Bowen fluorescence mechanism depends on a number of nebular properties, in particular the optical depths of He II Lyα and the O III resonance lines (e.g. Kallman & McCray 1980). It is interesting to note that NGC 6153 has one of the highest Bowen fluorescence efficiencies found for PNe. Liu et al. (1993) measured the Bowen fluorescence efficiencies for a large sample of PNe and found that $\Re$ increases with O^{2+}/H^+. The high Bowen efficiency of NGC 6153 is consistent with the very high O^{2+}/H^+ ratio derived from the O II recombination lines.

3.6 Comparison of ORL and CEL abundances

The ionic abundances derived from the UV, optical and IR collisionally excited lines (Table 8) and those from ORLs (Table 18) are compared in Fig. 11. The most striking feature of Fig. 11 is that in all cases where ionic abundances have been derived both from ORLs and from CELs (UV, optical or IR), the values from the ORLs are approximately a factor of 10 higher than those derived from the CELs, with the possible exception of N^{2+}/H^+, for which the value derived from the UV intercombination line λ1751 falls halfway between those derived from the far-IR [N III] 57-μm line and from the N II optical recombination lines. The λ1751 line is, however, of low S/N ratio, and may be subject to SWP camera artefacts that mimic emission lines at 1663 and 1750 Å, precisely at the wavelengths of the O III] λ1663 and N III] λ1751 lines (Crenshaw, Bruegman & Norman 1990). For O^{2+}/H^+, Ne^{2+}/H^+ and S^{2+}/H^+, the abundances derived from the infrared fine-structure lines, which are insensitive to the adopted T_e given the very small excitation energies of these lines, agree well with those derived from the optical forbidden lines.

Fig. 11 shows no correlation between the magnitude of the

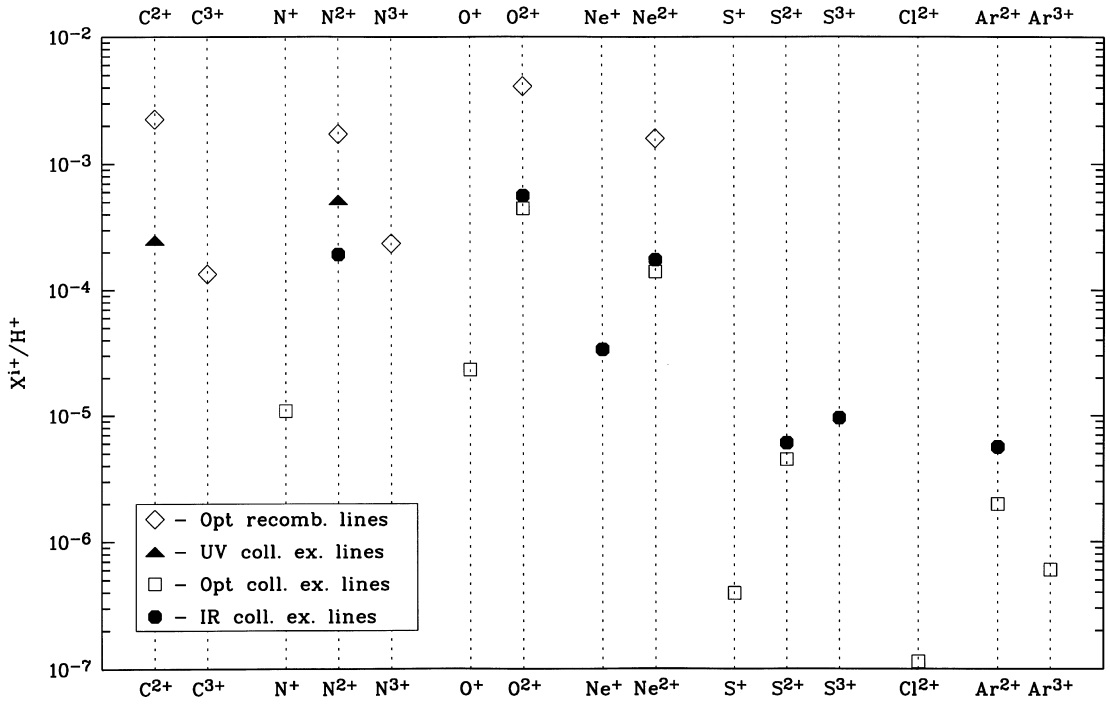

Figure 11. Comparison of ionic abundances derived from optical recombination lines, and from UV, optical and IR collisionally excited lines. The values plotted are for the entire nebula.

abundance discrepancies for individual ions, derived from ORLs on the one hand and from CELs on the other, and the excitation energies of the CELs. Similarly, no correlation is apparent between the discrepancies and the critical densities of the IR lines, which vary from less than 3000 cm^{-3} for the [O III] 52, 88-μm lines and the [N III] 57-μm line to 15 000 cm^{-3} for the [S III] 18.7-μm line and 2×10^5 cm^{-3} for the [Ne III] 15.5-μm line. Adopting a higher N_e of 3500 cm^{-3}, as derived from the optical [Ar IV] and [Cl III] doublet ratios, rather than 1660 cm^{-3} given by the [O III] 88 μm/52 μm ratio, increases the IR fine-structure line O^{2+}/H^+ and N^{2+}/H^+ abundances by approximately 80 per cent, but hardly affects the IR fine-structure line Ne^{2+}/H^+ and S^{2+}/H^+ abundances (Table 8).

Comparison of Table 18 with Table 8 shows that although the absolute values of the ionic abundances derived from ORLs are much higher than those derived from CELs, the two techniques yield identical *relative* heavy-element ionic abundances. This constancy of derived ionic *ratios* has already been commented upon for other PNe (Barlow 1995; Mathis, Torres-Peimbert & Peimbert 1998; Liu et al. 1999), with the conclusion that reliable C/O, N/O, Ne/O, etc., ratios can be derived from nebular observations, provided that the same type of line is used in deriving both ionic abundances in a ratio, i.e., both abundances should be based on ORLs or both should be based on CELs.

Although the absolute magnitude of its discrepancy differs, it is remarkable to note that for NGC 7009, studied by LSBC, the ORL abundances for C, N and O were also all higher than the corresponding CEL values by a uniform amount, a factor of 5 in that case. The implications of these findings for the various scenarios proposed to explain the large abundance discrepancies will be discussed in Section 5.

3.7 Total elemental abundances

The total elemental abundances derived for NGC 6153 from CELs and ORLs are presented in Table 19, together with those derived previously by PDM and by Kingsburgh & Barlow (1994). For He/H, PDM and Kingsburgh & Barlow derive 0.13 and 0.102 respectively. The former is in excellent agreement with our result. For comparison, also listed in Table 19 are the average abundances of Galactic PNe derived by Kingsburgh & Barlow and the solar photospheric abundances compiled by Anders & Grevesse (1989) and Grevesse & Noels (1993).

Table 19. Elemental abundances by number, derived from CELs and ORLs, in units such that $\log N(\mathrm{H}) = 12.0$.

Ref	He	C	N	O	Ne	S	Cl	Ar
				Recombination lines				
(1)	11.13	9.42	9.32	9.66	9.29			
(2)	11.14	9.40	9.31	9.66	9.29			
				Collisionally excited lines				
(1)			8.36	8.69	8.25	7.23	5.62	6.40
(2)		8.44	8.36	8.70	8.23	7.21	5.62	6.43
(3)		8.90	9.30	9.00	8.40	7.57		7.00
(4)		8.14	8.72	8.70	8.18			
(5)	11.06	8.74	8.35	8.68	8.09	6.92		6.39
(6)	10.99	8.55	7.97	8.87	8.09	7.21	5.50	6.56

(1) This work, for the minor axis;
(2) This work, for the whole nebula;
(3) Pottasch, Dennefield & Mo (1986; PDM);
(4) Kingsburgh & Barlow (1994);
(5) Average abundances of PN from Kingsburgh & Barlow (1994);
(6) Solar photospheric abundances from Anders & Grevesse (1989) and Grevesse & Noels (1993). Grevesse & Sauval (1998) suggested preliminary revised values for the solar C, N and O abundances of 8.52, 7.92 and 8.83 respectively, slightly lower than the values adopted here. The new recommended solar abundances of Ne, S and Ar are 8.08, 7.33 and 6.40 respectively, while there is no change for Cl.

Whenever available, the ionization correction factors (ICFs) given by Kingsburgh & Barlow (1994) were used. The forbidden line O/H abundance ratio was calculated from the O^+/H^+ derived from the [O II] λλ3726, 3729 lines[5] and the O^{2+}/H^+ ratio derived from the [O III] λλ4959, 5007 lines, correcting for the unseen O^{3+} using,

$$\frac{\mathrm{O}}{\mathrm{H}} = ICF(\mathrm{O}) \times \left(\frac{\mathrm{O}^+}{\mathrm{H}^+} + \frac{\mathrm{O}^{2+}}{\mathrm{H}^+}\right)$$

$$= \left(\frac{\mathrm{He}^+ + \mathrm{He}^{2+}}{\mathrm{He}^+}\right)^{2/3} \times \left(\frac{\mathrm{O}^+}{\mathrm{H}^+} + \frac{\mathrm{O}^{2+}}{\mathrm{H}^+}\right).$$

From the He^+ and He^{2+} abundances given in Table 9, we have $ICF(O) = 1.06$ for both the minor axis and the entire nebula of NGC 6153.

A recombination line O^+/H^+ abundance is not available, so to make use of the above equation, we assume that the recombination line O^+/O^{2+} ratio is the same as that derived from the CELs. Given the small ionic concentration of O^+ (about 5 per cent), the errors introduced should be negligible.

Both C^{2+}/H^+ and C^{3+}/H^+ have been derived from recombination lines. The unseen C^+/H^+ is corrected for, using

$$\frac{\mathrm{C}}{\mathrm{H}} = \left(1 + \frac{\mathrm{O}^+}{\mathrm{O}^{2+}}\right) \times \left(\frac{\mathrm{C}^{2+}}{\mathrm{H}^+} + \frac{\mathrm{C}^{3+}}{\mathrm{H}^+}\right).$$

For the collisionally excited lines, only C^{2+}/H^+ is available and we assume $C^{3+}/C^{2+} = 0.060$ for the whole nebula of NGC 6153, as given by ORLs.

Recombination-line abundances are available for N^{2+}/H^+ and N^{3+}/H^+ ratios but not for N^+/H^+. The latter is, however, available from the collisionally excited [N II] λλ6548, 6584 lines. The N^{2+}/H^+ ratio derived from the UV collisionally excited N III] λ1751 line is significantly higher than that deduced from the [N III] 57-μm far-IR fine-structure line. Given the weakness of the λ1751 line and the fact that its measured flux could be affected by camera artefacts, we will adopt the N^{2+}/H^+ ratio derived from the far-IR line. N^{2+}/H^+ from the 57-μm line and N^+/H^+ from the λλ6548, 6584 lines yield $N^+/N^{2+} = 0.056$ for the whole nebula of NGC 6153. Assuming that this is also valid for the corresponding abundances derived from ORLs, the total recombination line N/H abundance is given by

$$\frac{\mathrm{N}}{\mathrm{H}} = 1.056 \times \frac{\mathrm{N}^{2+}}{\mathrm{H}^+} + \frac{\mathrm{N}^{3+}}{\mathrm{H}^+}.$$

To obtain the collisional line N/H abundance for the whole nebula, we correct for the unseen N^{3+}/H^+ assuming $N^{3+}/N^{2+} = 0.136$, as given by ORLs, so that

$$\frac{\mathrm{N}}{\mathrm{H}} = \frac{\mathrm{N}^+}{\mathrm{H}^+} + 1.136 \times \frac{\mathrm{N}^{2+}}{\mathrm{H}^+}.$$

[5] To maintain consistency for the analysis of the CELs and of the ORLs, recombination excitation of the [O II] λλ3726, 3729 doublet (cf. Section 3.3) will be neglected. Given the small ionic concentration of O^+, the errors introduced to the total O/H elemental abundances deduced below, both from CELs and from ORLs, should be negligible.

The collisional line N/H abundance for the minor axis of NGC 6153 is quite uncertain, as only N^+/H^+ derived from the [N II] $\lambda\lambda$6548, 6584 lines is available. The standard approach adopted for the traditional abundance determinations in such a situation is to use the ICF formula,

$$\frac{N}{H} = ICF(N) \times \frac{N^+}{H^+} = \frac{O}{O^+} \times \frac{N^+}{H^+},$$

which yields N/H = 8.36 with an ICF correction $O/O^+ = 18.7$. The exact agreement of this result with that derived for the whole nebula (Table 19) seems somewhat fortuitous.

Ne^+/H^+ and Ne^{2+}/H^+ ionic abundances are available for the whole nebula from IR and optical CELs. For Ne^{2+}/H^+, we adopt the abundance derived from the [Ne III] $\lambda\lambda$3868, 3967 optical lines, which is only 20 per cent lower than derived from the *IRAS* LRS observation of the 15.5-μm IR fine-structure line. Ne^{2+} has an ionization potential of 62.7 eV, significantly larger than those of doubly ionized C, N and O as well as being higher than the 54.4-eV ionization potential of He^+. We thus expect that the ionic concentration of Ne^{3+} should be negligible (cf. Section 3.4) and that

$$\frac{Ne}{H} = \frac{Ne^+}{H^+} + \frac{Ne^{2+}}{H^+}.$$

Note that the assumption that Ne^+ is negligible (Kingsburgh & Barlow 1994) is inconsistent with the observations of NGC 6153 (Table 8). The ionization potential of Ne^+, 41.0 eV, is significantly larger than those of the singly ionized ions C^+, N^+ and O^+. For NGC 6153, we find $Ne^+/Ne^{2+} = 0.24$.

The collisional line Ne/H abundance for the minor axis, and the recombination line Ne/H abundances for both the minor axis and the whole nebula, are calculated using

$$\frac{Ne}{H} = 1.24 \times \frac{Ne^{2+}}{H^+}.$$

For elements heavier than Ne, only ionic abundances from CELs are available. For S, we have S^+/H^+ from the [S II] $\lambda\lambda$6716, 6731 lines and S^{2+}/H^+ from [S III] λ6312. For the whole nebula, S^{2+}/H^+ is also available from the [S III] 18.7-μm IR line, in addition to S^{3+}/H^+ from [S IV] 10.5 μm, which is well detected. Ionic abundances derived from the IR fine-structure lines have the advantage that they are essentially insensitive to the adopted T_e. In contrast, the S^{2+}/H^+ ratio derived from the λ6312 line is very sensitive to the adopted T_e, given the very high E_{ex} of the λ6312 line (3.9×10^4 K as compared to only 1200 K for the 18.7-μm line). The [S III] 18.7-μm line is, however, only marginally detected by the LRS. Given the large uncertainty of the 18.7-μm line flux, we adopt here the S^{2+}/H^+ ratio derived from the λ6312 line. S^{4+} is not observed. Since S^{3+} has an ionization potential of 47.3 eV, very similar to the value of 47.4 eV for N^{2+}, we assume that $S/S^{4+} = N/N^{3+}$. From the ionic and total N abundances derived from ORLs for the whole nebula, we have $N^{3+}/N = 0.115$, thus for the entire nebula,

$$\frac{S}{H} = \left(\frac{S^+}{H^+} + \frac{S^{2+}}{H^+} + \frac{S^{3+}}{H^+}\right)/(1 - 0.115).$$

For the minor axis of NGC 6153, S^{3+}/H^+ is not available and we assume that the value of $S^{3+}/S^{2+} = 2.13$ derived for the whole nebula is also valid for the minor axis, in which case the S/H ratio for the minor axis is given by

$$\frac{S}{H} = \left(\frac{S^+}{H^+} + 3.13 \times \frac{S^{2+}}{H^+}\right)/(1 - 0.115).$$

Cl is not discussed by Kingsburgh & Barlow (1994). Based on the similarities of the ionization potentials of Cl ion stages to those of the S ion stages, we derive the elemental Cl/H abundance using

$$\frac{Cl}{H} = \frac{S}{S^{2+}} \times \frac{Cl^{2+}}{H^+}.$$

The [Ar III] 9.0-μm line is only marginally detected by the LRS, and so we use Ar^{2+}/H^+ derived from the [Ar III] λ7135 line only. Ar^{3+} has an ionization potential of 59.8 eV, larger than that of He^+; thus the ionic concentration of Ar^{4+} should be negligible. The unseen Ar^+ is corrected for assuming $Ar^+/Ar = N^+/N$, in which case

$$\frac{Ar}{H} = \left(\frac{Ar^{2+}}{H^+} + \frac{Ar^{3+}}{H^+}\right) \Big/ \left(1 - \frac{N^+}{N}\right).$$

From the ionic and total N abundances derived from CELs, we have $N^+/N = 0.054$ and 0.048 for the minor axis and for the whole nebula respectively, allowing us to derive the Ar elemental abundances listed in Table 19.

Given that PDM derived very large C, N, O and Ne overabundances in NGC 6153, from their analysis of its UV, optical and IR collisionally excited lines (see Table 19 for a summary), it is worth noting that our own analysis of NGC 6153's CELs yields a 'normal' oxygen abundance, together with carbon and nitrogen abundances that lie within the range found for other PNe. However, we confirm their finding that neon is more abundant than in other planetary nebulae – our CEL analysis implies an abundance enhancement of 0.15 dex for this element relative to other PNe. NGC 6153's He/H ratio of 0.137 (Table 9) and its N/O ratio of 0.46 mean that it would be classified as a Type I planetary nebula using the original criteria of Peimbert & Torres-Peimbert (1983), although it would not satisfy Kingsburgh & Barlow's (1994) revised criterion that Type I Galactic PNe should have $N/O > 0.8$.

4 SPATIAL VARIATIONS OF NEBULAR PROPERTIES

To explore possible physical causes of the factor of 10 discrepancy between the C, N, O and Ne abundances derived from ORLs and from CELs, our deep long-slit spectra obtained along the minor axis of NGC 6153 have been used to map the spatial variations of nebular properties, such as extinction, electron temperature and density, and elemental abundances, across the nebular surface. The results are presented in this section.

The current data set is unfortunately limited by its relatively low spatial angular resolution. During all three observing runs at the ESO 1.52-m telescope, the CCD was binned by a factor of 2 along the slit in order to reduce the readout noise and improve the S/N ratios of the weak ORLs of interest here. As a result of the binning, each pixel along the slit projected to 1.63 arcsec on the sky. The typical seeing during the observations was about 1 arcsec; thus the spectra obtained were spatially undersampled. A further complication when using the long-slit spectra to map the nebular properties across the surface, which often involves ratioing the derived surface brightness distribution along the slit of two diagnostic lines of different wavelength, falling on different parts

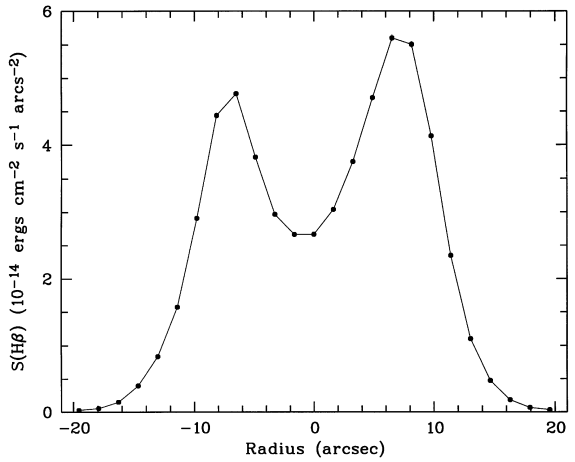

Figure 12. The Hβ surface brightness distribution along the minor axis of NGC 6153. Extinction has not been corrected for. Positive radius is to the south-east of the nebular centre (cf. Fig. 1).

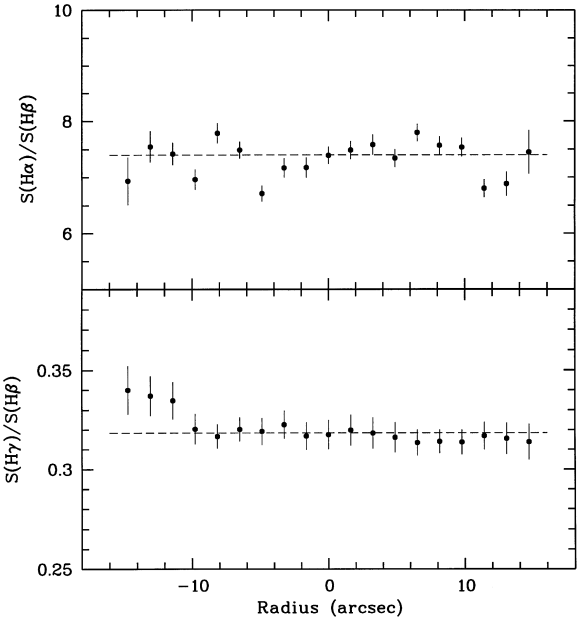

Figure 13. Variations of the surface brightness distribution ratios of H Balmer lines, $S(\mathrm{H}\alpha)/S(\mathrm{H}\beta)$ and $S(\mathrm{H}\gamma)/S(\mathrm{H}\beta)$, along the nebular minor axis. The dashed lines show the corresponding average values derived after integrating along the slit (Table 2).

of the CCD detector, arises from the imperfect alignment of the spectral dispersion along CCD rows and from the effect of atmospheric differential refraction. As a result, two pixels from the same CCD row but of different column numbers (wavelengths) sample slightly different parts of the nebula. Fortunately, the central star of NGC 6153 is bright enough ($B \sim 16$) to be well detected in our slit spectra. The derived central star position along the slit as a function of wavelength was used to trace and correct for the distortion along the slit. The drift of the nebula perpendicular to the slit caused by atmospheric differential refraction could not be traced. However, given the more or less spherical nebular shape, the uncertainties introduced by the latter were probably not significant. For all the grating set-ups used, the maximum distortion along the slit derived from the central star position amounted to about 0.2 pixel, or 0.33 arcsec, from one end to the other of the whole CCD wavelength coverage. Once the distortion as a function of wavelength (or equivalently the column number of the CCD frame) had been determined, each column of the frame was shifted accordingly and rebinned to a common grid. Although seemingly small, the distortions, if unaccounted for, can introduce significant errors in surface brightness ratios involving two lines that fall far apart on the CCD frame, given the steep radial variations of nebular surface brightness (Fig. 12) and the fact that the spectra were spatially undersampled. Finally, to minimize any effects caused by variations in seeing conditions between exposures, surface brightness distributions derived from the same exposures were always used to calculate line ratios.

4.1 Extinction as a function of position

The variations of the surface brightness distribution ratios of H Balmer lines, $S(\mathrm{H}\alpha)/S(\mathrm{H}\beta)$ and $S(\mathrm{H}\gamma)/S(\mathrm{H}\beta)$, along the nebular minor axis are plotted in Fig. 13. Also shown are the average values of $S(\mathrm{H}\alpha)/S(\mathrm{H}\beta)$ and $S(\mathrm{H}\gamma)/S(\mathrm{H}\beta)$, derived after integrating the spectra along the slit. With standard deviations of only 4 and 2 per cent respectively,[6] both $S(\mathrm{H}\alpha)/S(\mathrm{H}\beta)$ and $S(\mathrm{H}\gamma)/S(\mathrm{H}\beta)$ are constant along the minor axis and consistent with the mean values calculated from the integrated line fluxes (Table 2).

An uncertainty of 4 per cent in the measured $S(\mathrm{H}\alpha)/S(\mathrm{H}\beta)$ ratio yields an error of only 0.05 dex in the derived $c(\mathrm{H}\beta)$. The constancy of the Balmer line ratios along the minor axis of NGC 6153 (Fig. 13) suggests that the fairly large extinction of $(\mathrm{H}\beta) = 1.30$ towards this nebula is almost entirely due to reddening by intervening interstellar medium along the line of sight. This is consistent with the fact that NGC 6153 appears to have little or no surrounding neutral material (cf. Section 2.1.4). In the following discussion, a constant extinction of $c(\mathrm{H}\beta) = 1.30$ will be used to deredden all line fluxes measured along the minor axis.

4.2 T_e and N_e as a function of position

The electron temperatures derived from the [O III] λ4959/λ4363 ratio and from the ratio of the nebular continuum Balmer discontinuity to H 11, as a function of the slit position along the nebular minor axis are shown in Fig. 14. The [O III] λ5007 line was not used in calculating T_e([O III]), since this line was covered only in our low-resolution spectra and was saturated on the deep exposures. The λ4959 line was not saturated on the three 30-min high-resolution spectra covering 4000–4984 Å obtained in 1997 July, so these three spectra were used to produce the [O III] temperatures plotted in Fig. 14.

The [O III] temperatures show smooth variations along the nebular minor axis, decreasing outwards from a peak value of 9400 K at the centre to about 8200 K at a radius of 14 arcsec, the maximum radius where T_e([O III]) can be determined. The variation as a function of nebular radius can be well fitted with a second-order polynomial. In contrast, within the measurement errors ($\lesssim$500 K), the derived values of T_e(BJ) at different positions are approximately constant, and are consistent with the mean

[6] The scatter of the $S(\mathrm{H}\alpha)/S(\mathrm{H}\beta)$ ratios is larger than that of $S(\mathrm{H}\gamma)/S(\mathrm{H}\beta)$, because in order to calculate the former ratios with both Hα and Hβ measured from the same frame, the $\lambda\lambda$3523–7421 spectrum of only 2-min integration time had to be used – Hα was saturated on the two 10-min exposures. In contrast, $S(\mathrm{H}\gamma)/S(\mathrm{H}\beta)$ ratios were derived from several 4000–4985 Å high-resolution spectra, each of 30-min integration time (cf. Table 1).

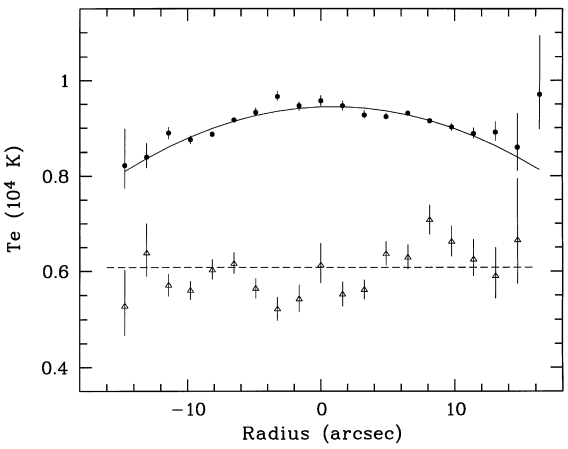

Figure 14. Variations of the electron temperatures derived from [O III] λ4959/λ4363 (solid circles) and the ratio of the nebular continuum Balmer discontinuity to H 11 (open triangles). The solid curve is a second-order polynomial fit to the [O III] temperatures, and the dashed line shows the mean Balmer jump temperature derived after integrating the spectrum along the slit.

value of 6080 K derived from the integrated spectrum. Thus the Balmer jump temperatures are between 2200 and 3400 K lower than the [O III] temperatures.

We showed in Section 3.3 that for the nebula as a whole, recombination excitation of the λ4363 is insignificant and the correction to T_e([O III]) due to this contamination amounts to only 200 K, even if the higher O abundance derived from ORLs is adopted. The contamination is, however, not uniform across the nebula, being larger at the centre because of the higher O^{3+}/H^+ ionic concentration in the nebular inner regions and should decrease to zero at the boundary where there is no triply ionized O. The contamination remains negligible even at the nebular centre if we adopt the lower O abundance derived from the CELs. If we take the recombination line O^{2+}/H^+ abundances mapped by the O II multiplet V 1 at 4650 Å, plotted in Fig. 18, multiply the values by 1.35 to account for the lower abundance yielded by this multiplet compared to other O II recombination lines from 3p–3d and 3d–4f configurations (cf. Tables 14, 15 and 18), and use the total and ionic He abundances (Fig. 16) to estimate the ionic concentration of O in the ionization stage of O^{3+} (cf. Section 3.7), then from equation (3) we find that recombination excitation can contribute 15 per cent of the observed λ4363 line flux at the nebular centre. After correcting for this contamination, T_e([O III]) at the nebular centre drops by 440 K, about one-third of the total variation in the [O III] temperature across the nebular minor axis shown in Fig. 14. While difficult to rule out completely, given the possible uncertainties in the estimate of the O^{3+} ionic concentration based on the He ionic abundances, it does not seem to us that recombination excitation of the λ4363 line alone can account for all the variations of T_e([O III]) shown in Fig. 14.

The electron density variations across the nebular surface have been mapped using the [Ar IV], [Cl III], [O II] and [S II] doublet ratios and are plotted in Fig. 15. Note that the [O II] λ3729/λ3726 doublet ratio remains as a valid density diagnostic even if recombination may contribute to the emission of the doublet (cf. Section 3.2, Section 3.3). The densities derived from the four diagnostics agree remarkably well, and all show similar variations of a factor of 2 across the nebular surface. There is evidence of a local minimum with $N_e = 3000\,cm^{-3}$ about 1–2 arcsec from the

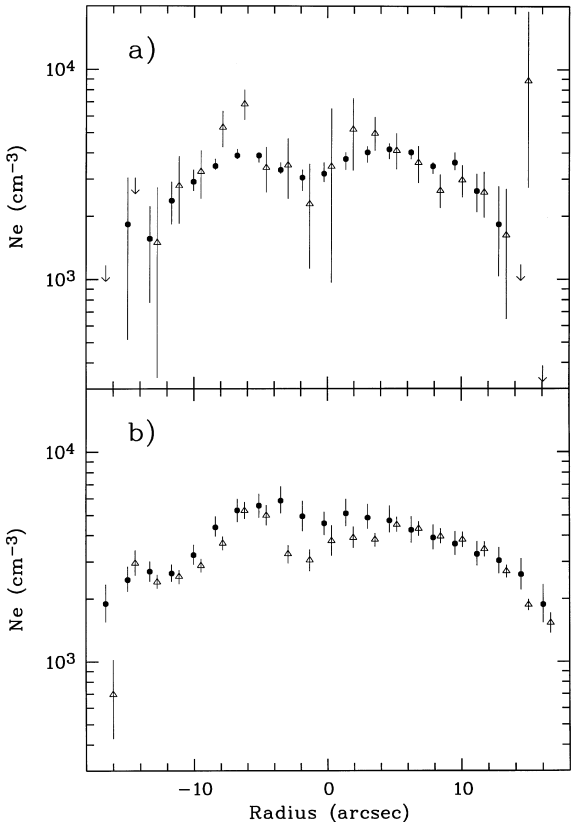

Figure 15. Variations of the electron density, derived from (a) [Ar IV] λ4740/λ4711 (solid circles) and [Cl III] λ5537/λ5517 (open triangles) ratios, and (b) from [O II] λ3729/λ3726 (solid circles) and [S II] λ6731/λ6716 (open triangles) along the minor axis of NGC 6153. To separate the error bars, the slit positions of data points derived from the [Ar IV] and [O II] ratios are shifted to the left by 0.25 arcsec, and those from the [Cl III] and [S II] ratios are shifted to the right by the same amount.

nebular centre. A careful look at the Hβ surface brightness distribution plotted in Fig. 12 shows that its central minimum is also offset by about 2 arcsec from the centre. From this local minimum, the density increases slightly outwards in both directions, reaching a maximum value of $4000\,cm^{-3}$ at a distance of about 5 arcsec, i.e., near the inner edges of the bright shell; it then decreases again to a low value of $2000\,cm^{-3}$ at radii of 15 arcsec, outside the bright shell. The optical appearance of NGC 6153 (Fig. 1) and the electron density distribution derived here thus suggest that NGC 6153 is a bipolar nebula, probably with a central cavity and a density-enhanced waist, and is viewed at a small angle to its polar axis.

4.3 Ionic abundances as a function of position

Fig. 16 shows the ionic and total abundances of He derived from He I and He II recombination lines. The fraction of He in the doubly ionized state provides a method of estimating the ionic concentration of unseen heavy-element species such as O^{3+} (Section 3.7). Also, because He abundances are based on ORLs, the results provide an interesting comparison to the C^{2+}/H^+ and O^{2+}/H^+ abundances derived from C II and O II recombination lines. As already noted when analyzing results from the integrated fluxes, the He^+/H^+ ratio derived from the singlet λ6678 line is systematically lower than those derived from the λ4471 and

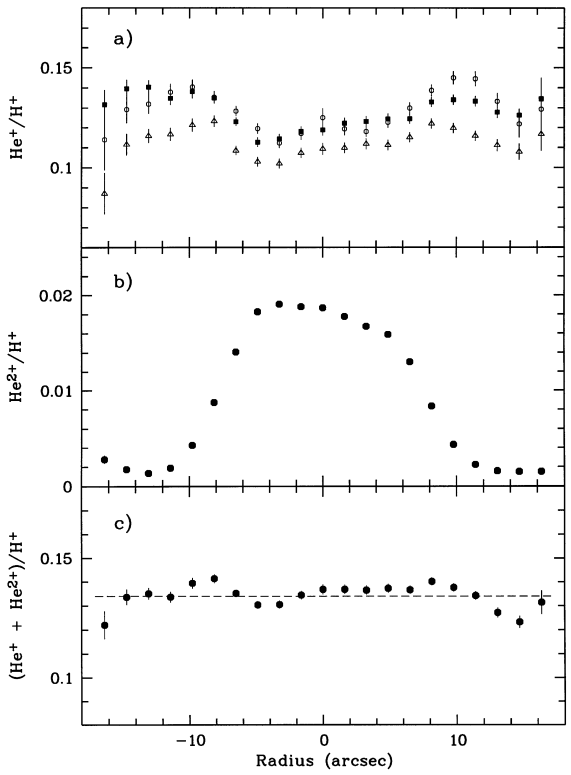

Figure 16. Variations along the minor axis of NGC 6153 of (a) He^+/H^+ derived from He I λ4471 (open circles), from λ5876 (solid boxes) and from λ6678 (open triangles); (b) He^{2+}/H^+ derived from the He II λ4686 line, and (c) the elemental abundance ratio $He/H \equiv He^+/H^+ + He^{2+}/H^+$, where He^+/H^+ is the average of the values deduced from the $\lambda\lambda$4471, 5876 and 6678 lines weighted by 1:3:1 respectively. The dashed line in (c) denotes the value derived from line fluxes integrated along the slit.

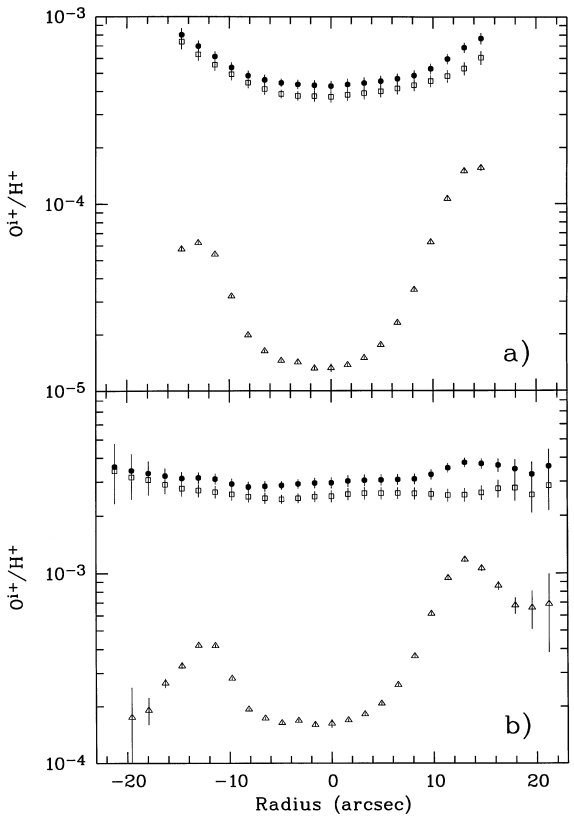

Figure 17. Variations along the minor axis of NGC 6153 of the forbidden line abundances of O^+/H^+ (open triangles), O^{2+}/H^+ (open boxes) and the total elemental abundance $O/H \equiv (O^+/H^+ + O^{2+}/H^+) \times (He/He^+)^{2/3}$ (filled circles). The O^{2+}/H^+ abundances were derived using the electron density given by the [Ar IV] doublet ratio, whereas the densities given by the [O II] doublet ratio were used for O^+/H^+. In (a) the abundances were calculated using the electron temperatures derived from the [O III] nebular to auroral line ratio (the solid curve in Fig. 14), and in (b) all abundances were calculated using a constant temperature of 6080 K, as given by the ratio of the nebular continuum Balmer discontinuity to H 11 (the dashed line in Fig. 14).

λ5876 triplet lines. Within a distance of 9 arcsec from the nebular centre, the ratio of He^+/H^+ values derived from the two triplet lines to that deduced from the λ6678 line is nearly constant, with an average value of 1.11 and a standard deviation of only 0.02. At large radii, the ratio increases slightly to about 1.20.

Fig. 16 shows a clear change in the He ionization degree with distance from the central star. For lines of sight within a distance of ~5 arcsec from the nebular centre, approximately 15 per cent of He is doubly ionized. Outside this, He^{2+}/H^+ decreases rapidly. Interestingly, He^{2+}/H^+ never reaches zero, and even at very large radii there is still about 1.5 per cent doubly ionized He. One possible explanation is that this is due to the projection of more diluted material along the nebular polar axis, where He is fully doubly ionized throughout. The derived total He/H abundance shows no gradient across the nebula, and is constant with a mean value of 0.133 and a standard deviation of 0.006.

The O^+/H^+ and O^{2+}/H^+ abundances derived respectively from the [O II] $\lambda\lambda$3726, 3729 and [O III] λ4959 forbidden lines are presented in Fig. 17. The abundances were calculated for two cases. For (a), the actual electron temperatures across the nebula derived from the λ4959/λ4363 ratio were used. Given the sensitivity of the results to the adopted T_e, in order to minimize errors introduced by uncertainties in the temperature determinations, the smooth polynomial fit to the [O III] temperature as a function of radius was used (the solid line in Fig. 14) instead of the individual measurements. We have assumed that recombination excitation of the λ4363 line is insignificant, which is the case if the O abundances derived from these optical CELs are correct (cf. Section 4.2). Abundances are given only out to a radial distance of 15 arcsec, the maximum distance from the nebular centre where T_e([O III]) has been determined. In (b), a constant temperature of 6080 K, as given by the nebular continuum Balmer discontinuity (cf. Fig. 14), was used for all abundance calculations. The abundances are calculated out to the edge where the λ4959/Hβ ratio can be determined. In both cases, the O^{2+}/H^+ abundances were calculated using the electron densities derived from the [Ar IV] λ4740/λ4711 doublet ratio (Fig. 15a) and those of O^+/H^+ using the densities derived from the [O II] λ3729/λ3726 doublet ratio (Fig. 15b). Over the density range of 2000–4000 cm^{-3}, the effect of a varying N_e on the λ4959 O^{2+}/H^+ abundance is negligible. It can, however, affect the derived $\lambda\lambda$3726, 3729 O^+/H^+ abundance by up to 20 per cent. Also shown are the total O/H abundances after correcting for the unseen O^{3+} species using the He ionic abundances plotted in Fig. 16 (cf. Section 3.7). The corrections are small even near the nebular centre.

Apart from the fact that the derived abundances differ by about an order of magnitude for the two cases of T_e adopted, an interesting aspect of Fig. 17 is that the O/H abundance ratio plotted in panel (a), derived using the varying [O III] temperatures

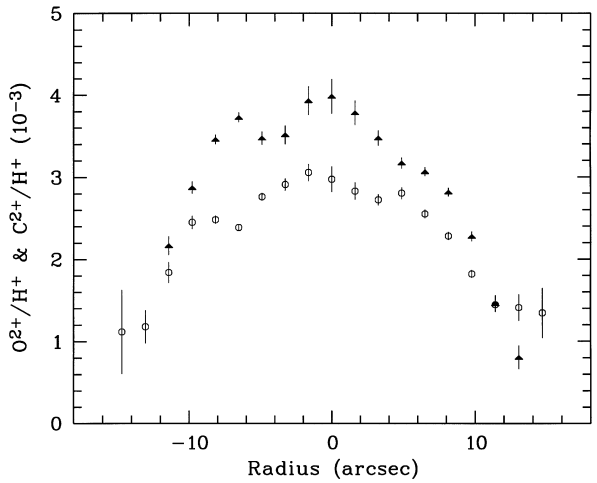

Figure 18. Ionic recombination line abundances of C^{2+}/H^+ (open circles) and O^{2+}/H^+ (solid triangles), derived respectively from the C II λ4267 line and from the O II 4650 Å multiplet.

measured from the [O III] nebular to auroral line ratio, increases smoothly outwards from the nebular centre, by about a factor of 2 over the radius range where the [O III] temperatures are available. In contrast, when a constant T_e was used, as in the case of panel (b), the derived O/H abundance is largely constant. Over the entire radial range plotted in panel (b), O/H has a average value of 0.0032 and a standard deviation of 0.0003.

Of the many ORLs from heavy-element ions, only a few are strong enough to be mapped across the nebular surface with useful accuracy. In Fig. 18 we plot the distributions of C^{2+}/H^+ and O^{2+}/H^+, mapped respectively from the C II λ4267 line and O II multiplet V 1 at 4650 Å. Both show similar radial variations, decreasing by approximately a factor of 2–3 from the centre to the outer edge, at a distance of 15 arcsec, where the lines are still detectable. Given the distributions of the He ionic abundances in Fig. 16 and the small ionic concentration of O in the form of O^+ as suggested by the CEL analysis (Fig. 16), it is reasonable to assume that for any line of sight along the nebular minor axis, the total ionic fraction of O in the form of O^+ and O^{3+}, or of C in the form of C^+ and C^{3+}, is likely to be less than 25 per cent. The C^{2+}/H^+ and O^{2+}/H^+ ionic abundance gradients shown in Fig. 18 indicate the presence of carbon and oxygen abundance gradients in NGC 6153, provided that the C^{2+}/H^+ and O^{2+}/H^+ abundances derived from the ORLs are correct and have not been contaminated by some unknown process which can yield the apparent radial variations of the ORL intensities *relative* to Hβ.

We have shown in Section 3.3 that if one takes the high O^{2+}/H^+ abundance of 4×10^{-3} deduced from the *permitted* O II optical recombination lines, then our new effective recombination coefficient calculations for the [O II] metastable levels (cf. Appendix A) predict that the observed fluxes of the [O II] auroral lines at 7320, 7330 Å and of the nebular lines at 3726, 3729 Å can be entirely due to recombination excitation for the case of a low-density uniform nebula. We also find that the intensity ratio of the nebular to auroral lines is consistent with the predictions of recombination theory. In such a case, we would, however, expect the forbidden nebular and auroral lines to have surface brightness distributions similar to permitted O II recombination lines, such as multiplet V 1 at 4649 Å. In Fig. 19(a) we compare the surface brightness distributions of these lines along the nebular minor axis. Fig. 19(a) shows that the spatial distribution of the forbidden

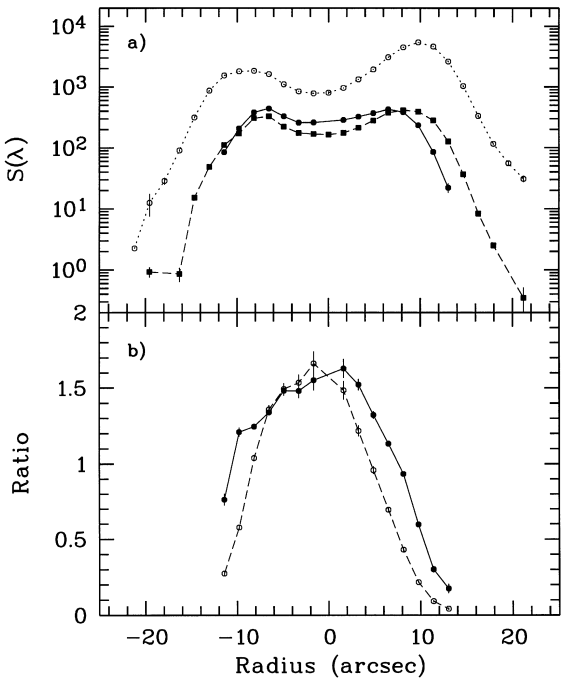

Figure 19. (a) Surface brightness distributions of (i) O II multiplet V 1 at 4649 Å (filled circles, solid line); (ii) [O II] $\lambda\lambda$7320, 7330 (filled boxes, dashed line); (iii) [O II] $\lambda\lambda$3726, 3729 (open circles, dotted line) along the nebular minor axis. A constant extinction correction of $c(H\beta) = 1.30$ across the nebula has been applied. (b) Ratios of the surface brightness distribution of O II multiplet V 1 λ4649 to those of the forbidden nebular lines $\lambda\lambda$3726, 3729 and auroral lines $\lambda\lambda$7320, 7330. (i) $S(\lambda4649)/S(\lambda\lambda7320,7330)$ (filled circles, solid line); (ii) $5\times S(\lambda4649)/S(\lambda\lambda3726,3729)$ (open circles, dashed line).

$\lambda\lambda$7320, 7330 auroral lines is indeed very similar to that of O II multiplet V 1, although some small differences are present beyond 8 arcsec to the south-east (positive radii) of the nebular centre, just outside the bright patch where the surface brightness of Hβ (Fig. 12) starts to decline sharply. Fig. 19(b) shows that the $S(\lambda4649)/S(\lambda\lambda7320, 7330)$ ratio is relatively flat in the central nebular regions, lending further support to the interpretation of recombination being the dominant excitation mechanism for the $\lambda\lambda$7320, 7330 lines. However, the spatial distribution of the [O II] $\lambda\lambda$3726, 3729 nebular lines differs significantly from that of O II V 1, peaking at much larger radii in both directions along the nebular minor axis. The $S(\lambda4649)/S(\lambda\lambda3726,3729)$ ratio falls off much more rapidly from the nebular centre than the $S(\lambda4649)/S(\lambda\lambda7320,7330)$ ratio (Fig. 19b). The forbidden nebular doublet is particularly strong outside the south-east bright patch.

The high-resolution *HST* image shown in Fig. 1 reveals an extremely rich network of loops, filaments and condensations. Located at the centre of the bright south-east patch, at a position angle of PA = 117.°9 and a radius of 7.9 arcsec from the central star, is an extremely bright condensation, which remains unresolved even with the *HST* resolution. The long-slit used for our ESO 1.52-m telescope observations, at PA = 122.°8, passed through a series of condensations (filaments) found at the southern crescent edge of the bright patch. These condensations were not resolved in our long-slit spectra, given the fairly low spatial resolution (1.63 arcsec per pixel along the slit). Clearly, NGC 6153 is far from being a homogeneous nebula. As we will show in Section 5.5, inhomogeneous nebular models containing H-deficient knots embedded in diffuse gas of more or less 'normal' metallicity

can account for many of the observed patterns of NGC 6153, suggesting that NGC 6153 may have experienced a recent ejection of H-deficient knots, similar to those observed in the 'born-again' PNe Abell 30 and Abell 78 (Section 6). The excitation mechanisms for the [O II] forbidden lines in inhomogeneous nebular models will be discussed in Section 5.5.

5 POSSIBLE EXPLANATIONS FOR THE ABUNDANCE DISCREPANCIES

In Sections 3 and 4 we have derived the ionic abundances of C^{2+}/H^+, N^{2+}/H^+, O^{2+}/H^+ and Ne^{2+}/H^+ using a large number of optical recombination lines detected from this nebula in our deep optical spectra. With few exceptions, the relative intensities of the permitted ORLs from each species are in good agreement with the predictions of recombination theory. In all cases, the ionic abundances derived from ORLs are approximately an order of magnitude higher than those deduced from CELs – optical, UV or infrared, regardless of the excitation energies or critical densities of the latter. Spatial analysis along the nebular minor axis yields [O III] temperatures that decreases from 9400 K at the nebular centre to about 8200 K at a radius of 15 arcsec. In contrast, the Balmer jump temperatures are constant along the minor axis, and are 2000–3000 K lower than the [O III] temperatures. We find moderate variations in N_e by a factor of 2 from several optical density diagnostics. The total He/H abundance mapped by He I and He II recombination lines is constant across the nebula, whereas the C^{2+}/H^+ and O^{2+}/H^+ abundance ratios derived from C II and O II recombination lines decrease by a factor of 2–3 from the centre out to a radius of 15 arcsec, suggesting the presence of carbon and oxygen abundance gradients across the nebula. In the remainder of this section, we will address the reliability of heavy-element abundances derived from ORLs and discuss possible interpretations of the large discrepancy between abundances derived from these two types of emission lines in the context of temperature, density fluctuations and chemical inhomogeneities.

5.1 Reliability of heavy-element recombination coefficients

We have seen above that the heavy-element (all elements other than hydrogen and helium) abundances relative to hydrogen, derived from ORLs are larger by almost a factor of 10 than those derived from UV, optical and IR collisionally excited lines. The possibility that resonance line or continuum fluorescence (e.g. Grandi 1976) may be important in exciting the ORLs used here for abundance determinations can be ruled out based on the excellent agreement of the results obtained from multiple lines of different electron configurations and multiplicity. The excellent agreement of the observed intensities, relative to the 3d–4f λ4267 line, of the C II 4f–*n*g lines (which cannot be excited by any known resonance line or continuum fluorescence mechanism), with the predictions of C II recombination theory (Section 3.5.2, Table 12), provides further evidence that strongly argues against fluorescence as the cause of the very high C/H abundances derived from the ORLs. Is it possible that such a difference could be attributed in part, or in full, to the recombination coefficients used in the analysis? Incorrect recombination coefficients could arise in two ways; either the fundamental atomic data could be in error, or the overall atomic model could be incomplete, perhaps failing to include some important intrinsic atomic process. We note that the observational evidence so far argues against problems with the fundamental atomic data, since the discrepancy between ORL and CEL abundances varies greatly between PNe, ranging from less than a factor of 2, through the factor of 10 reported in the present work, up to more than a factor of 20 in the extreme case of the bulge PN M 1-42 (Liu et al. 1999).

The most recent calculations of effective recombination coefficients for line emission in light elements (Storey 1994; LSBC; Kisielius et al. 1998, Davey et al. 1999) all rely on bound–bound and bound–free radiative data calculated using the R-matrix method. This method is potentially of high accuracy, being particularly applicable to Rydberg states of atomic ions. In the calculations referred to above, the R-matrix method is typically used for all states up to valence electron principal quantum number $n = 10$. For these states, the calculated photoionization cross-sections typically show a continuum interrupted by resonances, which correspond to the process of dielectronic recombination. For $n > 10$ more approximate methods are used, and in particular dielectronic recombination is not included. Two potential sources of error can be identified in this procedure.

First, it has been established (e.g. Kisielius et al. 1998) that the photoionization data deposited in the Opacity Project data base, which was used by Storey (1994) in the calculation of O II recombination coefficients, was in some cases, calculated on a rather coarse grid of energies, opening up the possibility that the resonance contribution to the recombination coefficients could be in error. This was noted by Storey, but he also pointed out that resonance (dielectronic) contributions were only of any great importance for direct recombination to the terms of the ground configuration of O^+. For higher states, such as those arising from the $2p^2 4f$ configuration, resonance contributions are insignificant, and indeed the calculations by Storey for the 3d–4f transition array agree to within 5 per cent with the less elaborate calculations of Pequignot et al. (1991), and indeed with a simple hydrogenic model (Storey & Hummer 1995). In addition, in the work of Davey et al. (1999) on C^+, the problem of insufficient resolution of resonance features was overcome by new R-matrix calculations of the photoionization cross-sections using a mesh carefully designed to resolve all relevant resonance features. The total recombination coefficients to the 4f state of C^+ obtained from this new calculation is in agreement with those for O^+ from Storey (1994) and LSBC to within 3 per cent. We believe therefore that for transitions between states of relatively high orbital angular momentum ($l \geq 3$) in O^+, C^+ and Ne^+ the direct recombination coefficients are certainly in error by less than 10 per cent and probably by much less than that. For states of lower l, and particularly for states of low n and l, uncertainties are likely to be greater. Low-lying states often interact strongly with other states belonging to the ground complex. The interaction of the $2s2p^2$ and $2s^2 3d\ ^2D$ states in C^+ is an example. Such interactions are inevitably not modelled exactly by the R-matrix approach, and *f*-values and photoionization cross-sections may be in error as a result. The resulting uncertainties could be large enough to explain the difference in the O^{2+}/H^+ ratio derived from the 3s–3p and 3d–4f transition arrays, for example. However, the fact that a similar discrepancy of a similar magnitude is seen in the Ne^{2+}/H^+ ratio suggests that errors in the recombination coefficients are not the explanation, since there is no reason to expect systematic errors in the atomic data.

The second potential source of error lies in the exclusion of the effects of dielectronic recombination for states with $n > 10$. It is well known that at sufficiently high electron temperatures, dielectronic recombination to states of high principal quantum

number becomes the dominant recombination mechanism. For once-ionized species of light elements, temperatures of 20 000 K or higher are needed for this process to become effective, and consequently it has been neglected in all calculations of recombination line intensities carried out for nebular plasmas. High-temperature dielectronic recombination causes a local maximum in the recombination coefficient at temperatures for which mean free electron energies are a significant fraction of the excitation energies of the ion resonance lines. For once-ionized C, N, O and Ne, temperatures of $(2\text{–}5)\times10^4$ K are required. The effect of high-temperature dielectronic recombination is to populate high Rydberg states of the recombined ion, and unlike low-temperature dielectronic recombination, the resulting cascade processes strongly enhance the populations of states of the principal series of the ion. The process can therefore increase the recombination coefficient of an ionic line relative to that of a hydrogen line. This opens up the possibility of a nebular model in which pockets of gas which are much hotter than the measured mean temperature of the nebula are responsible for the strong emission in the heavy-element recombination lines, while hydrogen emission would come predominantly from the cooler background gas. Such regions would also be strong emitters of high-excitation CELs, leading to the CEL temperature being higher than measured by other means. This is exactly what is observed, but a detailed evaluation of such a model cannot be made at present, since no calculations of line recombination coefficients have yet been made which correctly and fully incorporate high-temperature dielectronic recombination.

The question of recombination excitation of the [O II] auroral lines $\lambda\lambda$7320, 7330 has been discussed in Section 3.3. Using the new recombination coefficients described in Appendix A and the O^{2+}/H^+ abundance derived from permitted O II recombination lines, we find good agreement between the observed and expected intensities of these lines. We note that this good agreement is not found if the earlier radiative recombination data of Pequignot et al. (1991) are combined with the dielectronic recombination coefficients of Nussbaumer & Storey (1984). Using those recombination coefficients, the predicted intensity of these lines from recombination alone exceeds the observed intensity by 70 per cent.

5.2 Temperature fluctuations

Given the exponential sensitivity to T_e of the ionic abundances derived from UV or optical CELs, the large discrepancies between heavy-element abundances derived from ORLs on the one hand, and from UV and optical CELs on the other, have generally been interpreted as being caused by the presence of large temperature fluctuations (cf. Peimbert 1994 for a recent review). The concept of significant temperature fluctuations and their effects on abundance determinations was first explored by Peimbert (1967). As an example, in traditional nebular abundance analyses the O^{2+}/H^+ abundance is derived from the $(\lambda4959+\lambda5007)/H\beta$ intensity ratio, using the electron temperature derived from the [O III] $(\lambda4959+\lambda5007)/\lambda4363$ ratio (e.g. Osterbrock 1989). However, in a thermally inhomogeneous nebula, because of the much higher E_{ex} of the λ4363 line (62 000 K) compared to that of the $\lambda\lambda$4959, 5007 lines (29 000 K), the emission of the λ4363 line is much more strongly biased towards the warmer regions than the $\lambda\lambda$4959, 5007 lines. As a result, the electron temperature derived from their ratio overestimates the average temperature of the $\lambda\lambda$4959, 5007 emission region, leading to an overestimated emissivity for the latter two lines. This error is further augmented by the application of the same [O III] temperature to Hβ, resulting an underestimated average Hβ emissivity because of the decrease of the Hβ emissivity with increasing T_e. The combined effect of the errors leads to a grossly underestimated O^{2+}/H^+ abundance ratio. For ionic abundances derived from the intensity of a recombination line relative to Hβ, the result is proportional to $\alpha_{eff}(H\beta)/\alpha_{eff}(\lambda)\propto T_e^{\beta}$, where α_{eff} are the effective recombination coefficients. In general, $|\beta|\ll1$, and the abundances derived from ORLs are essentially independent of the adopted temperature and the presence of temperature fluctuations.

To characterize temperature fluctuations and their effects on forbidden-line abundance determination, Peimbert (1967) introduced the concepts of the mean ionic temperature T_0 and the temperature fluctuation parameter t^2, which for a given ion species X^{i+} can be defined as

$$T_0(X^{i+})=\frac{\int T_e N_e N(X^{i+})\,dV}{\int N_e N(X^{i+})\,dV}, \tag{4}$$

$$t^2(X^{i+})\equiv\frac{\int (T_e-T_0)^2 N_e N(X^{i+})\,dV}{T_0^2\int N_e N(X^{i+})\,dV}. \tag{5}$$

The observed flux from a line emitted by ion stage X^{i+} is given by

$$I(X^{i+},\lambda)=\int N_e N(X^{i+})\epsilon(T_e)\,dV, \tag{6}$$

where $\epsilon(T_e)$ is the line emissivity. $\epsilon(T_e)$ can be expanded in a Taylor series about a mean temperature T_0. If the temperature variation over the volume considered in the integral above is relatively small, then we can truncate this series and retain only terms up to second order:

$$\epsilon(T_e)=\epsilon(T_0)+\epsilon'(T_e-T_0)+\frac{\epsilon''}{2}(T_e-T_0)^2. \tag{7}$$

Then

$$I(X^{i+},\lambda)=\int\left[\epsilon(T_0)+\frac{T_0^2\epsilon''(T_0)}{2}t^2\right]N_e N(X^{i+})\,dV. \tag{8}$$

Equation (8) can be used to calculate the average temperature $T(\lambda)$ of the emitting region of a given line λ. For a CEL with critical density $N_{crit}(\lambda)\gg N_e$ (which is usually true for UV and optical CELs under typical nebular conditions), collisional de-excitation can be neglected and we have

$$\epsilon(\lambda)\propto T_e^{-1/2}\exp(-\Delta E/kT_e), \tag{9}$$

$$T_e^{-1/2}(\lambda)\exp\left[\frac{-\Delta E}{kT_e(\lambda)}\right]=T_0^{-1/2}\exp\left(\frac{-\Delta E}{kT_0}\right)\times\left\{1+\left[\left(\frac{\Delta E}{kT_0}\right)^2-\frac{3\Delta E}{kT_0}+\frac{3}{4}\right]\frac{t^2}{2}\right). \tag{10}$$

For the [O III] $\lambda\lambda$4959, 5007 lines, $\Delta E=28\,800$ K.

The emissivity of an ORL is proportional to its effective recombination coefficient α_{eff}. For lines dominated by radiative recombination, α_{eff} can be fitted (e.g. Péquignot et al. 1991) by

$$\alpha_{eff}=10^{-13}Z\frac{AT_4^B}{1+CT_4^D}\ \mathrm{cm^3\,s^{-1}},\quad T_4\equiv\frac{T_e}{10^4Z^2}.$$

Thus we have

$$\frac{T_e^{-\alpha}(\lambda)}{1+\gamma T_e^{\beta}(\lambda)} = \frac{T_0^{-\alpha}}{1+\gamma T_0^{\beta}} + \frac{t^2}{2}(1+\gamma T_0^{\beta})^{-3} \times [\alpha(\alpha+1)T_0^{-\alpha} + (\alpha+\beta)(\alpha+\beta+1)\gamma^2 T_0^{2\beta-\alpha} + (2\alpha^2+2\alpha+2\alpha\beta-\beta^2+\beta)\gamma T_0^{\beta-\alpha}], \quad (11)$$

where

$$\alpha = -B, \quad \beta = D, \quad \gamma = CZ^{-2D}10^{-4D}.$$

For case B Hβ recombination, $Z = 1$, $A = 0.668$, $B = -0.507$, $C = 1.221$ and $D = 0.653$.

Peimbert (1971) measured the nebular continuum Balmer jump temperatures in three PNe and for several regions of the Orion nebula, and found them to be systematically lower than the [O III] temperatures. He interpreted the result as indicating the presence of temperature fluctuations. The [O III] and Balmer jump temperatures are given by (Peimbert 1967)

$$T_e([\mathrm{O\,III}]_{na}) = T_0(O^{2+})\left\{1+\frac{1}{2}\left[\frac{91380}{T_0(O^{2+})}-3\right]t^2(O^{2+})\right\}, \quad (12)$$

$$T_e(\mathrm{BJ}) = T_0(H^+)[1-1.67t^2(H^+)]. \quad (13)$$

Thus, if $T_0(O^{2+}) = T_0(H^+)$ and $t^2(O^{2+}) = t^2(H^+)$, the values of T_0 and t^2 can be derived by measuring $T_e([\mathrm{O\,III}]_{na})$ and $T_e(\mathrm{BJ})$. For example, Peimbert (1971) found $t^2 \approx 0.04$ for the nebulae he observed. That $T_e(\mathrm{BJ})$ tends to be lower than $T_e([\mathrm{O\,III}]_{na})$ for the same nebula is supported by recent measurements of $T_e(\mathrm{BJ})$ in a number of PNe by Liu & Danziger (1993b). They found that on average $t^2 \approx 0.03$. On the other hand, deep spectroscopic observations (Liu et al. 1995b) disproved claims by Walter & Dufour (1994) of very low Balmer jump temperatures in the Orion nebula, and showed excellent agreement between Balmer jump and [O III] forbidden-line temperatures.

The large temperature fluctuations suggested by $T_e(\mathrm{BJ})$ measurements of PNe are not predicted by photoionization models. Several mechanisms capable of producing large temperature fluctuations have been proposed, such as extra heating from shocks, density fluctuations and chemical abundance gradients, but direct observational evidence to support these suggestions has yet to be found (cf. Section 1 for references). In addition, the assumption that $T_0(O^{2+}) = T_0(H^+)$ and $t^2(O^{2+}) = t^2(H^+)$, required to derive T_0 and t^2 from equations (12) and (13), have been shown to be invalid by photoionization modeling in most cases (Kingdon & Ferland 1995b). In a typical photoionized nebula, H^+ is present in the whole ionized region while, depending on the nebular ionization structure, O^{2+} exists only in a limited zone. Thus, in general, $T_0(O^{2+}) \neq T_0(H^+)$ and $t^2(O^{2+}) \lesssim t^2(H^+)$. On the other hand, the large-scale temperature variations predicted by photoionization models, caused by changes in the ionization and thermal equilibrium as a function of nebular radius, are not fluctuations which, in the strict sense, refer only to localized, small-scale thermal inhomogeneities, caused by, say, shock waves or density condensations. Nebular models that deal with such localized inhomogeneities are not yet available.

An alternative method to estimate values of t^2 in PNe avoids the above-mentioned complications by using two T_e diagnostics from the same ion species, as has been proposed by Dinerstein et al. (1985). By comparing electron temperatures derived from the [O III] λ5007/λ4363 ratio with those from the λ5007/52 μm ratio, for several PNe, they derived t^2 values between 0.04 and 0.06. A reanalysis of the data for NGC 6543 by Dinerstein et al. (1995), however, contradicts the earlier results of Dinerstein et al. (1985) by finding no evidence for temperature fluctuations. A potential difficulty in using this method to estimate the t^2 parameter is the relatively low N_{crit} of the [O III] 52-μm line, $N_{crit} = 3400\,\mathrm{cm}^{-3}$. As a result, the electron temperature derived from the λ5007/52 μm ratio is sensitive to the adopted N_e and to the presence of density inhomogeneities (cf. Table 6, Section 3.2). A recent study by Liu (1997) of a large sample of PNe observed with the *ISO* LWS has shown that the electron densities derived from the [O III] 52 μm/88 μm ratio are systematically lower than those derived from the optical [Ar IV] and [Cl III] doublet ratios, which have higher critical densities, indicating the presence of moderate density inhomogeneities in the nebulae. The same result is apparent here for NGC 6153 (Section 3.2). Probably a better approach would be to estimate t^2 by comparing the electron temperatures given by the [Ne III] λ3868/λ3342 and λ3868/15.5-μm ratios, since the 15.5-μm line has a much higher critical density, $2.0\times10^5\,\mathrm{cm}^{-3}$. The [Ne III] 3342.42-Å line is unfortunately lost in the nearby strong O III Bowen fluorescence line at 3340.74 Å in our spectra. Deep spectroscopy, of much higher resolution than obtained here, is needed to detect this line.

5.3 Temperature fluctuations as the cause of abundance discrepancies

Fig. 14 shows that the electron temperature derived from the [O III] nebular to auroral line ratio varies by $\sim$1200 K along the nebular minor axis and is more than 2000 K higher than the Balmer jump temperature, which is constant across the nebula, suggesting the presence of temperature fluctuations in NGC 6153. Consistent with this, the temperature derived from the [O III] optical nebular to auroral line ratio is higher than that deduced from the ratio of the optical nebular lines to the far-IR fine-structure lines (cf. Table 6). On the other hand, the temperature yielded by the [Ne III] (λ3868 + λ3967)/15.5-μm ratio agrees reasonably well with that deduced from the [O III] nebular to auroral line ratio. In the remainder of this section, we examine the possibility that the factor of 10 discrepancy between the heavy-element abundances derived for NGC 6153 from ORLs and from CELs can be explained by assuming large temperature fluctuations, without identifying their physical causes.

We assume that $T_0(O^{2+}) = T_0(H^+)$, $t^2(O^{2+}) = t^2(H^+)$, and that the Balmer jump temperature has a constant value of $T_e(\mathrm{BJ}) = 6080$ K. Then, taking $T_e([\mathrm{O\,III}]_{na})$ to have the minimum and maximum measured values of 8200 and 9400 K, we obtain from equations (12) and (13) $T_0 = 6580$ K, $t^2 = 0.045$ and $T_0 = 6900$ K, $t^2 = 0.071$ respectively.

For $T_0 = 6580$ K and $t^2 = 0.045$, equations (11) and (10) yield average line-emitting temperatures of $T_e(\lambda\lambda4959, 5007) = 6830$ K and $T_e(\mathrm{H}\beta) = 6340$ K, which when used to calculate the average emissivities of the [O III] $\lambda\lambda$4959, 5007 lines and Hβ, respectively, yield an O^{2+}/H^+ ionic abundance ratio that is 2.4 times higher than the value that would be obtained if $T_e([\mathrm{O\,III}]_{na}) = 8200$ K were to used to calculate the emissivities of all lines. Similarly, for $T_0 = 6900$ K and $t^2 = 0.071$, one finds that $T_e(\lambda\lambda4959, 5007) = 7260$ K and $T_e(\mathrm{H}\beta) = 6500$ K, and that the O^{2+}/H^+ ionic abundance would be 3.1 times higher than if $T_e([\mathrm{O\,III}]_{na}) = 9400$ K were to be used for all lines. Thus the temperature fluctuations derived from the measured [O III] and

Balmer jump temperatures are too small to account for the observed discrepancy of a factor of 9.3 between O^{2+}/H^+ abundances derived from the O II recombination lines and from the $\lambda\lambda$4959, 5007 lines.

There are, however, more fundamental difficulties with the interpretation of temperature fluctuations as the cause of the discrepant ionic abundances derived from the two types of emission lines. Our results in Fig. 11 show that for C^{2+}/H^+, N^{2+}/H^+, O^{2+}/H^+ and Ne^{2+}/H^+, in all cases where ionic abundances have been derived using both ORLs and UV or optical CELs, the abundances derived from the ORLs are all approximately a factor of 10 higher than the corresponding values deduced from the CELs, regardless of the excitation energies of the CELs. If temperature fluctuations are responsible for the discrepancies, we would expect the ratios to be correlated with E_{ex} (cf. equation 10). For example, for the parameters $T_0 = 6580$ K and $t^2 = 0.045$ above, $T_e(\lambda1908) = 7360$ K is obtained, and temperature fluctuations will cause the C^{2+}/H^+ ratio derived from $I(\lambda1908)/I(H\beta)$ ($\Delta E = 75\,500$ K) to be underestimated by a factor of 3.4, as compared to a factor of 2.4 for the O^{2+}/H^+ ratio derived from $I(\lambda4959 + \lambda5007)/I(H\beta)$ ($\Delta E = 28\,800$ K). For $T_0 = 6900$ K and t^2=0.071, $T_e(\lambda1908) = 7980$ K, and temperature fluctuations will cause the C^{2+}/H^+ ratio to be underestimated by a factor of 5.2 as compared to a factor of 3.1 for O^{2+}/H^+. In both cases, the predicted effect of temperature fluctuations on the derived C^{2+}/H^+ ratio is approximately a factor of 1.5 larger than for the O^{2+}/H^+ ratio. Yet the ratio of the C^{2+}/H^+ abundance derived from ORLs to that deduced from the collisionally excited λ1908 line is 9.0, very similar to the ratio of 9.3 found in the case of O^{2+}/H^+.

Fig. 17(a) shows that when the electron temperature mapped by the [O III] λ4959/λ4363 line ratio along the nebular minor axis is used together with the λ4959 surface brightness distribution to derive the O^{2+}/H^+ abundance ratio, the implied O/H abundance increases outwards from the nebular centre. This result is difficult to understand in the context of stellar evolution, and casts strong doubt on the reliability of T_e derived from the [O III] nebular to auroral line ratio. Could the abundance discrepancies be explained by discarding the [O III] temperature and adopting only the temperature of 6080 K given by the nebular continuum Balmer discontinuity? For a constant T_e of 6080 K, the observed [O III] $\lambda\lambda$4959, 5007 fluxes from NGC 6153 yield $O^{2+}/H^+ = 2.63 \times 10^{-3}$, two-thirds of the value given by the O II recombination lines (cf. also Fig. 17b). However, for this temperature to reproduce the observed intensities of the C III] λ1908 line and the N III] λ1751 line by collisional excitation alone would require C^{2+}/H^+ and N^{2+}/H^+ abundances of 0.017 and 0.056 respectively, 8 and 32 times higher even than the high abundance values given by the ORLs. This discrepancy can be reduced, at least for C^{2+}/H^+, if recombination excitation of C III] λ1908 is included, using the C^{3+}/H^+ abundance derived from ORLs given in Table 18 and recombination coefficients from Péquignot et al. (1991) and Nussbaumer & Storey (1984). The C^{2+}/H^+ abundance ratio required to reproduce the observed C III] λ1908 flux is then 0.007, a factor of 2.7 larger than that obtained from the C II recombination lines. Lower abundances can be obtained from these UV collisionally excited lines by adopting the Balmer jump temperature, but at the same time assuming some temperature fluctuations. For example, we find that for $T_e(BJ) = 6080$ K and $t^2 = 0.044$, equations (12) and (13) yield $T_0 = 6560$ K and $T_e([O\,III]_{na}) = 8140$ K. In return, equations (11) and (10) give $T_e(H\beta) = 6330$ K and $T_e(\lambda1908) = 7340$ K, which when combined with the observed λ1908 line flux yields $C^{2+}/H^+ = 2.22 \times 10^{-3}$, the same as derived from the C II recombination lines. However, the same temperature fluctuation parameters predict [O III] $\lambda\lambda$4959, 5007 and [Ne III] $\lambda\lambda$3868, 3967 line temperatures of 6810 and 6970 K, leading to $O^{2+}/H^+ = 1.60 \times 10^{-3}$ and $Ne^{2+}/H^+ = 5.82 \times 10^{-4}$ from the corresponding lines, approximately a factor of 2.7 lower than the values given by the ORLs. Smaller values of t^2 improve the agreement between O^{2+}/H^+ and Ne^{2+}/H^+ abundances derived from optical CELs and from ORLs, but make it worse for C^{2+}/H^+. Again, temperature fluctuations fail to provide a consistent explanation for all the observed lines.

The most serious difficulty for the temperature fluctuation scenario comes, however, from observations of the IR fine-structure lines, such as [Ne III] 15.5-μm, [N III] 57-μm and [O III] 52- and 88-μm, which all yield abundances similar to those given by the relevant UV and optical CELs (cf Section 3.6). Similarly, recent KAO measurement of the [O III] 52 and 88-μm lines from NGC 7009 by Rubin et al. (1997) yielded an O^{2+}/H^+ abundance ratio which is only 20 per cent higher than the value given by the $\lambda\lambda$4959, 5007 lines, and a factor of 3.8 lower than derived from O II recombination lines by LSBC. The excitation energies of these two IR fine-structure lines are well under 1000 K, much smaller than the nebular electron temperature, so their emissivities are essentially independent of the nebular thermal structure. However, these lines also have relatively low critical densities, so ionic abundances derived from them are sensitive to the adopted N_e and can thus be subject to the presence of density inhomogeneities, the subject of the next subsection.

5.4 Density inhomogeneities

For NGC 6153, the electron density derived from the low critical density [O III] 52- and 88-μm lines is about a factor of 2 lower than derived from the optical [Ar IV] and [Cl III] doublets, which have much higher critical densities. Given that all of these lines should arise from similar ionization zones, this result suggests the presence of density inhomogeneities within NGC 6153. Similar results are found for a large sample of PNe observed with the *ISO* LWS (Liu 1997), where the densities derived from the 88 μm/52 μm ratio are found to be systematically lower than given by the [Ar IV] and [Cl III] doublet ratios for the same nebula. Fig. 15 shows that the average line-of-sight electron density for NGC 6153 varies by a factor of 2 along the minor axis. The ionic abundances derived from the 57-μm [N III] and 52-, 88-μm [O III] lines for $N_e = 3500\,cm^{-3}$, the average density given by the [Ar IV] and [Cl III] doublet ratios, are about a factor of 1.7–1.8 higher than those deduced using $N_e = 1660\,cm^{-3}$ as given by the 52 to 88-μm line ratio (Table 8), but still a factor of 4–5 lower than those derived from the ORLs. The difference between the Ne^{2+}/H^+ values derived from the 15.5-μm line using these two densities is negligible.

Apart from the large-scale variations in the density distribution along the nebular minor axis (Fig. 15), density inhomogeneities can also take the form of small high-density clumps embedded in material of much lower density. Such high-density clumps may escape detection because of the limited spatial resolution of existing long-slit spectroscopy and the smoothing effect along the line of sight. Viegas & Clegg (1994) showed that condensations with $N_e \gtrsim 10^6\,cm^{-3}$ can have a significant effect on the [O III] $(\lambda4959 + \lambda5007)/\lambda4363$ ratio, via collisional quenching of the $\lambda\lambda$4959, 5007 lines, which have $N_{crit} = 6.9 \times 10^5\,cm^{-3}$. The

λ4363 line would be hardly affected by such condensations because of its much higher critical density, $2.5\times10^7\,\mathrm{cm}^{-3}$. Such high-density condensations would lead to apparently higher [O III] temperatures compared to those derived from nebular continuum Balmer discontinuities, as observed in some PNe (Liu & Danziger 1993b). Below we discuss in some detail the constraints our observations impose on such models and their implications for abundances derived from CELs, in particular those derived from IR fine-structure lines, which generally have lower critical densities than lines in the optical and UV.

In a simplified nebular model consisting of only two density components, the amount of nebular gas in the high-density component can be estimated using the observed ratio of the [O III] 52 and 88-μm lines ($N_{\rm crit}=3500$ and $500\,\mathrm{cm}^{-3}$ respectively) and either the [Cl III] $\lambda\lambda$5517, 5537 doublet ratio ($N_{\rm crit}=6400$ and $3.4\times10^4\,\mathrm{cm}^{-3}$ respectively) or the [Ar IV] $\lambda\lambda$4711, 4740 doublet ratio ($N_{\rm crit}=1.4\times10^4$ and $1.3\times10^5\,\mathrm{cm}^{-3}$ respectively). Given their higher $N_{\rm crit}$, the [Cl III] and [Ar IV] lines will be dominated by emission from the high-density regions, where the [O III] IR lines will be suppressed by collisional de-excitation. We assume that the low-density component has an electron density of $N_{\rm e}^{\rm L}$ and the high-density component has a density of $\alpha\times N_{\rm e}^{\rm L}$ and a volume filling factor of f. In this two-component model, the predicted [O III] 88 μm/52 μm ratio is given by

$$\frac{I(88\,\mu\mathrm{m})}{I(52\,\mu\mathrm{m})}=\frac{(1-f)\epsilon(88\,\mu\mathrm{m};N_{\rm e}^{\rm L})+f\alpha\epsilon(88\,\mu\mathrm{m};\alpha N_{\rm e}^{\rm L})}{(1-f)\epsilon(52\,\mu\mathrm{m};N_{\rm e}^{\rm L})+f\alpha\epsilon(52\,\mu\mathrm{m};\alpha N_{\rm e}^{\rm L})}. \qquad (14)$$

Similarly, for the [Cl III] and [Ar IV] doublet ratios, we have

$$\frac{I(\lambda5537)}{I(\lambda5517)}=\frac{(1-f)\epsilon(\lambda5537;N_{\rm e}^{\rm L})+f\alpha\epsilon(\lambda5537;\alpha N_{\rm e}^{\rm L})}{(1-f)\epsilon(\lambda5517;N_{\rm e}^{\rm L})+f\alpha\epsilon(\lambda5517;\alpha N_{\rm e}^{\rm L})}, \qquad (15)$$

$$\frac{I(\lambda4740)}{I(\lambda4711)}=\frac{(1-f)\epsilon(\lambda4740;N_{\rm e}^{\rm L})+f\alpha\epsilon(\lambda4740;\alpha N_{\rm e}^{\rm L})}{(1-f)\epsilon(\lambda4711;N_{\rm e}^{\rm L})+f\alpha\epsilon(\lambda4711;\alpha N_{\rm e}^{\rm L})}. \qquad (16)$$

Here $\epsilon(\lambda;N_{\rm e})$ denotes the emissivity of line λ per ion ($\mathrm{erg\,s}^{-1}$) at a given density $N_{\rm e}$ (and temperature $T_{\rm e}$). For NGC 6153, the observed ratios are $I(88\,\mu\mathrm{m})/I(52\,\mu\mathrm{m})=0.278$, $I(\lambda5537)/I(\lambda5517)=1.27$ and $I(\lambda4740)/I(\lambda4711)=0.927$ (cf. Tables 2 and 3).

For a given density contrast α, $N_{\rm e}^{\rm L}$ and f can be derived by solving equations (14) and (15) or equations (14) and (16). For $\alpha=10$, two solutions are possible for equations (14) and (15): (1) $N_{\rm e}^{\rm L}=375\,\mathrm{cm}^{-3}$ and $f=0.0921$; and (2) $N_{\rm e}^{\rm L}=453\,\mathrm{cm}^{-3}$ and $f=0.0759$. For the first solution the [N III] 57-μm and the [O III] 52- and 88-μm line fluxes yield $\mathrm{N}^{2+}/\mathrm{H}^+=2.81\times10^{-4}$ and $\mathrm{O}^{2+}/\mathrm{H}^+=8.22\times10^{-4}$. Similarly, for the second solution we have $\mathrm{N}^{2+}/\mathrm{H}^+=3.06\times10^{-4}$ and $\mathrm{O}^{2+}/\mathrm{H}^+=8.94\times10^{-4}$. These values are higher than those derived assuming a constant $N_{\rm e}$ of $1660\,\mathrm{cm}^{-3}$, but lower than those deduced for a constant $N_{\rm e}$ of $3500\,\mathrm{cm}^{-3}$. In both cases, the effects of density inhomogeneities on the [O III] temperature and on the $\mathrm{Ne}^{2+}/\mathrm{H}^+$ ratio derived from the 15.5-μm line are negligible.

For a much higher density contrast $\alpha=1000$, equations (14) and (15) yield $N_{\rm e}^{\rm L}=1614\,\mathrm{cm}^{-3}$ and $f=7.29\times10^{-6}$. It is interesting to note that for this particular solution, in spite of their small filling factor, the high-density condensations actually contribute about 7.3 times more to the emitted Hβ flux than the lower density component. Such a density structure however yields an [Ar IV] $\lambda4740/\lambda4711$ ratio of 2.1, twice as high as the observed value. A much tighter constraint on the amount of gas that can be present in high-density condensations can be obtained by combining equations (14) and (16), given the advantage of even higher critical densities of the [Ar IV] doublet lines than of the [Cl III] doublet. With $\alpha=1000$ we find $N_{\rm e}^{\rm L}=1640\,\mathrm{cm}^{-3}$ and $f=3.44\times10^{-7}$. In this case, the high-density condensations contribute only 26 per cent of the Hβ emission from the whole nebula. Ar^{2+} has an ionization potential of 40.74 eV, compared to 23.81 and 35.12 eV for Cl^+ and O^+ respectively. It is possible that because of the reduced ionization degree within the condensations (because their higher densities will enhance the recombination rates, proportional to density squared, over photoionization rates, proportional to density), there is little Ar^{3+} within the high-density condensations. Given this possibility, we discuss the consequences of high-density condensations on the derived nebular temperature and ionic abundances for both solutions.

For Case 1, with $\alpha=1000$, $N_{\rm e}^{\rm L}=1614\,\mathrm{cm}^{-3}$ and $f=7.29\times10^{-6}$, the observed [O III] $(\lambda4959+\lambda5007)/\lambda4363$ ratio of 284 can be reproduced by an electron temperature of $T_{\rm e}=6030$ K, which is nearly identical to the Balmer jump temperature. For Case 2, where $\alpha=1000$, $N_{\rm e}^{\rm L}=1640\,\mathrm{cm}^{-3}$ and $f=3.44\times10^{-7}$, the $(\lambda4959+\lambda5007)/\lambda4363$ ratio yields $T_{\rm e}=7980$ K. The ionic abundances derived from various CELs, for both cases, are tabulated in Table 20, where the excitation energies and critical densities of these lines are also listed. For the IR fine-structure lines the derived abundances are directly affected by the density inhomogeneities, whereas for the optical and UV lines they are affected mainly via the reduced $T_{\rm e}$([O III]) inferred after taking into account collisional quenching of the $\lambda\lambda$4959, 5007 lines within high-density condensations.

Comparison of the abundances given in Table 20 with those given in Table 8, which were derived from the same set of CELs but assuming no density inhomogeneities, and with the ORL abundances given in Table 18, shows that for Case 1, the IR fine-structure $\mathrm{O}^{2+}/\mathrm{H}^+$, $\mathrm{N}^{2+}/\mathrm{H}^+$ and $\mathrm{Ne}^{2+}/\mathrm{H}^+$ abundances all show a significant increase and become compatible, within a factor of 2, with the corresponding ORL abundances. So also do the $\mathrm{O}^{2+}/\mathrm{H}^+$ and $\mathrm{Ne}^{2+}/\mathrm{H}^+$ ratios derived from their optical CELs. However, the $\mathrm{C}^{2+}/\mathrm{H}^+$ and $\mathrm{N}^{2+}/\mathrm{H}^+$ ratios derived from the UV collisional lines become so large such that they are respectively factors of 9 and 37 higher than even those derived from C II and N II recombination lines. For Case 2, the abundances derived from the IR fine-structure lines show an enhancement of about a factor of 1.5 compared to the values derived in Table 8, and about a factor of 2 enhancement for the optical CELs. The enhancements for the two UV lines are again the largest, by about a factor of 3–4. Thus for Case 2, the effects of the high-density condensations are not large enough to bring the CEL abundances into agreement with the ORL abundances.

The above examples show that density fluctuations, like temperature fluctuations discussed earlier, fail to provide a consistent interpretation of the abundance discrepancies for all CELs observed from NGC 6153. Both scenarios require the discrepancies to be correlated with the excitation energies and/or the critical densities of the CELs, which is in contradiction with the observations.

We showed in Section 3.2 that high-order Balmer lines provide a sensitive diagnostic to determine nebular densities (cf. Fig. 10). The diagnostic is particularly useful for probing ionized high-density regions. In Fig. 20 we compare the intensities of the high-order Balmer lines predicted by the two-density-component models of Cases 1 and 2 with those observed in NGC 6153. For both cases, the predicted intensities are much higher than observed. The comparison shown in Fig. 20 rules out the

Table 20. Effects of high-density condensations[a].

Quantity	Lines	E_{ex} (K)	N_{crit} (cm^{-3})	Case 1[b]	Case 2[c]
T_e([O III])				6030 K	7980 K
C^{2+}/H^+	1908	7.5(4)	≤9(8)	2.1(−2)	8.5(−4)
N^{2+}/H^+	57 μm	250	1500	2.2(−3)	2.8(−4)
	1751	8.2(4)	≤11(9)	6.3(−2)	2.0(−3)
O^{2+}/H^+	52,88 μm	≤603	≤3500	6.3(−3)	8.4(−4)
	4959,5007	2.9(4)	6.9(5)	7.8(−3)	9.1(−4)
Ne^{2+}/H^+	15.5 μm	930	2(5)	1.2(−3)	2.4(−4)
	3868,3967	3.7(4)	9.6(6)	1.4(−3)	2.7(−4)

[a] The numbers in parentheses are powers of 10, thus 7.5(4) represents 7.5×10^4;
[b] $\alpha = 1000$, $\log N_e^L = 3.208\,cm^{-3}$ and $f = 7.29 \times 10^{-6}$;
[c] $\alpha = 1000$, $\log N_e^L = 3.215\,cm^{-3}$ and $f = 3.44 \times 10^{-7}$.

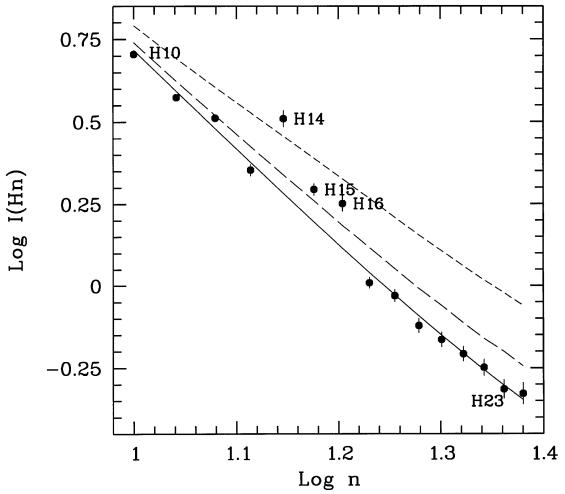

Figure 20. Predicted intensities (in units where $H\beta = 100$) of high-order Balmer lines ($n \rightarrow 2$, $n = 10, 11, \ldots, 24$) for Case 1 ($\alpha = 1000$, $N_e^L = 1614\,cm^{-3}$ and $f = 7.29 \times 10^{-6}$; short-dashed line) and Case 2 ($\alpha = 1000$, $N_e^L = 1640\,cm^{-3}$ and $f = 3.44 \times 10^{-7}$; long-dashed lines) of the two-density-component models. The solid circles are observed values, whereas the solid curve shows the best fit for a homogeneous nebula, which yields $N_e = 2000\,cm^{-3}$ (cf. Section 3.2 and Fig. 10).

possibility of explaining the abundance determination discrepancy in NGC 6153 by invoking high-density condensations, unless the condensations are also H-deficient. In the next section we discuss some such composite models, incorporating density and temperature fluctuations as well as chemical abundance inhomogeneities.

5.5 Empirical composite models

The standard techniques for determining electron temperatures and densities from ratios of the intensities of CELs tacitly assume that the intensities of such lines depend only upon the number density of the atomic ion in question. It is apparent from the discussion of [O II] auroral lines λλ7320, 7330 in Section 3.3 above that at the temperatures implied by the magnitude of the Balmer discontinuity in NGC 6153 this is no longer a good approximation for many of the forbidden lines. To rigorously use these lines as diagnostics we need to consider the relative populations of all the ions of the element in question. We describe a simple empirical model of this sort here.

We consider a selection of permitted recombination lines, forbidden lines, IR lines and UV intersystem lines chosen to provide information about temperature, density and abundances. A list of the lines selected is given in Table 22. It is not exhaustive. For some elements (H, He, Ne, Ar) we include lines arising from only one ionization stage, but for oxygen and carbon we include the ionization stages necessary to allow for the effects of recombination on the important lines. For example, the intensity of C II λ 4267 depends on the C^{2+} abundance, while the intensity of λ1909 depends on the abundances of both C^{2+} and C^{3+}. Once a physical model of the nebula has been specified, perhaps by a temperature, a density and the abundances of the ionization stages of the elements, the predicted intensities of all the lines in Table 22 [taken relative to $I(\beta) = 100$] can be compared to the observed values, and this can be used as the basis of an optimization procedure to determine the best values of the physical parameters. The line intensities given in Table 22 are those measured for the whole nebula, except for the high Balmer lines, where the high-resolution data taken along the minor axis are used. In practice, we minimize the sum of the squares of the fractional differences between prediction and observation for all lines except H11–H24. The lines H14, H15 and H16 are omitted from the sum because of serious blending problems, and the remaining 11 Balmer lines are given equal weight and a combined weight of unity in the optimization procedure. The optimal value of the sum for each of the empirical models is given in Table 21, where it is referred to as χ^2. An optimization procedure of this kind can be used to give an indication of the kind of physical conditions that might be necessary to explain the observed fluxes. Since no consistent model of the nebular physics is involved, the optimization might lead to solutions that are physically unrealistic. In this section we present the results of the optimization procedures, and in the next section we attempt to relate these results to possible physical realities.

As we discussed in Section 3.6, Fig. 11 and Tables 8 and 18 show that for a given element, ORLs and CELs both yield the same *relative* ionic concentrations for individual ionization stages of different elements. We therefore adopt throughout the relative abundance fractions from Tables 8 and 18, with the ICF corrections as discussed in Section 3.7. Thus for oxygen we have $O^+/O = 0.05$, $O^{2+}/O = 0.90$ and $O^{3+}/O = 0.05$, while for carbon we assume $C/O = 0.55$, $C^{3+}/C = 0.051$ and $C^{2+}/C = 0.90$. We also adopt $Ne^{2+}/O = 0.35$ and $Ar^{3+}/O = 0.0012$ for all models.

If we model the emission by assuming a homogeneous nebula of a uniform electron temperature and density, and treat these two quantities and the O/H and He/H ratios as free parameters, we obtain the line intensities labelled H1 in Table 22. The resultant model parameters are listed in Table 21. The best-fitting electron

Table 21. Parameters of empirical models.

Parameter	H1	H2	IH1	IH2	IH3
Component 1					
N_e (cm^{-3})	2400	2370	5750	5460	1370
T_e (K)	8630	7112	9550	9484	8913
$\sigma_{\log T_e}$	0	0.172	0	0	0
$10^4 \times$ O/H	6.40	8.98	1.13	4.09	5.01
He/H	0.124	0.120	0.107	0.100	0.100
filling factor	1.0	1.0	0.032	0.692	1.000
frac(O)[a]	1.0	1.0	0.181	0.185	0.997
Component 2					
N_e (cm^{-3})	–	–	857	663	2.15×10^6
T_e (K)	–	–	2608	510	4716
$10^4 \times$ O/H	–	–	as C.1	492	392
He/H	–	–	as C.1	0.440	0.334
filling factor	–	–	0.968	0.308	3.43×10^{-8}
χ^2 [b]	3.30	2.78	2.21	0.174	0.439

[a] Fraction of the total number of oxygen atoms in Component 1;
[b] Goodness-of-fit measure; see text for definition.

Table 22. Comparison of observed line intensities with those from empirical models.

Line	λ(Å)	$I(\lambda)$	H1	H2	IH1	IH2	IH3
H 11	3770.6	3.75	3.96	3.93	3.84	3.96	4.11
H 12	3750.1	3.25	3.05	3.02	2.97	3.06	3.19
H 13	3734.3	2.26	2.40	2.38	2.34	2.41	2.54
H 17	3697.1	1.02	1.10	1.09	1.09	1.12	1.20
H 18	3691.5	0.93	0.93	0.94	0.93	0.96	1.02
H 19	3686.8	0.76	0.80	0.81	0.80	0.83	0.89
H 20	3682.8	0.69	0.70	0.71	0.70	0.73	0.77
H 21	3679.5	0.62	0.62	0.63	0.62	0.64	0.68
H 22	3676.3	0.56	0.55	0.56	0.55	0.58	0.61
H 23	3673.7	0.49	0.49	0.51	0.50	0.52	0.54
H 24	3671.2	0.47	0.44	0.46	0.45	0.47	0.49
BJ/Hβ[a]	3646	0.60	0.48	0.58	0.89	0.60	0.50
He I	4471.5	6.43	6.38	6.26	5.90	6.03	6.34
He I	5875.7	18.7	18.0	18.0	18.3	18.4	18.0
He I	6678.2	4.80[b]	5.03	5.09	5.18	5.07	5.07
C II	4267.2	2.40	0.37	0.55	0.75	2.58	2.59
C III]	1908	46.2	31.7	51.3	47.0	44.4	39.2
[O II]	3726.0	17.8[c]	20.1	18.8	17.8	19.1	18.0
[O II]	3728.8	9.53[c]	12.4	11.2	8.61	9.30	12.9
O II	4089.3	0.59	0.07	0.11	0.15	0.52	0.53
[O II]	7320.0	1.74	0.98	1.09	1.50	1.63	1.74
[O II]	7339.7	1.56	0.78	0.88	1.20	1.31	1.37
[O III]	4363.2	4.16	3.60	4.45	4.72	4.58	3.46
[O III]	5006.8	887.	928.	767.	823.	812.	790.
[O III]	52 μm	266.	211.	254.	269.	255.	204.
[O III]	88 μm	74.	47.1	55.3	73.4	75.2	62.7
Ne II	4392.0	0.15	0.02	0.03	0.05	0.16	0.16
[Ne III]	3868.8	93.4	117.	98.3	112.	110.	109.
[Ne III]	15.5 μm	252.	335.	412.	385.	272.	301.
[Ar IV]	4711.4	2.52	2.72	2.20	1.96	1.97	2.30
[Ar IV]	4740.2	2.34	2.53	2.05	2.37	2.33	2.02
Mean percentage difference			32.7	30.1	26.8	8.26	13.5

[a] The Balmer jump to Hβ ratio is in units of 10^{-2} Å^{-1} and the line intensities are on a scale where $I(\mathrm{H}\beta) = 100$;
[b] Corrected for the contribution from He II λ6683.20 (1.7%);
[c] The λλ3726, 3729 intensities were derived from the total intensity of the blend of H 14, [S III] λ3722, [O II] λλ3726, 3729 and H 13 lines by correcting for the contributions from H 14, [S III] λ3722 and H 13, assuming that the latter lines have intensities as measured from the high-resolution spectrum taken along the nebular minor axis. We further assume that the λ3726 to λ3729 intensity ratio for the whole nebula is the same as that measured along the minor axis.

temperature and density are 8630 K and 2400 cm^{-3} respectively, while $\mathrm{O/H} = 6.4 \times 10^{-4}$ and $\mathrm{He/H} = 0.12$. Note that we only fit the intensities of the neutral helium recombination lines, so we determine only the $\mathrm{He}^{+}/\mathrm{H}$ fraction. With the exception of the high Balmer lines, the differences between the model and observation are generally much larger than the expected uncertainties in the measurements. In particular, there are very large discrepancies for the permitted recombination lines (C II λ4267, O II λ4089 and Ne II λ4392). The last entry in Table 22 is the rms difference between the fitted and observed fluxes, expressed as a percentage.

In model H2, we simulate the effects of temperature fluctuations in the nebula by assuming that the material of the nebula has a Gaussian distribution in $\ln T_{\mathrm{e}}$. If we define $x = \log T_{\mathrm{e}}$, then the fraction of the material, $f(x)$ in the temperature range dx is

$$f(x)\,\mathrm{d}x = \frac{1}{\sigma_x\sqrt{\pi}} \exp\left[-\left(\frac{x - x_0}{\sigma_x}\right)^2\right] \mathrm{d}x. \qquad (17)$$

The temperature distribution in the nebula is then characterized by x_0 and σ_x, for which we find $x_0 = 3.852$ and $\sigma_x = 0.172$, implying a mean temperature of 7110 K with a one-sigma range of 4790–10 570 K. The best fit yields $N_{\mathrm{e}} = 2370\,\mathrm{cm}^{-3}$, $\mathrm{O/H} = 9.0 \times 10^{-4}$ and $\mathrm{He/H} = 0.12$. This model provides a better fit to the Balmer discontinuity than H1, due to the presence of low-temperature material in the nebula and gives a higher oxygen abundance due to the lower mean temperature, but the ORLs are still too weak by up to a factor of 5. This confirms the conclusion of Section 5.3 that temperature fluctuations alone are insufficient to explain the discrepancy.

The discussion of density inhomogeneities in Section 5.4 leads us to consider models in which the nebula may be viewed as consisting of two components each with distinct physical conditions. A model in which only the temperature varies between the components has no advantage over one with temperature fluctuations, while models in which only the density differs have been discussed in Section 5.4, with the conclusion being that the evidence of the high Balmer lines rules out such models. We therefore consider, in the first instance, a two-component model in which both the temperature and the density differ (such two-component models have also been considered by Mathis et al. 1998). The model is then characterized by two densities, two temperatures, a volume filling factor and the oxygen and helium abundances. The results are shown as IH1 in Table 22, while the model parameters for IH1 are listed in Table 21. The densities of the two components are found to be 5750 and 860 cm^{-3}, with the corresponding temperatures being 9550 and 2610 K. The higher density material occupies 0.032 of the total volume, while $\mathrm{O/H} = 1.1 \times 10^{-3}$ and $\mathrm{He/H} = 0.107$ in both components. Although the overall fit is better than for H1 or H2, the prediction of the Balmer discontinuity is markedly worse, due to the presence of extensive material at a very low electron temperature. This discrepancy alone is sufficient to rule out this model as being physically unrealistic. The O/H ratio is increased compared to either of the homogeneous models, but the ORLs are still too weak by a factor of about 3. Even so, the increased neon abundance leads to a large excess flux in the [Ne III] 15.5-μm line. The IR lines of [O III] do not show this excess, because they are collisionally de-excited in the higher density component, while [Ne III] 15.5-μm has a higher N_{crit} and is emitted predominantly from the higher density component.

The second two-component model (IH2) investigates the possibility that the nebula might contain clumps of material that differ in abundance as well as in T_{e} and N_{e} from the material whose properties are diagnosed by the CELs. The model is characterized by two electron densities, two electron temperatures, two oxygen abundances and a filling factor. We also assume that in the components with 'normal' properties, the ratio of helium to hydrogen number densities is 0.1, while the helium abundance is a free paremeter in the other component. The best fit is obtained with the 'normal' component occupying 69 per cent of the volume of the nebula and having an electron density of 5460 cm^{-3}, a temperature of 9480 K and $\mathrm{O/H} = 4.1 \times 10^{-4}$. The remainder of the material has $N_{\mathrm{e}} = 660\,\mathrm{cm}^{-3}$, $T_{\mathrm{e}} = 510$ K, $\mathrm{O/H} = 4.9 \times 10^{-2}$ and $\mathrm{He/H} = 0.44$. The average percentage difference between model and observed intensities is 8 per cent. In this scenario, most of the CEL emission originates from the hotter, denser component, while most of the ORL emission comes from the remaining very cool gas. The agreement between model and observations is good for the ORLs, due to the presence of material in which the oxygen abundance is enhanced by a factor of almost 100 compared to the rest of the nebula. The very low T_{e} of this material provides a solution to the difficulty posed by the [Ne III] 15.5-μm line, in that the temperature is now sufficiently low that collisional excitation of infrared lines is reduced and the large abundance enhancement is not translated into a commensurate increase in flux.

The [Ne III] 15.5-μm line could also be suppressed by a sufficiently high N_{e} in the component with enhanced C, N, O and Ne abundance. We have already seen (Section 5.4) that such a high-density component is inconsistent with the intensities of the high Balmer lines, so we consider a two-component model in which hydrogen is relatively depleted in this component. This model is characterized by the same set of parameters as IH2, but we start the optimization with a high N_{e} in the second component. The best fit for this model (IH3) is obtained when the high metal abundance component occupies a fraction 3.4×10^{-8} of the nebular volume, and has an electron density of $2.2 \times 10^{6}\,\mathrm{cm}^{-3}$, an electron temperature of 4720 K and $\mathrm{He/H} = 0.33$. The remaining material has $N_{\mathrm{e}} = 1370\,\mathrm{cm}^{-3}$, $T_{\mathrm{e}} = 8910$ K and $\mathrm{O/H} = 5.0 \times 10^{-4}$. This model gives a good fit to the metal ORLs and a reasonably good fit to the IR lines, but is significantly worse than IH2 for the Balmer discontinuity. In IH3, almost all the hydrogen emission comes from the lower density component, where $T_{\mathrm{e}} = 8910$ K, determined primarily by the optical CELs. The temperature derived from the observed Balmer jump to H 11 ratio, however, is only 6080 K, or 6380 K from the Balmer jump to Hβ ratio. This model is unable to simultaneously fit the large Balmer discontinuity, which requires a low T_{e}, and the high Balmer lines, which require a low N_{e}.

Carrying out the optimization procedure with different starting values for the second component of IH3 shows that there are several minima in the χ^2 surface, all of which give broadly similar results in terms of the goodness of fit. They differ mainly in the filling factor, N_{e} and hydrogen number density of the second component, but all give very similar results for the O/He ratio (about 0.1) and have relatively high O/H ratios compared to the first component. We note that no stable solutions could be found in which the second component has simultaneously a low T_{e} *and* a high N_{e}, bringing it into approximate pressure equilibrium with the material in component 1.

In Section 3.3 we show that recombination excitation may play an important or even dominant role in the formation of the [O II] nebular and auroral lines, usually collisionally excited in ordinary nebulae. In Section 4.3 we find that the spatial variation of the

surface brightness of the λλ7320, 7330 auroral lines resembles that of a 'typical' (permitted) O II recombination line, such as multiplet V 1 at 4649 Å, both peaking strongly towards the nebular centre (relative to Hβ). In contrast, the λλ3726, 3729 nebular line emission is found to be more diffuse, with a broader radial profile. It is of interest to examine the two-component model predictions for these lines. Both models IH2 and IH3 reproduce the observed intensities of all four forbidden lines reasonably well. Examination of the contributions from the two components shows that for model IH2, emission from both the nebular and auroral lines is dominated by the diffuse component of 'normal' metallicity, with the high-metallicity component contributing only 16 and 25 per cent of the total emission from both components for the nebular and auroral lines respectively. Therefore, for this particular inhomogeneous model, both the nebular and auroral lines are dominated by collisional excitation, and so they should have similar surface brightness distributions which all differ significantly from that of O II multiplet V 1. In contrast, for model IH3, while less than 0.2 per cent of the [O II] λλ3726, 3729 nebular line emission arises from the high-metallicity inclusions, this high-metallicity component dominates the λλ7320, 7330 auroral line formation, contributing 60 per cent of the total emission. Thus in model IH3, the nebular lines are almost entirely collisionally excited. Despite the much higher O/H ratio and lower electron temperature, the high-metallicity component emits little flux in the λλ3726, 3729 nebular lines, due to the high electron density, which causes collisional de-excitation of λλ3726, 3729 before photons can be emitted. Collisional de-excitation is unimportant for the λλ7320, 7330 auroral lines, owing to their much higher critical densities, higher than the density of the high-metallicity component. The low electron temperature in the high-metallicity component and the high excitation energy of the λλ7320, 7330 lines means that recombination is the dominant excitation mechanism in that component. In terms of spatial variations, we would therefore expect the λλ3726, 3729 lines to follow the O^+ abundance variation across the nebula and therefore show a quite different behaviour to typical O II recombination lines, while the λλ7320, 7330 lines should show a variation much more like a typical recombination line and yield high abundances close to those in the high-metallicity component. These expectations are broadly confirmed by Fig. 19, where we compare the surface brightness distributions of the forbidden [O II] nebular and auroral lines with that of the permitted λ4649 O II multiplet V 1 recombination line.

6 DISCUSSION: NGC 6153 – A PN WITH SUPER-METAL-RICH CONDENSATIONS?

We have shown that the heavy-element ORLs from NGC 6153 yield ionic abundances which are consistently about 10 times higher than those obtained from its optical, UV or IR collisional lines, larger even than the factor of 5 discrepancy found by LSBC for the PN NGC 7009. NGC 6153's heavy-element ORLs yield an oxygen abundance which is 6 times solar and a neon abundance which is 16 times solar. If correct, these abundances would certainly justify it being labelled a super-metal-rich object.

In the preceding subsections we have considered a number of possible explanations for this severe discrepancy, including the frequently discussed possibilities of either temperature fluctuations (Peimbert 1967) or density fluctuations (Rubin 1989; Viegas & Clegg 1994). In Section 5.3 we rejected temperature fluctuations as the cause of the lower abundances obtained from the UV and optical CELs, because (a) the magnitude of the abundance discrepancy is not correlated with the excitation energy of the line but, more importantly, because (b) the IR fine-structure lines, which have no significant T_e-sensitivity, yield abundances very similar to those given by the UV and optical CELs.

In Section 5.4 we considered the effects of strong density fluctuations within the nebula, which could selectively reduce the strength of those lines having lower critical densities. This was found to be promising both as a means of explaining the lower electron densities derived from those diagnostic lines having lower critical densities, and for suppressing the lines with lower critical densities used in the [O III] and [N II] optical temperature diagnostic ratios, such that the ratios could then be reconciled with a 'true' T_e equal to the hydrogen recombination Balmer jump temperature (6100 K). An empirical model with the necessary parameters to do this (ambient material with $N_e = 1600\,cm^{-3}$, containing inhomogeneities with $N_e = 1.6 \times 10^6\,cm^{-3}$ and a filling factor of 7.3×10^{-6}) yielded abundances from the optical and IR collisional lines that then broadly agreed with those derived from ORLs, but which also gave C^{2+} and N^{2+} abundances from UV semiforbidden lines that were 9 and 37 times higher than those obtained from ORLs (Case 1 in Table 20). Allowing the adopted T_e to be higher (8000 K, Case 2 in Table 20) would reduce the abundances derived from the UV collisional lines sufficiently for them to agree with those derived from the ORLs, but with the consequence that the ionic abundances obtained from the optical and IR collisional lines then became only a factor of 1.5 higher than the uniform density values derived in Table 8, i.e., well below the ORL abundances. In addition, it was shown via Fig. 20 that both of these two-density-component models predicted Balmer-line intensity progressions that were in disagreement with the observations (which are fitted best by a homogeneous model with an electron density of $2000\,cm^{-3}$).

In Section 5.5, after considering two reference models (one with uniform conditions and the other with a Gaussian distribution of temperature fluctuations), we considered several more two-component models, where each component had a separate T_e and N_e. A model (IH1) which had the same abundances in each component failed, as it produced too large a Balmer jump and too strong emission from the high critical density [Ne III] 15.5-μm line. Much better fits could be obtained by allowing the abundances in each component to differ, as well as their temperatures and densities. A good fit to the observed parameters was obtained with model IH2. This had 70 per cent of the volume of the nebula filled with material having $N_e = 5750\,cm^{-3}$, $T_e = 9550$ K and $O/H = 4.1 \times 10^{-4}$, with the remainder having $N_e = 660\,cm^{-3}$, $T_e = 510$ K and $O/H = 4.9 \times 10^{-2}$. In this model the hot component produces the UV and optical CELs, and the very cool component produces the heavy-element ORLs and the IR fine-structure lines, with both components contributing to the hydrogenic line and continuum emission. Improved agreement with the observed [Ne III] 15.5-μm line intensity was obtained because T_e of the cool component was sufficiently low to reduce the efficiency of collisional excitation. The high critical density [Ne III] 15.5-μm line can also be suppressed by a sufficiently high N_e, so model IH3 contained a low filling-factor, hydrogen-deficient component, with $N_e = 2.2 \times 10^6\,cm^{-3}$ and $T_e = 4700$ K, immersed in 'normal' material with $N_e = 1370\,cm^{-3}$, $T_e = 8900$ K and $O/H = 5.0 \times 10^{-4}$. For this model the mean percentage difference between the observed and predicted line intensities (Table 22) was only slightly larger than for model IH2,

but the predicted hydrogen emission was too hot to match the observed T_e(BJ) of 6000 K. Overall, these two-component dual-abundance models seem to hold promise as an explanation for the severe discrepancies found when assuming a chemically homogeneous nebula. However, we may ask: (1) are the parameters of the inferred metal-enhanced inclusions physically reasonable, and (2) are there are any precedents for them in other planetary nebulae?

Jacoby (1979) and Hazard et al. (1980) discovered knots of extremely hydrogen-deficient material at the centres of the old planetary nebulae A 30 and A 78, which were interpreted by Iben et al. (1983) as having been ejected during a final helium flash which briefly brought the central star back to the AGB from the white dwarf cooling track to repeat its post-AGB evolution. From deep spectroscopy of Abell 30's knots, Guerrero & Manchado (1996) inferred that the knots were not completely H-deficient, but that 90–95 per cent of their original hydrogen had been converted to helium (with He/H ratios of 4–8, versus values of 0.3–0.4 for the postulated H-deficient knots in models IH2 and IH3 for NGC 6153). Both Jacoby & Ford (1983) and Guerrero & Manchado detected very strong C II λ4267 and C III λ4650 recombination line emission from Abell 30's knots. Harrington & Feibelman (1984) compared the λ4267 strength with that of C III] λ1908 in their *IUE* spectrum and the λ4650 strength with that of the collisionally excited C IV λ1549 resonance doublet. They found that the observed C^{2+} line ratio implied an electron temperature of only 7800 K [compared with an observed T_e([O III]) of 13 400–16 400 K], and that the observed C^{3+} line ratio implied an electron temperature of only 10 600 K. An explanation considered by them for this behaviour was that the knots might have cool (∼1000 K), but still highly ionized, cores due to high CNO coolant abundances relative to helium. The carbon ORLs would then originate predominantly from the cool cores, while the UV collisional lines would originate from the hotter surrounding regions of the knots, so that CEL to ORL temperatures for carbon would be meaningless. We have already noted in Section 2.1.3 that the central star of NGC 6153 shows the same H-deficient O VI and C IV emission line characteristics as the central stars of A 30 and A 78, so it may not be implausible that similar H-deficient knots of material have been ejected into NGC 6153 in the past. The central peaking of the ORL oxygen and carbon abundances (Fig. 18) and of the ORL to CEL abundance ratio (Figs 17 and 18) could be consistent with a relatively recent ejection of H-deficient knots into NGC 6153. Because of the much higher surface brightness of its main nebula compared to those of A 30 and A 78, such knots could be difficult to discern – a high spectral resolution search for components with different kinematics from the main nebula might offer one means for their detection.

Another relevant object is A 58, whose central star V605 Aql experienced a nova-like event in 1919 and now exhibits broad WR-like C IV λ5801,12 emission, indicative of hydrogen deficiency (Seitter 1987; Guerrero & Manchado 1996). A high-velocity knot at the centre of the A 58 nebula exhibits extreme H-deficiency (Pollacco et al. 1992; Guerrero & Manchado 1996). The latter found it to exhibit extremely strong [O I] λλ6300, 6363 and [O II] λλ7320, 7330 emission lines. We take this as evidence that the A 58 knot has a relatively high-density core that has not yet been fully ionized since its ejection in 1919. The deduced dynamical ages of the H-deficient knots in A 30 and A 78 are, on the other hand, significantly longer (∼10^3 yr; e.g. Meaburn et al. 1998b), consistent with having been ionized to a greater degree.

Model IH2 produces a somewhat better match to the observations of NGC 6153 than does model IH3. However, IH2's H-deficient regions occupy 30 per cent of the volume of the nebula and contribute 82 per cent of all the heavy elements in the nebula (Table 21), which both seem implausibly high. Its H-deficient inclusions have an 8 times lower N_e and a 20 times lower T_e than the surrounding 'normal' material. This factor of 160 overpressure would soon lead to the compression and collapse of the inclusions, if they were already fully ionized. If instead they corresponded to evaporating regions around dense neutral cores, then compression might be prevented – pressure equilibrium would require a neutral density of 10^5 cm^{-3} for a temperature of 500 K, and a correspondingly higher density if the core temperatures were lower. It is noteworthy that Reay & Atherton (1985) concluded from an analysis of Fabry–Perot [O I] imaging observations of NGC 7009 that it must contain cool (∼45 K), dense (∼4×10^6 cm^{-3}) neutral condensations – NGC 7009 was found by LSBC to also show a large discrepancy between its ORL and CEL heavy-element abundances. Similar densities and temperatures have been inferred for the cometary globules in the Helix nebula (NGC 7293), for which core densities of 10^5–10^6 cm^{-3} and core temperatures of 10–50 K have been estimated (Dyson et al. 1989; Meaburn et al. 1992, 1998a; Huggins et al. 1992; O'Dell & Handron 1996). The density estimates for the Helix were based on the assumption of standard hydrogen to dust and hydrogen to CO ratios, and would be reduced if the globules were instead assumed to be H-deficient. However, the fact that the mid-infrared *ISO* spectrum of NGC 7293 is dominated by H_2 emission lines (Cox et al. 1998) indicates that the neutral globules are unlikely to be H-deficient. The fact that the [O I] 6300-Å line is very weak in the optical spectrum of NGC 6153 (Table 2), while the [O I] 63- and 146-μm lines are not detected in our *ISO* LWS spectrum, means that there is no direct observational evidence for the presence of dense neutral knots. On the other hand, although no [O I] 6300-Å emission has been detected in any of the spectra of A 30's H-deficient knots, Borkowski, Harrington & Tsvetanov (1995) suggested that several of its knots may contain dense neutral cores.

Model IH3 for NGC 6153 (Table 21) contains dense, fully-ionized, H-deficient inclusions, occupying only 3.4×10^{-8} of the nebular volume and contributing only 0.3 per cent of the heavy elements in the nebula, much more plausible fractions than in the case of model IH2. Since such knots would have a pressure that was a factor of ∼1000 *larger* than that of the surrounding 'normal' material, they should dissipate on a sound-crossing time-scale (unless confined, e.g., by stellar-wind ram pressure). For a distance of 2.1 kpc (Kingsburgh & English 1992) this time-scale would be 1400θ yr, for a knot of angular radius θ arcsec. If one assumes that such (undiscovered) high-density knots must be less than 0.2 arcsec in radius, very short lifetimes are implied for them. Again, the presence of dense neutral cores within the knots, providing a reservoir of material, would help to alleviate this problem. The very small filling factor and low total mass of the H-deficient inclusions of model IH3 would make it easier for them to escape direct detection than in the case of model IH2.

Model IH3 thus appears much more physically plausible than model IH2 on several grounds. Model IH3 is unable, however, to account for the low observed hydrogen Balmer jump temperature of NGC 6153, relative to its observed optical forbidden line temperatures, since IH3's cool clumps are too hydrogen-deficient. Perhaps an intermediate-temperature interface between such clumps and the rest of the nebula might exist, into which hydrogen has been mixed, but it is not obvious that the total

amount of hydrogen in such interface zones could be sufficient to appreciably affect the magnitude of the overall Balmer jump.

Although models containing H-deficient clumps are successful in accounting for a number of the major discrepancies found for NGC 6153 when using standard analysis techniques, a major problem still remains, namely that the heavy-element ionic abundance ratios (e.g., N^{2+}/O^{2+}, C^{2+}/O^{2+}) derived from ORLs are identical within the errors with the same ratios derived from CELs. In the closest-fitting models, the ORLs come from H-deficient regions, while the CELs come from 'normal' abundance nebular material. However, no known nuclear processes can produce hydrogen-deficient material while preserving the C/O, N/O and Ne/O ratios of the original material. We therefore conclude that a convincing physical model that can account for the full range of behaviour exhibited by NGC 6153 has still to be found.

ACKNOWLEDGEMENTS

MC thanks NASA for its support for this work under grant NAG 5-4884. We thank Professor J. S. Mathis, Dr R. Rubin and an anonymous referee for helpful comments.

REFERENCES

Aggarwal K. M., 1983, ApJS, 52, 387
Anandarao B. G., Banerjee D. P. K., 1988, A&A, 202, 215
Anders E., Grevesse N., 1989, Geochim. Cosmochim. Acta, 53, 197
Barker T., 1978, ApJ, 219, 914
Barker T., 1991, ApJ, 371, 217
Barlow M. J., 1995, in Appenzeller I., ed., Highlights of Astronomy, Vol. 10. Kluwer, Dordrecht, p. 476
Bayes F. A., Saraph H. E., Seaton M. J., 1985, MNRAS, 215, 85P
Berrington K. A., Burke P. G., Butler K., Seaton M. J., Storey P. J., Taylor K. T., Yan Yu., 1987, J. Phys. B: Atom. Mol. Phys., 20, 6379
Blum R., Pradhan A. K., 1992, ApJS, 80, 425
Borkowski K. J., Harrington J. P., Tsvetanov Z. I., 1995, ApJ, 449, L143
Brocklehurst M., 1972, MNRAS, 157, 211
Brown R. L., Mathews W. G., 1970, ApJ, 160, 939
Butler K., Zeippen C. J., 1989, A&A, 208, 337
Butler K., Zeippen C. J., 1994, A&AS, 108, 1
Cahn J. H., Kaler J. B., Stanghellini L., 1992, A&AS, 94, 399
Clegg P. E. et al., 1996, A&A, 315, L38
Cohen M., Barlow M. J., 1980, ApJ, 238, 585
Cohen M., Walker R. G., Witteborn F. C., 1992, AJ, 104, 2030
Cox P. E. et al., 1998, ApJ, 495, L23
Crenshaw D. M., Bruegman O. W., Norman D. J., 1990, PASP, 102, 463
Crowther P. A., De Marco O., Barlow M. J., 1998, MNRAS, 296, 367
Cunto W., Mendoza C., Ochsenbein F., Zeippen C. J., 1993, A&A, 275, L5
Davey A. R., Storey P. J., Kisielius R., 1999, A&AS, in press
Dinerstein H. L., Lester D., Werner M. W., 1985, ApJ, 291, 561
Dinerstein H. L., Haas M. R., Erickson E. F., Werner M. W., 1995, in Haas M. R., Davidson J. A., Erickson E. F., eds, ASP Conf. Ser. Vol. 73, Airborne Astronomy Symp. on the Galactic Ecosystem. Astron. Soc. Pac., San Francisco, p. 387
Dyson J. E., Hartquist T. W., Pettini M., Smith L. J., 1989, MNRAS, 241, 625
Eissner W. E., Jones M., Nussbaumer H., 1974, Comput. Phys. Commun., 8, 270
Escalante V., Victor G. A., 1990, ApJS, 73, 513
Fang Z., Kwong H. S., Parkinson W. H., 1993, ApJ, 413, L141
Fich M., Blitz L., Stark A. A., 1989, ApJ, 342, 272
Fleming J., Bell K. L., Hibbert A., Vaeck N., Godefroid M. R., 1996, MNRAS, 279, 1289
Giles K., 1981, MNRAS, 195, 64P
Grandi S. A., 1976, ApJ, 206, 658
Grevesse N., Noels A., 1993, in Prantzos N., Vangioni-Flam E., Cassé M., eds, Origin and Evolution of the Elements. Cambridge Univ. Press, Cambridge, p. 15
Grevesse N., Sauval A. J., 1998, Rev., Space Sci., 85, 161
Gruenwald R., Viegas S. M., 1995, A&A, 303, 535
Guerrero M. A., Manchado A., 1996, ApJ, 472, 711
Hamuy M., Suntzeff N. B., Heathcote S. R., Walker A. R., Gigoux P., Phillips M. M., 1994, PASP, 106, 566
Harrington J. P., Feibelman W. A., 1984, ApJ, 277, 716
Hazard C., Terlevich R., Morton D. C., Sargent W. L. W., Ferland G., 1980, Nat, 285, 463
Howarth I. D., 1983, MNRAS, 203, 301
Huggins P. J., Bachiller R., Cox P., Forveille T., 1992, ApJ, 401, L43
Iben I., Jr, Kaler J. B., Truran J. W., Renzini A., 1983, ApJ, 264, 605
Jacoby G. H., 1979, PASP, 91, 574
Jacoby G. H., Ford H. C., 1983, ApJ, 266, 298
Johnson C. T., Kingston A. E., 1990, J. Phys. B, 23, 3393
Kaler J. B., 1986, ApJ, 308, 337
Kallman T., McCray R., 1980, ApJ, 242, 615
Keenan F. P., Feibelman W. A., Berrington K. A., 1992, ApJ, 389, 443
Keenan F. P., Hibbert A., Ojha P. C., Conlon E. S., 1993, Phys. Scripta., 48, 129
Keenan F. P., Aller L. H., Bell K. L., Hyung S., McKenna F. C., Ramsbottom C. A., 1996, MNRAS, 281, 1073
Kessler M. F. et al., 1996, A&A, 315, L27
Kingdon J., Ferland G. J., 1995a, ApJ, 442, 714
Kingdon J., Ferland G. J., 1995b, ApJ, 450, 691
Kingsburgh R. L., Barlow M. J., 1994, MNRAS, 271, 257
Kingsburgh R. L., English J., 1992, MNRAS, 259, 635
Kisielius R., Storey P. J., Davey A. R., Neale L. T., 1998, A&AS, 133, 257
Liu X.-W., Danziger I. J., 1993a, MNRAS, 261, 465
Liu X.-W., Danziger I. J., 1993b, MNRAS, 263, 256
Liu X.-W., Danziger I. J., Murdin P., 1993, MNRAS, 262, 699
Liu X.-W., Storey P. J., Barlow M. J., Clegg R. E. S., 1995a, MNRAS, 272, 369 (LSBC)
Liu X.-W., Barlow M. J., Danziger I. J., Storey P. J., 1995b, ApJ, 450, L59
Liu S.-W., 1997, in Kessler M. F., ed., The First *ISO* Workshop on Analytical Spectroscopy. ESA Publication Division, ESTEC, p. 87
Liu X.-W., 1998, Ap&SS, 255, 499
Liu X.-W., Barlow M. J., Danziger I. J., Storey P. J., 1999, in Walsh J. R., Rosa M. R., eds, Proc. ESO Workshop on Chemical Evolution from Zero to High Redshift. Springer-Verlag, Berlin, p. 39
Mathis J. S., Torres-Peimbert S., Peimbert M., 1998, ApJ, 495, 328
Meaburn J., Clayton C. A., Bryce M., Walsh J. R., Holloway A. J., Steffen W., 1998a, MNRAS, 294, 201
Meaburn J., Lopez J. A., Bryce M., Redman M. P., 1998b, A&A, 334, 670
Meaburn J., Walsh J. R., Clegg R. E. S., Walton N. A., Taylor D., Berry D. S., 1992, MNRAS, 255, 177
Meatheringham S. J., Wood P. R., Faulkner D. J., 1988, ApJ, 334, 862
Mendez R. H., 1991, in Michaud G., Tutukov A. V., eds, Proc. IAU Symp. 145, Evolution of Stars: the Photospheric Abundance Connection. Kluwer, Dordrecht, p. 375
Mendoza C., 1983, in Flower D. R., ed., Planetary Nebulae. Kluwer, Dordrecht, p. 143
Mendoza C., Zeippen C. J., 1982a, MNRAS, 198, 127
Mendoza C., Zeippen C. J., 1982b, MNRAS, 199, 1025
Mendoza C., Zeippen C. J., 1983, MNRAS, 202, 981
Milne D. K., 1973, AJ, 78, 239
Nussbaumer H., Rusca C., 1979, A&A, 72, 129
Nussbaumer H., Storey P. J., 1981, A&A, 99, 177
Nussbaumer H., Storey P. J., 1984, A&AS, 56, 293
O'Dell C. R., Handron K. D., 1996, AJ, 111, 1630
Osterbrock D., 1989, Astrophysics of Gaseous Nebulae and Active Galactic Nuclei. University Science Books, Mill Valley, CA
Parthasarathy M., Acker A., Stenholm B., 1998, A&A, 329, L9
Peimbert M., 1967, ApJ, 150, 825
Peimbert M., 1971, Bol. Obs. Tonantzintla y Tacubaya, 6, 29

Peimbert M., 1994, in Williams R., Livio M., eds, The Analysis of Emission Lines. Cambridge Univ. Press, Cambridge, p. 165
Peimbert M., Torres-Peimbert S., 1983, in Flower D. R., ed., Planetary Nebulae. Kluwer, Dordrecht, p. 233
Peimbert M., Sarmiento A., Fierro J., 1991, PASP, 103, 815
Peimbert M., Storey P. J., Torres-Peimbert S., 1993, ApJ, 414, 626
Péquignot D., Petitjean P., Boisson C., 1991, A&A, 251, 680
Pérez E., 1997, MNRAS, 290, 465
Pollacco D. L., Lawson W. A., Clegg R. E. S., Hill P. W., 1992, MNRAS, 257, 33P
Pottasch S. R. et al., 1984, ApJ, 278, L33
Pottasch S. R., Dennefeld M., Mo J.-E., 1986, A&A, 155, 397 (PDM)
Pradhan A. K., 1976, MNRAS, 177, 31
Reay N. K., Atherton P. D., 1985, MNRAS, 215, 233
Rola C., Stasińska G., 1994, A&A, 282, 199
Rubin R. H., 1986, ApJ, 309, 334
Rubin R. H., 1989, ApJS, 69, 897
Rubin R. H., Colgan S. W. J., Haas M. R., Lord S., Simpson J. P., 1997, ApJ, 479, 332
Saraph H. E., Storey P. J., 1999, A&AS, 134, 369
Sawey P., Berrington K. A., 1993, Data Tables, Atomic Data Nucl., 55, 81
Schachter J., 1991, PASP, 103, 457
Schneider S. E., Terzian Y., Purgathofer A., Perinotto M., 1983, ApJS, 52, 399
Seitter W. C., 1987, ESO Messenger, 50, 14
Smith L. F., Aller L. H., 1969, ApJ, 157, 1245
Smits D. P., 1996, MNRAS, 278, 683
Stafford R. P., Bell K. L., Hibbert A., Wijesundera W. P., 1994, MNRAS, 268, 816
Storey P. J., 1994, A&A, 282, 999
Storey P. J., Hummer D. G., 1995, MNRAS, 272, 41
Torres-Peimbert S., Peimbert M., Peña M., 1990, A&A, 233, 540
Walsh J. R., 1993, ST-ECF Newsletter, 19, 6
Walter D. K., Dufour R. J., 1994, ApJ, 434, L29
Viegas S., Clegg R. E. S., 1994, MNRAS, 271, 993
Zeippen C. J., 1982, MNRAS, 198, 111
Zeippen C. J., Butler K., Le Bourlot J., 1987, A&A, 188, 251

APPENDIX A RECOMBINATION COEFFICIENTS FOR $O^{2+} + e^-$

Recombination coefficients for O II lines were given by Storey (1994), but he did not give effective recombination coefficients for the $2p^3\ ^2P^o$ and $^2D^o$ states, because the photoionization cross-sections contain significant resonance features which are not accurately delineated in the Opacity Project work for this ion (Cunto et al. 1993; Lennon & Burke, private communication). The presence of resonance features implies that direct dielectronic recombination is important for these states; indeed, the calculations of Storey show that the total recombination coefficient for the $2p^3\ ^2P^o$ and $^2D^o$ states is dominated by direct recombination, with cascade contributions being relatively unimportant. We have therefore carried out a new calculation of the direct recombination coefficient to the $2p^3\ ^2P^o$ and $^2D^o$ states, using the methods developed for the Opacity Project (Berrington et al. 1987).

Table A1. Recombination coefficients, α ($10^{-13}\,cm^3\,s^{-1}$) for O^+ $2p^3\ ^2P^o$ and $2p^3\ ^2D^o$. Direct recombination, α_d from this work, cascade contributions, α_c from Storey (1994). α_T is the total recombination coefficient.

T_e[K]	$^2P^o$			$^2D^o$		
	α_d	α_c	α_T	α_d	α_c	α_T
5000	5.079	2.492	7.571	12.90	5.020	17.92
7500	4.320	1.831	6.151	10.45	3.720	14.17
10000	3.881	1.490	5.371	8.973	3.060	12.03
15000	3.365	1.149	4.514	7.289	2.466	9.755
20000	3.050	0.989	4.039	6.340	2.197	8.537

We describe the O^{2+} target in terms of the following 13 electron configurations,

$2s^22p$ $2s2p^3$ $2p^4$,
$2s^22p3d$ $2s2p^23d$ $2p^33d$,
$2s^23d^2$ $2p^23d^2$ $2s2p3d^2$,
$2s^22p4f$ $2p^34f$,
$2s^24f^2$ $2p^24f^2$,

where the target radial wave functions were computed with the atomic structure code SUPERSTRUCTURE (Eissner, Jones & Nussbaumer 1974), and the 3d and 4f orbitals are short-range correlation functions, computed in scaled Coulomb potentials (Nussbaumer & Storey 1978). The target was represented by the 12 terms of the three electron configurations of the $n = 2$ complex, $2s^22p^2$, $2s2p^3$ and $2p^4$, and bound state wave functions and photoionization cross-sections were computed using the Opacity Project methods (for more details see Berrington et al. 1987), making sure that all important resonance features were fully delineated. The techniques used to ensure this are described in Kisielius et al. (1998). The direct recombination coefficients to the $2p^3\ ^2P^o$ and $^2D^o$ states were calculated from the photoionization cross-section data and the cascade contributions, which are about 25 per cent of the total, were taken from the earlier calculations of Storey (1994). The direct, cascade and total recombination coefficients are tabulated in Table A1.

This paper has been typeset from a TEX/LATEX file prepared by the author.